PO-AK 85

FINAL REPORT

Contract #NA-84-ABC-00225
Research Unit 627
Number of pages: 131

Numerical Modeling of Storm Surges in the Norton Sound

Zygmunt Kowalik

and

Walter R. Johnson

Institute of Marine Science
University of Alaska
Fairbanks, Alaska 99701

July 1985

Prepared for the
National Oceanic and Atmospheric Administration

ABSTRACT

Storm surges and their associated water and ice motion are important to the continuing offshore exploration for petroleum on the continental shelves. The shore of the Bering Sea in the Norton Sound region is generally of low relief, so coastal plains can be inundated by the surge and waves. The knowledge of sea level variations along the Alaska coast is scant. Tide gauges have been operated in this region only at irregular intervals, and the present set of data is too small to estimate a statistically valid distribution of the sea level variations. The goal of this project is to develope methods of predicting storm surges based on the equations of motion and continuity.

Specific problems of storm-surge modeling in the polar seas were analyzed. The vertically integrated equations of motion and continuity were applied to the prediction of the storm-surge waves in both the ice-free and ice-covered seas. The interactions of atmosphere, ice, and water were expressed by the normal and tangential stresses. A numerical grid was established over the Bering Sea and Norton Sound and three storm-surges were simulated and briefly described. The Norton Sound area was investigated using an additional smaller scale model. Comparison of the measured and computed sea level, and observed and computed ice velocities, proves that the model is suitable to reproduce both water and ice motion.

TABLE OF CONTENTS

1. INTRODUCTION

The Bering Sea has one of the largest continental shelves in the world. Along this shelf during late summer and fall low pressure systems generate storm surge waves. Two regions of the Bering Sea are obvious candidates for large sea level variations, i.e., Bristol Bay and Norton Sound. Shallow Norton Sound, with an average depth of about 20 m, leads to strong amplification of the storm wave, especially in conjunction with west and southwest winds.

The knowledge of sea level changes caused by storm surges is quite modest in Norton Sound mainly due to the absence of any permanent tide gauges in this area. The frequency of major storms, when compared to the other regions of the Bering Sea, is rather low. Late summer and fall storms, if they generate south, southwest or northwest winds, can cause extensive flooding to the coastal areas of low relief surrounding Norton Sound. The main storm track during summer and fall is toward the north and northeast [*Brower et al., 1977*]. Storm surges of as much as 4 m have occurred in this area and the most recent storm of such intensity was in November 1974 [*Fathauer, 1978*]. The most severe flooding occurred at Nome, where the damage sustained was estimated at $12 million. The low pressure system moved from the Aleutians to the Bering *Sea.* Winds as high as 75 knots were recorded. The extent of flooding were tracked by USGS through an observation of the driftwood and debris line after the storm [*Sallenger*, 1983]. This storm has been used as the wind forcing for one of the model cases (Section 4.4). Surges of 1 to 2 m regularly flood the Norton Sound area and cause serious problems to the coastal communities [*Wise et al.*, 19811. Until now tide gauges were installed in this region only for *shore* periods

of time. Sea level data were recorded in Norton Sound during a sediment transport study in summer and fall 1977 [*Cacchione and Drake*, 1979]. The Yukon River discharges about 60 million tons of suspended matter per year into the Bering Sea [*Drake et al.*, 19801. The fall storm surges are responsible for much of the transport and resuspension of the sediments derived from the Yukon.

In 1978 a set of sea level data was gathered over the shelf by *Schumacher and Tripp [19791. An* extensive observational study of tides and tidal currents in the northeastern Bering Sea from November 1981 until August 1982 was conducted by NOAA/PMEL [*Mofjeld*, 1984]. At the same time, sea level was recorded at a nearshore station in Stebbins (R. Mitchel, personal comm.) – an area where fast ice usually occurs in winter. During 1982 ice drift motion was also studied from several ARGOS drifting ice platforms [*Reynolds and Pease, 1984].* This set of diverse data gave a good opportunity to test our model, especially the influence of nearshore fast ice on the storm surge wave propagation.

Wise *et al.* [1981] compiled all available data on the storm surges and were able to identify 13 floodings at Nome and 10 at Unalakleet. Although the present set of data is too small to estimate a statistically valid distribution of the sea level variations, the statistics developed by *Wise et al. [1981]* may serve as a first approach to the prediction of the surge range.

The lack of knowledge on the sea level distribution can be modified by applying numerical modeling. Numerical models are useful because they provide a possibility to study the time-dependent distribution of sea level and vertically averaged current. *Leendertse and Liu* [1981] developed a three-dimensional model of Norton Sound to study the density

and tide-driven motion. We have applied a model to study storm surge in the Norton Sound area based on a model previously tested in the Beaufort and Chukchi Seas [*Kowalik and Matthews*, 1982; *Kowalik*, 1984] . To drive the storm surge model, suitable wind data are required; we used the surface pressure charts to compute the geostrophic and surface winds. First, geostrophic wind was computed from the atmospheric pressure, then the "true" wind was computed by application of empirical coefficients [*Albright*, 1980; *Walter and Overland*, *1984].*

In the polar regions, ice cover impedes the transfer of momentum from the atmosphere to the ocean thus influencing the spatial and temporal distribution of the storm surges [*Henry*, 1974]. Therefore, while developing a storm surge model for the Beaufort and Chukchi Seas, a scheme to include ice cover was developed. Various constitutive laws to describe sea ice, proposed by *Coon et al. [1974]* and *Hibler [1979],* contain both mechanical and thermal properties of ice. A storm *surge is a* phenomenon of short duration. In such cases thermal properties of ice growth and decay can be neglected and only ice mechanics needs to be considered. Therefore, for storm surge modeling, a simpler constitutive law has been implemented, as proposed by *Doronin [1970].* Ice motion in Norton Sound has been studied by *Stringer and Henzler [1981].* Direct comparison of the . . ice motion observed through the satellite imagery with the ice movement computed by the model seems to be the best approach to validate this segment of the model. Unfortunately, the acquisition of the cloud-free images during storms has a rather small probability.

Air-ice interaction has been studied both from ice floe stations and aircraft. *Macklin* [1983] reported a wind drag coefficient over ice of

3.1X 10^{-3}. Measurements by *Walter and Overland* [1984] gave a similar value for the drag coefficient. These values are among the largest for the polar seas [*Leavitt, 1980].*

The steady-state slab models of the wind-driven ice drift developed for the Bering Sea shelf by *Pease and Overland [1984]* and *Overland et al.* [1984] show a very good correlation with the observed ice motion. Through the application of these models it has been established that the influence of the bathymetry on the wind-drift of ice in shallow seas is constrained to water depth less than 30 m.

Storm surges occur together with astronomical tides and therefore it is essential to understand the tide distribution. The tide distribution in the Norton Sound is known approximately through the observations and numerical modeling [*Pearson et al., 1981; Mofjeld,* 1984] . A tidal range of the order of 1 m to 1.5 m can be expected. The semidiurnal (M_2) component has an amphidromic point in the Norton Sound, therefore the diurnal components dominate tidal regime.

2. FORMULATION OF BASIC EQUATIONS

The basis for calculations is the vertically integrated equations of water motion and continuity, written in the Cartesian coordinate system $\{x_i\}$, with x_1 directed to the east and X_2 directed to the north:

$$\frac{\partial u_i}{\partial t} + \varepsilon_{ij} u_j + \frac{\partial}{\partial x_j}(u_i u_j) = - g \frac{\partial \zeta}{\partial x_i} - \frac{1}{\rho_w} \frac{\partial P_a}{\partial x_i} + \frac{(1-c)\tau_i^a}{Ho_w} + \frac{c\tau_i^w}{Ho_w} - \frac{\tau_i^b}{\rho_w H} + A \frac{\partial^2 u_i}{\partial x_j^2} \quad (1)$$

$$\frac{\partial \zeta}{\partial t} + \frac{\partial (Hu_i)}{\partial x_i} = 0 \quad (2)$$

The ice motion induced by wind is studied through the following equations of motion [*Rothrock, 1975]*;

$$m \frac{\partial v_i}{\partial t} + m \frac{\partial}{\partial x_j}(v_i v_j) + m \varepsilon_{ij} v_j = \tau_i^a - c \frac{\partial Pa}{\partial x_i} + c (T_i^a - \tau_i^w) + F_i \quad (3)$$

Rate of change of the ice mass (m) over a specific area is equal to the net influx of mass to that area plus all sources and sinks (ϕ) [*Rothrock*, 1970]. The equation of continuity for the ice mass consistent with the above considerations is;

$$\frac{\partial m}{\partial t} + \frac{\partial (mv_i)}{\partial x_i} = \phi$$

In the above equations the following notation is used;

- i,j — indices ($i,j = 1,2$) where 1 stands for east coordinate, and 2 for north coordinate;
- t — time;
- u_i — components of the water velocity vector;
- v_i — components of the ice velocity vector;
- τ_i^a — components of the wind stress vector over the sea;

τ_i^a — components of the wind stress vector over the ice;

τ_i^w components of the water stress;

τ_i^b components of the bottom stress;

F_i components of the force due to internal ice stress;

Pa atmospheric pressure;

ε_{ij} Coriolis tensor;

ζ variation of the sea level or the ice around the undisturbed level;

c ice compactness; $0 \leqslant c \leqslant 1$;

H water depth;

ρ_w water density;

A lateral eddy viscosity, usually will be taken as 5×10^8 cm^2/s;

m ice concentration or mass per unit area;

h ice thickness;

g gravity acceleration.

Einstein's summation convention is applied throughout all indexed expressions. The variables and coefficients in the equations are expressed in CGS units.

Assuming that the ice is not spread evenly over the whole sea surface, the mass of ice can be expressed through the ice compactness (c), ice thickness (h), and ice density (p);

$$m = phc \tag{5}$$

A *storm* surge is a phenomenon of a relatively short duration, therefore thermodynamic sources and sinks linked to ϕ in equation (4) can be neglected. The equation of mass balance can be divided into two separate equations, i.e., a continuity equation for the ice compactness and an equation of thickness balance;

$$\frac{\partial c}{\partial t} + \frac{\partial (v_i c)}{\partial x_i} = 0 \qquad (6)''$$

$$\frac{\partial h}{\partial t} + v_i \frac{\partial h}{\partial x_i} = 0 \qquad (i)$$

Both equations (4) and (6) are applied along with equations (1) through (3) to obtain the ice mass and the ice compactness distributions. It is reasonable to assume that when the ice is not packed closely ($c<1$) the ice thickness is not changed due to the ice motion. If, on the other hand due to internal ice stress, the ice compactness will grow beyond $c=1$, the excess of compactness will lead to a change of the ice thickness. In such a case the new ice thickness distribution is computed through equation (5).

To derive a solution to equations (1) through (6), suitable boundary and initial conditions must be stated. Among all possible sets of the boundary conditions, the one chosen should lead to a unique solution to the above system of equations. Such a set of conditions is still undefined for the ice-ocean interaction, therefore we shall assume (since the ice flow equations are analogous to the water flow equations) that the specification of the normal and tangential velocities along the boundaries is sufficient to derive the unique solution [*Marchuk et al., 3.972].* Usually on the open boundaries (i.e., water boundaries) the storm surge velocity distribution is unknown. To overcome this hindrance the conditions on the open boundary are specified for the sea level and instead of a parabolic problem, a new problem is formulated in which the horizontal exchange of momentum is neglected. This simplified problem is solved along the open boundary to define velocity distribution. Having defined the velocity at the boundary, the solution of the complete system of equations is sought.

3. NUMERICAL MODELING : AREA , GRID, BOUNDARY COND IT IONS AND NUMERICAL SOLUTION

The main modeling effort is confined to Norton Sound (Fig. 1). The Norton Sound model has three open boundaries (broken lines); in the Bering Strait, between Siberia and St. Lawrence Island, and between St. Lawrence Island and Alaska. 'The grid intervals of the numerical lattice are 1/6 of a degree of latitude and 1/2 degree of longitude. To check the validity of the model with the open boundaries we also compute the storm surges throughout the Bering Sea area with a larger numerical grid spacing of 0.5 degree of latitude and 1.5 degree of longitude (Fig. 1). The application of the radiation condition by *Reid and Bodine [1968]* and the modified versions by *Camerlengo and O'Brien [1980],* and *Raymond and Kuo [1984]* lead to a distorted sea level distribution in Norton Sound. Such behavior of the solution may be related to the depth distribution since the average depth of Norton Sound is about 20 m and the open boundaries of the numerical model were located at the 30- to 50-m depth.

Normally, in a storm surge computation, the radiating boundary is situated beyond the shelf break (and/or far away from the region of interest) and the comparison of calculated and measured sea level in the shelf zone is quite satisfactory. The radiation condition is applied to waves generated inside the domain of integration. In those instances when only certain portions of the shelf are considered, waves generated outside the domain may influence the solution. Therefore, to solve the equations of water motion and continuity in Norton Sound, first, the solution for the entire Bering Sea is calculated. Then the distribution of velocity and sea level at the open boundary of the refined model is defined by linear interpolation from the results of those calculations.

Numerical solutions to equations (1)-(6) were obtained by applying an explicit-in-time and staggered-in-space numerical scheme proposed by *Hansen [19621.* Internal ice stresses (F_i) in the equations of motion are expressed by a linear viscous model

$$F_i = \eta \frac{\partial^2 v_i}{\partial x_j \partial x_j} \quad m \tag{8}$$

with the magnitude of kinematic viscosity coefficient ranging from $5 \cdot 10^8$ cm^2/s to $5 \cdot 10^{12}$ Cm^2/s. For large viscosity coefficient the explicit scheme is unstable [*Kowalik*, 1981]. Therefore, to model fast ice (which is parametrized by a large value of viscosity coefficient), a modified scheme of numerical computation, unconditionally stable in time, has been introduced. We shall explain the approach only for the one component of equation (3). The time variations of the E-W component of ice velocity caused by internal *stresses* are expressed by

$$\frac{\partial v}{\partial t} = \eta \left(\frac{\partial^2 v}{\partial x_1^2} + \frac{\partial^2 v}{\partial x_2^2} \right) \tag{9}$$

(where v_1 is changed to v).

To integrate numerically the above equation, the time step T and space lattice with step h is introduced. Independent variables t, x_1, and x_2 are expressed as t = KT, x_1 = Lh, x_2 = Mh, and the numerical form of *(a)*

$$\frac{v_{L,M}^{K+1} - v_{L,M}^{K}}{T} = \frac{\eta}{h} \left(\frac{v_{L+1,M}^{K} - v_{L,M}^{K}}{h} - \frac{v_{L,M}^{K+1} - v_{L-1,M}^{K+1}}{h} \right) + h \frac{\eta}{} \left(\frac{v_{L,M+1}^{K} - v_{L,M}^{K}}{h} - \frac{v_{L,M}^{K+1} - v_{L,M-1}^{K+1}}{h} \right) \tag{10}$$

is the advancing solution in time from t = KT to t =, (K+1)T. This numerical scheme is unconditionally stable for any (positive) η. The actual computation is explicit although the values $v^{K+1}_{L-1,M}$ and $v^{K+1}_{L,M-1}$ seem to be unknown. The process of computation usually takes place along increasing values of indices L and M, thus when the solution is sought at the point (L,M) the new values of variable v are already known at the points (L,M-1) and (L-1,M).

To advance the solution in time, the following explicit formula is used:

$$v^{K+1}_{L,M} = \left\{ \frac{\eta T}{h^2} \left[v^{K}_{L+1,M} + v^{K+1}_{L-1,M} + v^{K}_{L,M+1} + v^{K+1}_{L,M-1} - 2v^{K}_{L,M} \right] + v^{K}_{L,M} \right\} \Big/ \left(1 + \frac{2\eta T}{h^2} \right) . \qquad (11)$$

The method presented above is closely related to the angle derivative method [*Roache, 1972*].

The influence of fast ice on the storm wave is studied through a linear viscous model of the ice internal stress. The difference between the pack ice and fast ice will be expressed through the different values of the viscosity coefficient η.

Through a comparison of the ice drift motion of the ARGOS stations set on the pack ice and the drift computed by the model, we found that for a compactness of 0.7 to 0.8 the viscosity coefficient (η) ranged from $5 \cdot 10^8$ cm^2/s to $5 \cdot 10^9$ cm^2/s.

To define the ice friction coefficient suitable for the storm surge propagation in the fast ice, the magnitude of the coefficient which will cause the ice velocity to be nearly zero must be determined. A series of experiments was carried out with the whole area of Norton Sound covered by

fast ice (c = 1) and applying a friction coefficient from the range 1 cm^2/s to 5 x 10^{12} cm^2/s. Friction through the viscous stresses suppresses the ice motion and when the ice friction coefficient attains 10^{12} cm^2/s, the ice motion is stopped (Fig. 2). Because water motion depends on the energy transfer from the atmosphere to the water through the ice cover, the high values of ice friction coefficient and ice compactness c = 1, lead to suppression of the water motion as well. The motion decreased faster at the nearshore location (Stebbins) than in the open sea region (NC17) probably due to the higher bottom friction. Fast ice never covered the whole Norton Sound area but only a narrow nearshore band, therefore the damping of the surge wave under the pack ice was only partial.

In the process of computation, instabilities are generated because of the explicit numerical formulas for the stress between ice and water. This occurs only if the velocity of ice or water attains large values. Considering the time variations of the ice velocity caused by the stress alone

$$\frac{\partial v}{\partial t} = -Rv \tag{12}$$

one can write an explicit numerical scheme

$$\frac{v_{L,M}^{K+1} - v_{L,M}^{K}}{T} = -Rv_{L,M}^{K} \tag{13}$$

which is stable when time step $T < \frac{2}{R}$.

Since R is proportional to an absolute value of ice velocity, for the larger values of velocity, the time step limit may become very short. The application of a fully implicit scheme,

$$\frac{v^{K+1}_{L,M} - v^{K}_{L,M}}{T} = -Rv^{K+1}_{L,M} \qquad (14)$$

establishes a stable numerical computation.

To find a unique solution to the set of equations (l)-(6), the boundary conditions both for the water and ice have to be specified. The boundary conditions for the equations of water motion are specified either by the radiation condition or by linear approximation of the velocities and sea level from the large scale grid model located at the boundary of the refined grid model. The boundary conditions for the ice motion are neither understood nor readily available. For the equations of ice motion we found that the best results are derived by assuming a continuity of velocity along the normal to the open boundary. In the first series of experiments, the equation of ice transport (5) was solved with known compactness along the open boundaries. An ice distribution closer to the observed one has been obtained by applying an advection equation.

$$\frac{\partial c}{\partial t} + v\frac{\partial c}{\partial x} = 0 \qquad (15)$$

along the direction (x) normal to the open boundary. Assuming the point at the boundary has coordinates L,M, the numerical form for (15)

$$\frac{C^{K+1}_{L,M} - C^{K}_{L,M}}{T} + \frac{(v + |v|)}{2}\frac{\left(C^{K}_{L,M} - C^{K}_{L-1,M}\right)}{h} + \frac{(v - |v|)}{2}\frac{\left(C^{K}_{O} - C^{K}_{L,M}\right)}{h} = 0 \qquad (16)$$

will set compactness at the boundary as a function of velocity direction. The positive v is directed out of the integration domain. C^{K}_{O} is the ice compactness outside of the domain boundary and is assumed to be known from observation; it is advected into the domain by condition (16) if the velocity across the boundary has a negative sign.

We are not able to measure the same storm surge in the summer and winter, but this is possible for the astronomical tide wave. The *sea* level recorded at Stebbins in February-March 1982 under the fast ice (Fig. 3a) and in August 1982 (Fig. 3b) displays a clear difference in the tide amplitude. The harmonic analysis (Table 1) shows that the amplitudes of the main constituents, K_1, O_1, M_2, increase from winter (H_w) to summer (H_s) by about 40%. We therefore expect an inhibitory effect on the storm surge by fast ice as well. In addition, fast ice may produce a shift in the time of arrival of the surge wave.

Results from model calculations with and without ice are given in the storm descriptions in the following section. The presence of ice does modifies the sea level distribution over time to a varying extent. The sea level is most greatly affected in the fast ice zone, and some grid points under pack ice not near the boundary do not show large differences.

4. STORM SURGES IN THE BERING SEA AND NORTON SOUND

The Bering Sea has one of the largest continental shelves in the world. The late summer and fall storms move from the south and southeast, therefore there is sufficient fetch to generate strong' variations in the sea level. The late summer storms are often caused by the low pressure centers which, in the northeastern Bering Sea, generate positive sea level changes. During the winter, the weather over the Bering Sea depends on the east Siberian high pressure system. The northeasterly winds generate negative sea levels in the Norton Sound area and the ice movement from the northeastern Bering Sea towards the south [*Muench and Ahlnas*, 1976]. Because of geographical location, two shelf regions are candidates for the

Table 1. Amplitude (11) and phase (G) of the principal tidal constituents at Stebbins, Alaska.

Constituent	Frequency CPD	Summer Amplitude (H_s) cm	Summer Phase (G_s) degree	Win_ter Amplitude (H_w) cm	Win_ter Phase (G_w) degree	H_w/H_s
Q_1	0.89324	5.01	34.8	2.91	359.4	0.58
O_1	0.92954	25.81	61.9	14.98	30.1	0.58
M_1	0.96645	1.83	89.1	1.06	61.0	0.58
P_1	" 0.99726	15.69	112.2	10.28	87.3	0.65
K_1	1.00274	47.41	1.16.3	31.07	91.9	0.65
J_1	1.03903	2.04	1.43.3	1.18	122.6	(-).58
$2N_2$	1.85969	0.96	109.6	0.92	27.0	0.96
μ_2	1.86455	1.15	11.7.7	1.11	35.7	0.96
N2	1.89598	7.21	170.3	6.91	91.3	0.96
ν_2	1.90084	1.40	178.5	1.34	100.0	0.96
M2	1.93227	19.46	231.1	13.40	155.6	0.69
L_2	1.96857	(3.54	288.4	0.38	176.8	0.70
T_2	1.99726	0.28	333.7	O*10	193.6	0.36
S_2	2,00000	4.70	338.0	1.76	195.2	0.37
K_2	2.00548	1.28	346.6	0.48	198.4	0.37

extreme sea level changes – Bristol Bay and Norton Sound. Norton Sound is situated in the northeastern region of the Bering Sea as a relatively shallow embayment of about 200 km in length. Large portions of Norton Sound have a depth less than 10 m and the average depth is about 20 m [*Muench et al.*, 1981]. During the storm dominated season from August to November, an average of 2 to 4 low pressure systems with wind velocity ranging from 15 to 25 m/s may hit the Norton Sound area. The Norton Sound shore is generally of low relief, therefore during storms, the coastal plains can be inundated by the surge or wind waves superimposed on the surge wave. There is only limited knowledge of the sea level changes along the Bering Sea coast due to the lack of permanent tide gauges. An insufficient number of observations is the main reason that the surge height computed through a statistical method, developed for Alaska shores by *Wise et al.* [1981], has to be taken as an approximate value. We have reproduced three storm surges; two are from the winter 1982 when various oceanographic and atmospheric measurements were underway by NOAA/PMEL over the northeastern shelf of the Bering Sea *[Reynolds and Pease, 1984; Mofjeld, 1984]*. After the model had been tested against sea level data both in the pack ice and the fast ice area, the largest recently recorded *storm* surge in the Bering Sea, which occurred in November 1974, was reproduced. The model has been applied to study the water motion and sea level variation as well as the ice motion and distribution. The model is able to reproduce the essential features of ice motion and distribution; i.e., polynya region at the leeward shore of St. Lawrence Island, the ice edge motions caused by the wind, and the relatively fast transport of ice from the Bering Strait region to the southeastern shelf by the so-called "race track" [*Ray and Burns*, 1981; *Shapiro and Burns*, 1975; *Thorndike and Nelson*, 1979].

4.1 *Propagation of the Surge Wave in the Ice-Covered Bering Sea*

To test the model against measurements, we have simulated two storms. The first storm was driven by a high pressure system with the center situated over East Siberia during February 12-19, 1982 which caused a negative surge in the Norton Sound area. The second storm occurred from March 7-11, 1982, with a low pressure traveling from the central Bering Sea towards the northeastern Bering Sea. The southwesterly winds generated a positive surge of about 1 to 2 m in Norton Sound. 'The Bering Sea, during February and March 1982, was partly covered by ice with typical distribution from the Navy-NOAA Joint Ice Center, Naval Polar Oceanography Center redrawn as compactness in Figure 4. We shall use two measuring stations where the sea level was recorded during the storm surge passage. One point, located at $\phi = 62°53'N, \lambda = 167°04'W$, a bottom pressure gauge (designated NC17) was situated under the pack-ice [*Mofjeld*, 1984]. The second point was located close to Stebbins, Alaska ($\phi = 63°30'N, \lambda = 162°20'W$) and the measurements were taken under the fast ice (personal comm. John Oswald). The fast ice usually covers the southern part of Norton Sound (Fig. 4), therefore the measurements at Stebbins should provide the opportunity to study the influence of fast ice on propagation of the long wave.

4.2 *Storm Surge of February 1982*

The meteorological observations at the time of the storm are described by *Reynolds and Pease [1984]. The storm* surge of February 12-19 was induced by the high pressure system *with* the center located over eastern Siberia (Fig. .S). Northeasterly winds up to 20 m/s caused a negative surge over the northeastern shelf and a positive level at the southeast end

of the Bering Sea. The numerical model reproduces a 7-day period from OOZ, 12 February to OOZ, 19 February. The surface wind used to drive the model was calculated over the entire Bering Sea every 6 hour from the surface pressure maps. The wind was linearly interpolated for the shorter time steps of the numerical computations; 6 minutes for the Norton Sound model and 2 minutes for the Bering Sea model. The wind charts every 24 h for the entire period of *storm* are plotted in Figures 6 to 12. The wind directions during the computation were fairly steady. One horizontal grid distance in the above figures is scaled to a wind speed of 10 m/s. Quasi-steady north-northeast winds generate the wind-driven current mainly along the Bering Shelf (Figs. 13-19). The southward and southwestward flow along the eastern part of the shelf after about 2-3 days is compensated by northward and northeastward flow in Anadyr Bay and Anadyr Strait. Currents in Anadyr Bay flow in the opposite direction to the wind, therefore, such flow is due to the sea level distribution. Indeed, calculations of the wind-driven motion for the constant wind in the Bering Sea showed that the model steady state is achieved after about 2 days.

The southward and southwestward flow along the eastern Bering Shelf follow the bottom and coastal contours. In the shallow embayments like Norton Sound, the flow is directed to the east along the northern shore and to the west along the southern shore. In Figures 13 to 19 one horizontal grid distance of numerical lattice is scaled to 10 cm/s of velocity, The sea level charts are plotted every 24 hours in Figures 20 to 26. Along the northeastern shelf the strongest changes occurred, and on February 16 and 17 the negative level reached about 1 m in Norton Bay.

The ice motion (Figs. 27 to 29) is much more strongly coupled to the wind magnitude and direction than the water motion. Ice velocity as high

as 1 m/s occurred within the shelf (the horizontal grid-distance in Figures 27, 28 and 29 is scaled to 10 cm/s). The north and northeast winds pushed the ice from north to south with especially hig'n velocity between St. Lawrence Island and Norton Sound; the area which is known from satellite and aircraft observation as a "*race* track".

Ice concentration (or ice compactness) is plotted after *24* hours from the onset of the computation (Fig. 30); after 120 hours, at the maximum of sea level change (Fig. 31), and at the end of the storm — 00Z Feb 19 (hour 168) (Fig. 32). Comparison of observed ice edge location before the storm and the observed and computed ice edge location after the storm show that the model is able, to predict the correct direction of the ice edge motion (Fig. 31).

To study both the ice and water motion in Norton Sound, a fine grid model of three times shorter space grid has been applied (Fig. 1). Open boundary conditions for the model were defined by linear interpolation of velocity and sea level from the large scale Bering Sea model. Smaller grid step allowed for better resolution of the bottom and coastal topography which in turn leads to better reproduction of the local surge variations. The charts of currents over the northeastern shelf throughout the entire storm are given in Figures 33 to 39. Two regions of different dynamics can be singled out from the figures: high velocity area extended throughout the entire domain from Bering Strait to the southern boundary; and Norton Sound – an area of small and variable velocities. Sea level maps are shown in Figures 40 to 46, with the lowest level of about -150 cm occurring in Norton Bay. In the vicinity of St. Lawrence IsLand, the level throughout the entire storm was close to zero. The sea level contours and the current direction tend to be parallel.

The space-time variations of the ice compactness are plotted in Figures 47 to 49. Except for the southern nearshore region of Norton Sound and Norton Bay area where fast ice ($c = 0.99$) was set as a permanent feature, the initial ice compactness was set constant everywhere ($c = 0.7$) (Fig. 47). At the northern boundary (Bering Strait) the compactness was assumed to be constant and equal to 0.9. At both the eastern and southern boundaries, the ice compactness also remained constant during computation at 0.7. The boundary ice compactness altered the distribution of ice inside the domain of integration through the advective boundary condition (16). The northeast wind is dominant during the winter, therefore, it also sets a dominant ice pattern, i.e., areas of low compactness along the north shore of the Norton Bay and a band of high compactness ($c = 0.85$) southward from the Bering Strait (Fig. 48). The influence of St. Lawrence Island on the ice distribution is also eminent; at the windward side of the island the high compactness was produced – a feature often corroborated by observations [*McNutt, 1981*]. Resultant ice distribution is closely related to the ice velocity (Figs. 50-52). Three general modes of ice motion, inferred by *Stringer and Henzler [1981]* through the observation in Norton Sound, can also be seen in the computational results i.e. , outbound ice motion, inbound ice motion and gyre. In all figures an abrupt change in the ice movement between Horton Sound and the open Bering Sea is very apparent.

In February, 1982 PMEL deployed within the Norton Sound ice drift stations, therefore we have attempted a comparison for a period of three days (February 14-17, Julian day 45-48) of observed (continuous line) and calculated (dashed line) ice floe tracks. Figure 53 depicts the results for Station 2322B and Figure 54 for Station 2321B.

Three different temporal variations of the sea level at the time of the February storm surges in Stebbins are plotted in Figure 55. Observed changes are given by a continuous line, the computed level by the stern surge model without ice cover by a dotted line, and the computed level with pack and fast ice by a dashed line. Stebbins observations were located under the fast ice, therefore the calculated sea level with fast ice show essential differences from the ice free computations. The sea level changes at NC17 during the storm surge were calculated with the pack ice cover only, and they do not show any difference from the ice free computations (Fig. 56). The time dependent sea level changes have been plotted in a few locations along the Bering Sea coast (Figs. 57-60).

4.3 Storm Surge of March 1982

Although the dominant wind pattern over the Bering Sea is related to a high pressure system, the northwesterly flow is often reversed by low pressure systems. A storm surge due to a low pressure occurred on 8 and 9 March, 1982; the model computation spans the period 18Z, March 7 to 18Z, March 10.

At the time of the storm, a few tide gauges were deployed in the Bering Sea and ice motion was monitored by ice drift stations [*Reynolds and Pease,* 1984]. Again, to compare the measured and computed sea level changes, we shall use data from Stebbins and NC17. The low pressure system comprises two or three low pressure centers which were situated over the central and eastern Bering Sea (Fig. 61). The low pressure system displayed a slow motion towards the northeast, therefore, during the first part of the storm, southwesterly winds (Fig. 62) generated a positive surge in Norton Sound. Later, when the low pressure center was located over Alaska, the

northeasterly and northwesterly winds (Figs. 63 and 64) caused a negative surge in Norton Sound.

The horizontal grid distance in Figures 62 to 64 has been scaled to 5 m/s of wind velocity. Both sea level (Figs. 65 to 67) and currents (Figs. 68 to 70), computed from the large scale model, follow the wind pattern. Storm activity, i.e., large changes of velocity and sea level are located along shallow northern and eastern regions of the Bering Sea. Although high ice velocity was observed (Figs. 71 to 73), the ice concentration after 3 days of storm remained close to the initial distribution since the winds reversed.

The model of the Norton Sound region repeats the results derived from the Bering Sea model but the picture is more detailed. Based on the fine grid model, the ice and water interaction are shown at the time of the highest sea level occurrence; about 36 hours from onset of storm, i.e., at 182, March 7. The sea level increases from zero at St. Lawrence Island to above 1 m at Norton Bay area (Fig. 74). The water motion indicates that the velocity is parallel to the sea level isolines (Fig. 75).

Initial ice distribution has been taken to be the same as in Figure 47, thus , except for the southern shore of Norton Sound and the Norton Bay area where the fast ice is located, the ice compactness over the entire region is constant and set at 0.7. The southwesterly wind produced along the northern and northeastern shores an *area* of high ice compactness ($c = 0.85$). Close to St. Lawrence Island the ice compactness has been diminished to $c = 0.55$ (Fig. 76). The regions of the fast ice stayed uniform during the entire computation since the ice velocity was negligible in these regions. The ice velocity pattern (Fig. 77) essentially follows the wind distribution.

Again, due to the flow constraints, the high velocity region is generated between St. Lawrence Island and Alaska. In this case, ice is transported into the Chukchi Sea.

To study the influence of ice cover on the storm surge propagation, the computations were performed with the ice cover and with an ice-free sea surface. The results of the computations along with the recorded sea level in Stebbins and at point **NC17** are plotted in Figures 78 and 79. Somewhat better agreement with the observed sea level variations was achieved for this case than for the February case. Between Julian day 66 and 69, we have attempted a comparison of the ice floe tracks recorded by drifting station and calculated from the ice velocity. Due to the variable and slow motion around day 69, the comparison given in Figures 80 and 81 has been possible only for the period of two days, between days 66.5 and 68.5.

4.4 Storm Surge of November 1974

This storm surge was caused by a low pressure system traveling from the Aleutian Islands to the Bering Strait. Winds of 25 m/s to 35 m/s were recorded [*Fathauer, 1978].* Along the shores of Norton Sound combined storm surge and wind waves reached as high *as* **5** m [*Sallenger, 1983].* **On** November 11, 12 and 13 coastal communities from Bristol Bay to Kotzebue Sound were severely flooded and damaged. After the storm, observations of a debris line along the Norton Sound shore by *Sallenger* [1983] showed that at all but a few locations only one debris line was found. This would indicate that the storm surge of November 1974 was the strongest in recent history, since it had incorporated older debris lines and pushed them higher. The numerical calculation spans the period from 00Z, November 10 to 00Z,

November 14. The largest flooding indicated by the model calculation occurred between day 2 and day 3 from the onset of computations, i.e. between November 12 and 13. To describe the weather pattern during the storm, the pressure distribution at 18Z, November 12 is plotted in Figure 82. The charts of wind distribution as calculated from the surface pressure are given in Figures 83 to 86. South and southwesterly winds in the range 20 to 40 m/s generated conspicuous set up (Figs. 87-90). Even in the large scale model, sea level on day 3 (Nov 13) in Norton Bay reached about 3 m. Currents as large as 1 m/s pushed the water toward the Bering Strait (Figs. 91 to 94). The surge wave did not interact with ice cover because apart from fresh ice in Norton Sound, the entire Bering Sea was ice-free. The boundary data from the large-scale model and the wind served to drive the fine-scale model. The results show how shallow water bodies such as Norton Sound enhance the surge wave. At the peak of the storm the wave reached about 5 m in Norton Bay (Fig. 95). Storm surge related currents are transporting water towards the Chukchi Sea (Fig. 96). Temporal variations of the sea level calculated for several locations along the shore show that entire coast from south (Stebbins) to north (Diomedes) was severely flooded with set up higher than 2.5 m (Figs. 97-100). In certain locations, like Nome, flooding occurred several times. Although no tide gauge observations are available to compare against computation, the magnitude of surge derived from the model compares well with debris line observation arid flood reports from Nome [*Wise et al.*, 1981].

5. CONCLUSIONS

Results from the storm surge computations show the relationships of the sea level and currents. In addition, the inclusion of fast ice in the model can produce some measurable differences in the results. The Bering Sea model reproduces several observed features of the ice distribution as well as predict the sea level changes. The polynya south of St. Lawrence Island, the movement of the ice edge and the movement of the ice in the "race-track" region are good examples. The Bering Sea model is adequate to determine the boundary conditions for the Norton Sound region model. The Norton Sound model required the specification of velocity and sea level at the open boundaries. When the model was run with only radiation conditions on those boundaries, the model did not reproduce the observed variations in sea level, due to the lack of interaction with the larger domain. The fact that the regional Norton Sound model had the boundaries in relatively shallow water appears to be the source of this difficulty. If the radiation boundary conditions can be applied in deep water, the model is less sensitive to the alongshore regions. With the boundaries specified by the Bering model, the Norton Sound model made possible a more detailed examination of the surge within the sound, particularly in the regions of small scale bathymetry near Stebbins and in Norton Bay.

ACKNOWLEDGMENTS

We are grateful for the sea level data supplied to us by: Drs. H. Mojfeld and J. Schumacher of NOAA/PMEL, J. Oswald of ITECH, R. Mitchel, D. Bain and S. Hamrick of State of Alaska, Department of Natural Resources. We are indebted to Dr. W. Stringer for preparing charts of the ice distribution and discussion essential features of the ice motion in the Bering Sea and Norton Sound. This is the final report of OCSEAP Research Unit 627, Contract Number NA-84-ABC-00225.

REFERENCES

Albright, M., Geostrophic wind calculations for AIDJEX, *Sea Ice Processes and Models,* edited by R. S. Pritchard, pp. 402-409, Univ. of Washington Press, Seattle and London, 1980.

Brewer Jr., W. A., H. W. Searby, J. L. Wise, H. F Diaz and A. S. Prechtel, Climatic atlas of the outer continental shelf waters and coastal regions of Alaska. Arctic Environmental Information and Data Center, Anchorage, Alaska, 443 pp., 1977.

Cacchione, D. A. and D. E. Drake, Sediment transport in Norton Sound, Alaska. Open-file *Rep.* 79-1555, *USGS* Menlo Park, California, 88 pp., 1979.

Camerlengo, A. L. and J. J. O'Brien, Open boundary conditions in rotating fluids, *J. Comp. Physics, 35, 12-35,* 1980.

Coon, M. D., G. A. Maykut, R. S. Pritchard, D. A. Rothrock and A. S. Thorndike, Modeling the pack ice as an elastic-plastic material, *AIDJEX Bulletin, 24,* 1-105, 1974.

Doronin, Y. P., On the method to calculate compactness and drift of ice, Trudy Arctic-Antarctic Institute, Leningrad, T., *291,* 5-17, 1970.

Drake, D. E., D. A. Cacchione, R. D. Muench and C. H. Nelson, Sediment transport in Norton Sound, Alaska, *Marine Geology, 36, 97-126, 1980.*

Fathauer, T. F., A forecast procedure for coastal floods in Alaska, NOAA Tech. *Memo, NWS AR-23, 27* pp., 1978.

Hansen, W., Hydrodynamical methods applied to the oceanographical problems. Proc. Symp. Math.-Hydrodyn. Meth. Phys. Oceanography* Mitt. Inst. Meeresh., Univ. Hamburg, *1,* 25-34, 1962.

Henry, R. F., Storm surges in the southern Beaufort Sea, *Inter. Rept.* , Beaufort Sea Project. Institute of Ocean Sciences, Patricia Bay, Sidney, B.C., Canada. 41 p?., 1974.

Hibler, W. D., Modelling pack ice as a viscous-plastic continuum, *J. Phys. Oceanogr.*, *9*, *815-846, 1979.*

Kowalik, Z., A study of the M2 tide in the ice-covered Arctic Ocean. Modeling, identification, control, *Norwegian Research Bull.*, 2(4), 201-223, 1981.

Kowalik, Z., Storm surges in the Beaufort and Chukchi Seas, *J. Geophys. Res.*, *89*(C11), 10,570-10,578, 1984.

Kowalik, Z. and J. B. Matthews, The M_2 tide in the Beaufort and Chukchi Seas, *J. Phys. Oceanogr.*, 12(7), 743-746, 1982.

Leavitt, E., Surface-based air stress measurements made during AIDJEX, in Sea *Ice Processes and Models,* edited by R. S. Pritchard, pp. 419-329, **Univ.** of Washington Press, Seattle, 1980.

Leendertse, J. J. and S. K. Liu, Modeling of tides and circulations *of* the Bering Sea, Environmental Assessment of the Alaska Continental Shelf Annual Rept. of P.I. V. 5: Transport, NOAA, pp. 87-108, 1981.

Macklin, S. A., Wind drag coefficient over first-year sea ice in the Bering Sea, *J. Geophys. Res.*, *88*(C5), 2845-2852, 1983.

Marchuk, G., R. Gordev, B. Kagan and V. Rivkind, Numerical method to solve tidal dynamics equation and result of its testing, 78 pp., Report Comput. Centre, Novosibirsk, U.S.S.R., 1972.

McNutt, L. S., Remote sensing analysis of ice growth and distribution in the eastern Bering Sea, in *The Eastern Bering Sea Shelf: Oceanography and Resources,* edited by D. W. Hood and A. Calder, pp. 141-165, Univ. of Washington Press, Seattle, 1981.

Mofjeld, H. O., Recent observations of tides and tidal currents from the northeastern Bering Sea shelf, *NOAA Tech. Mem. ERL PMEL-57*, *36* pp., PMEL, Seattle, 1984.

Muench, R. D. and K. Ahlnas, Ice movement and distribution in the Bering Sea from March to June 1974, *J. Geophys. Res.*, 81(24), 4467-4476, 1976.

Muench, R. D., R. B. Tripp and J. D. Cline, Circulation and hydrography of Norton Sound, in The *Eastern Bering Sea Shelf: Oceanography and* Resources," edited by D. W. Hood and A. Calder, pp. 77-93, Univ. of Washington Press, Seattle, 1981.

Overland, J. E., H. O. Mofjeld and C. H. Pease, Wind-driven ice motion in a shallow sea, *J. Geophys. Res., 89*(C4), *6525-6531, 1984.*

Pearson, C. A., H. O. Mofjeld and R. B. Tripp, Tides of the eastern Bering Sea shelf, in The *Eastern Bering Sea Shelf: Oceanography and Resources,* edited by D. W. Hood and A. Calder, pp. 111-130, Univ. of Washington Press, Seattle, 1981.

Pease, C. H. and J. E. Overland, An atmospherically driven sea-ice drift model for the Bering Sea, *Annals of Glaciology, 5, 111-114,* 1984.

Ray, V. M. and W. R. Dupré, The ice-dominated regimen of Norton Sound and adjacent areas of the Bering *Sea,* in *The Eastern Bering Sea Shelf: Oceanography and Resources,* edited by D. W. Hood and A. Calder, pp. 263-278, U.S. GPO and Univ. of Washington Press, Seattle, 1981.

Raymond, W. H. and H. L. Kuo, A radiation boundary condition for multi-dimensional flow, *Quart. J. R. Met. Sot., 110, 535-551,* 1984.

Reid, R. O. and B. R. Bodine, Numerical model for storm surges in Galveston Bay, *J. Waterway and Harbour Div., 94*(WWI), *33-57,* 1968.

Reynolds, M. and C. H. Pease, Drift characteristics of northeastern Bering Sea ice during 1982, *NOAA Tech. Mere. ERL PMEL-55*, 135 pp., PMEL, Seattle, 1984.

Roache, P. J., *Computational Fluid Dynamics*, *446* pp., Hermosa Pub., Albuquerque, 1972.

Rothrock, D. A., The kinematics and mechanical behaviour of pack ice: the " state of subject, *AIDJEX Bull.*, 2, 1-10, 1970.

Rothrock, D. A., The mechanical behavior of pack ice. *Annual Rev. of Earth and Planetary Sciences, 3, 317-342, 1975.*

Sallenger, A. J., Jr., Measurements of debris-line elevations and beach . profiles following a major storm: Northern Bering Sea coast of Alaska. *Open-file Rep. 83-394, USGS,* Menlo Park, California, 1983.

Schumacher, J. D. and R. B. Tripp, Response of northeast Bering Sea shelf waters to *storms, EOS,* 60(46), 1979.

Shapiro, L. H. and J. J. Burns, Satellite observations of sea ice movement in the Bering Strait region, in *Climate* of *the Arctic,* edited by G. Weller and S. Bowling, pp. 379-386, Geophysical Institute, University of Alaska, Fairbanks, 1975.

Stringer, W. J. and R. D. Henzler, Ice replacement vectors measured in Norton Sound and the adjacent Bering Sea, 1973-1979, *Rep. for NOAA-OCSEAP, 37* pp., 1981.

Thor, D. R. and C. H. Nelson, A summary of interacting, surficial geologic processes and potential geological hazards in the Norton Sound Basin, northern Bering Sea. Proc. 11th Ann. offshore Tech. Conf. OTC, paper 3400:377-365, 1979.

Walter, B. A. and J. E. Overland, Air-ice drag coefficients for first-year sea ice derived from aircraft measurements, *J. Geophys. Res., 89 (C3), 3550-3560, 1984.*

Wise, J. L., A. L. Comiskey and D. Becker, Jr., Storm surge climatology and forecasting in Alaska. Arctic Envir. Inform. and Data Center. Univ. Alaska, Anchorage, 26 pp., 1981.

FIGURES

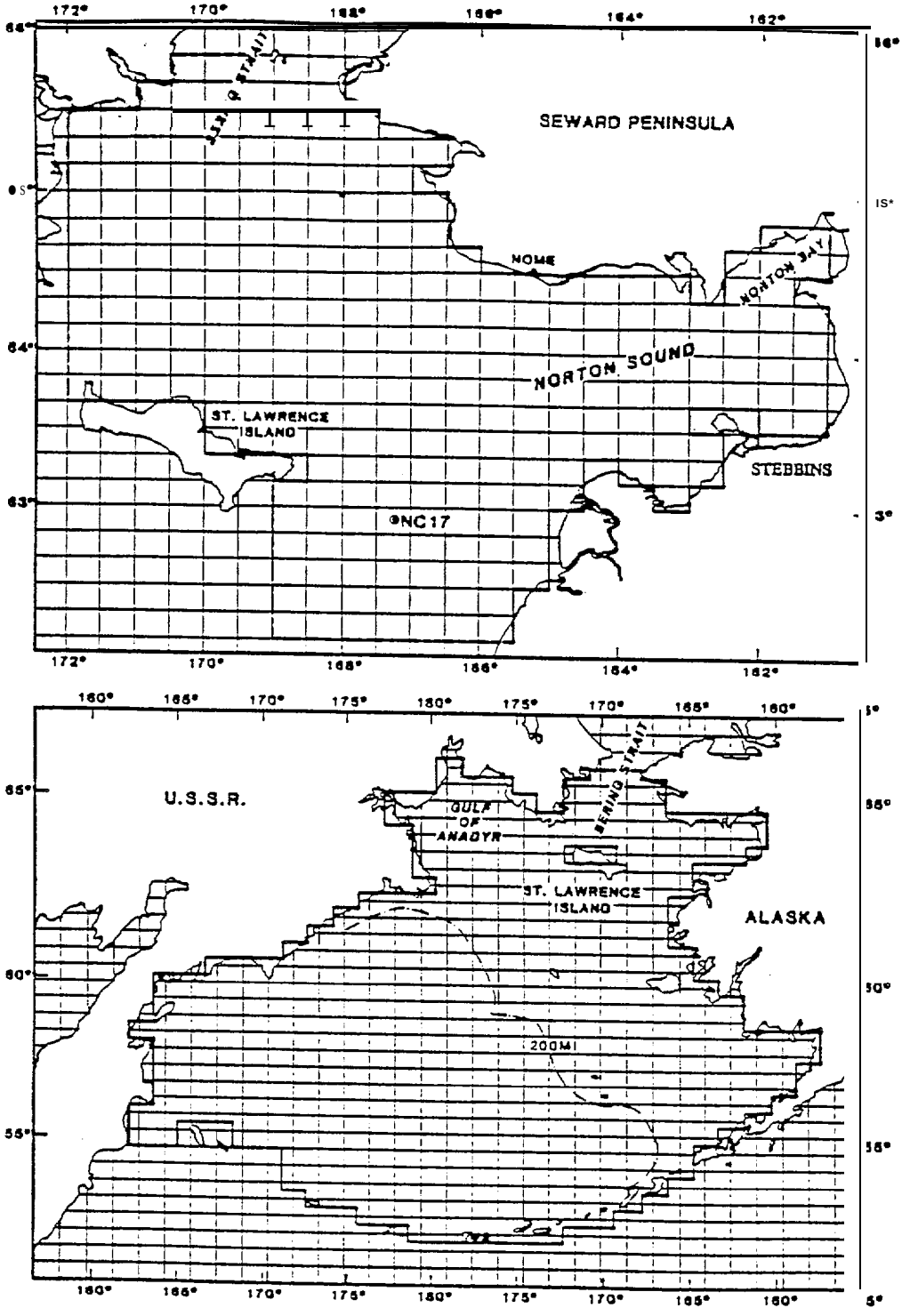

FIG.1

Chart showing model regions. The upper panel is the grid used for the detailed Norton Sound model. The lower panel is the grid used for the Bering Sea model.

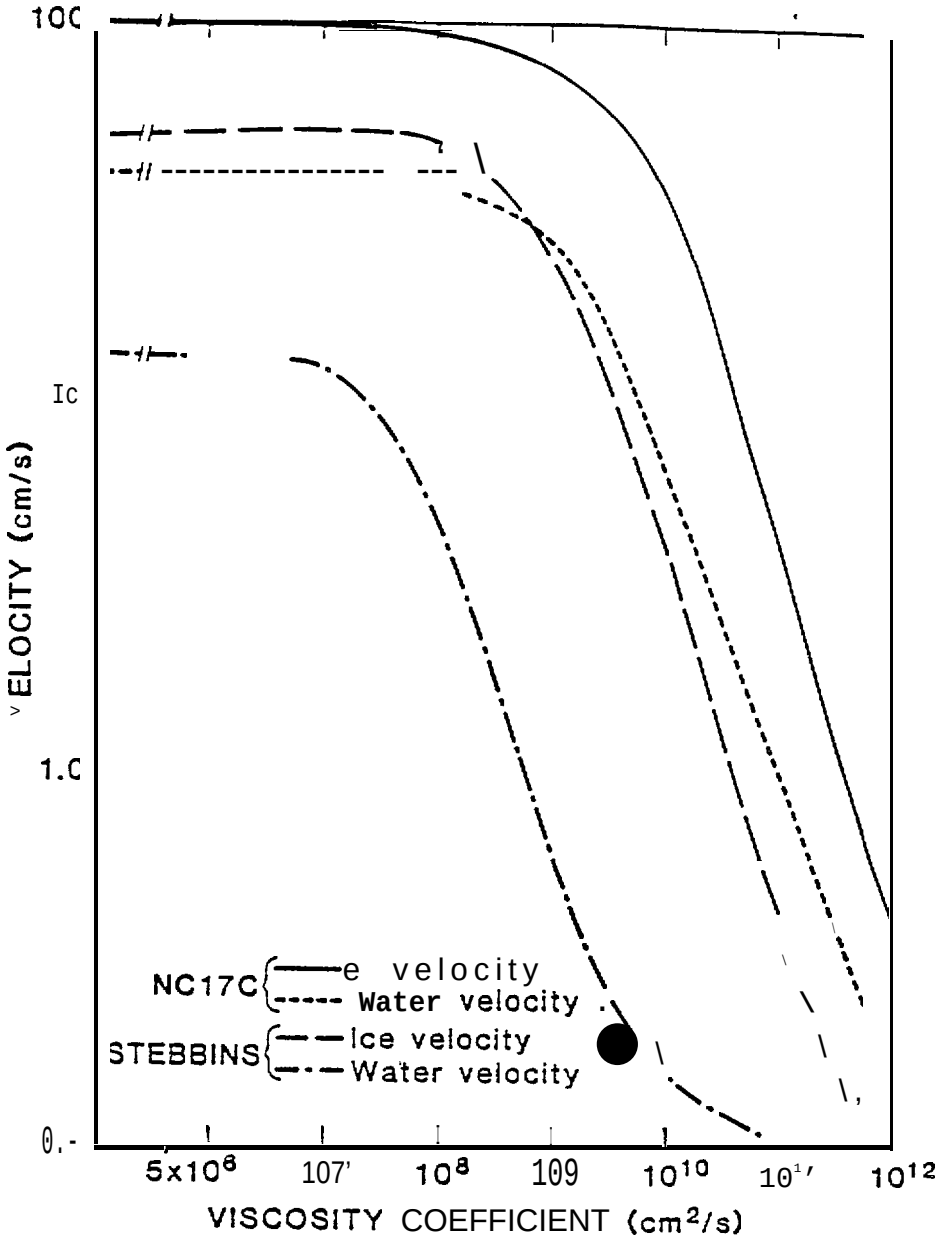

FIG. 2

Water and ice velocity as a function of the viscosity coefficient of the ice. The domain is covered by ice with 0.99 compactness.

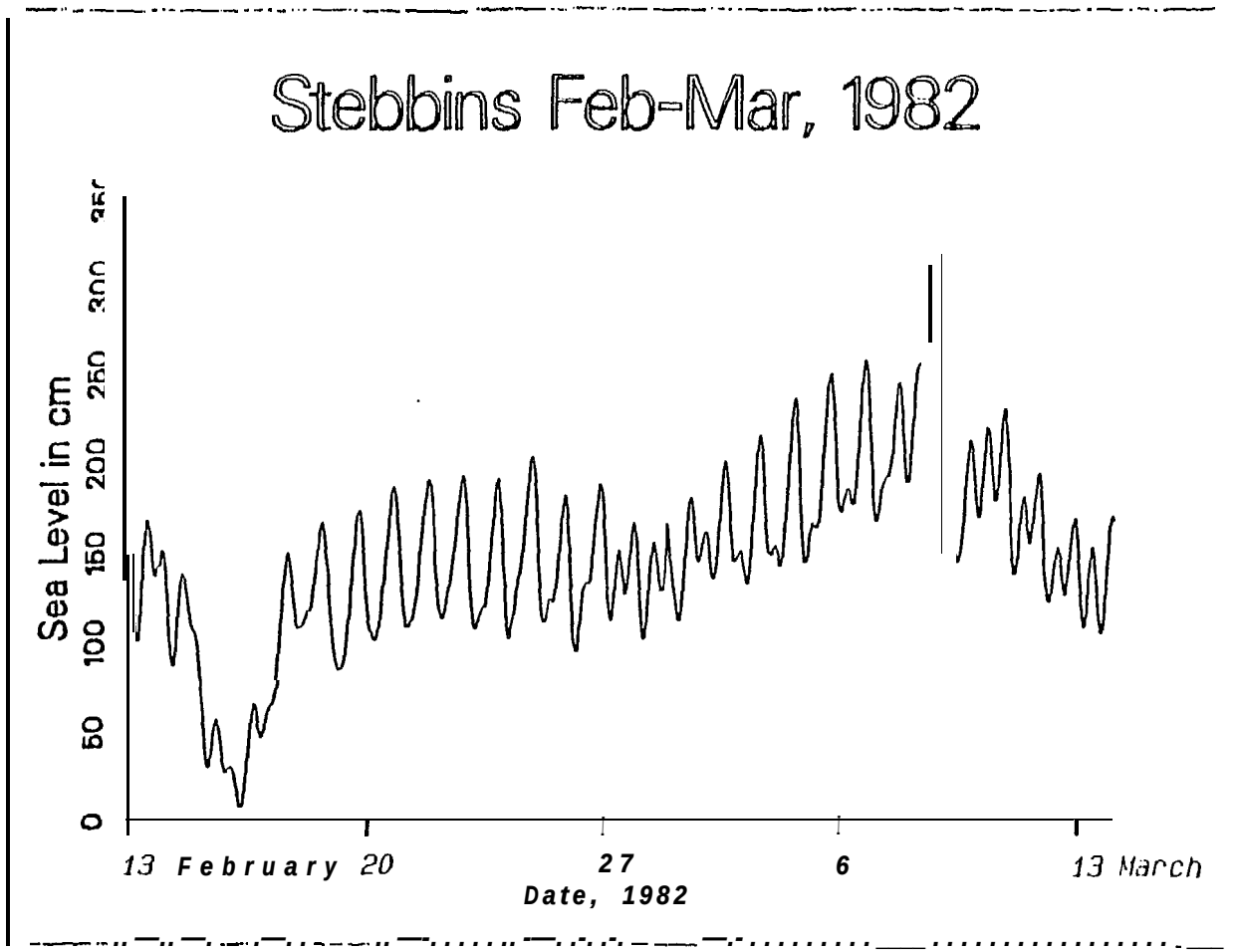

FIG. 3a

Time series of sea level measurements from Stebbins, Alaska, February and March, 1982.

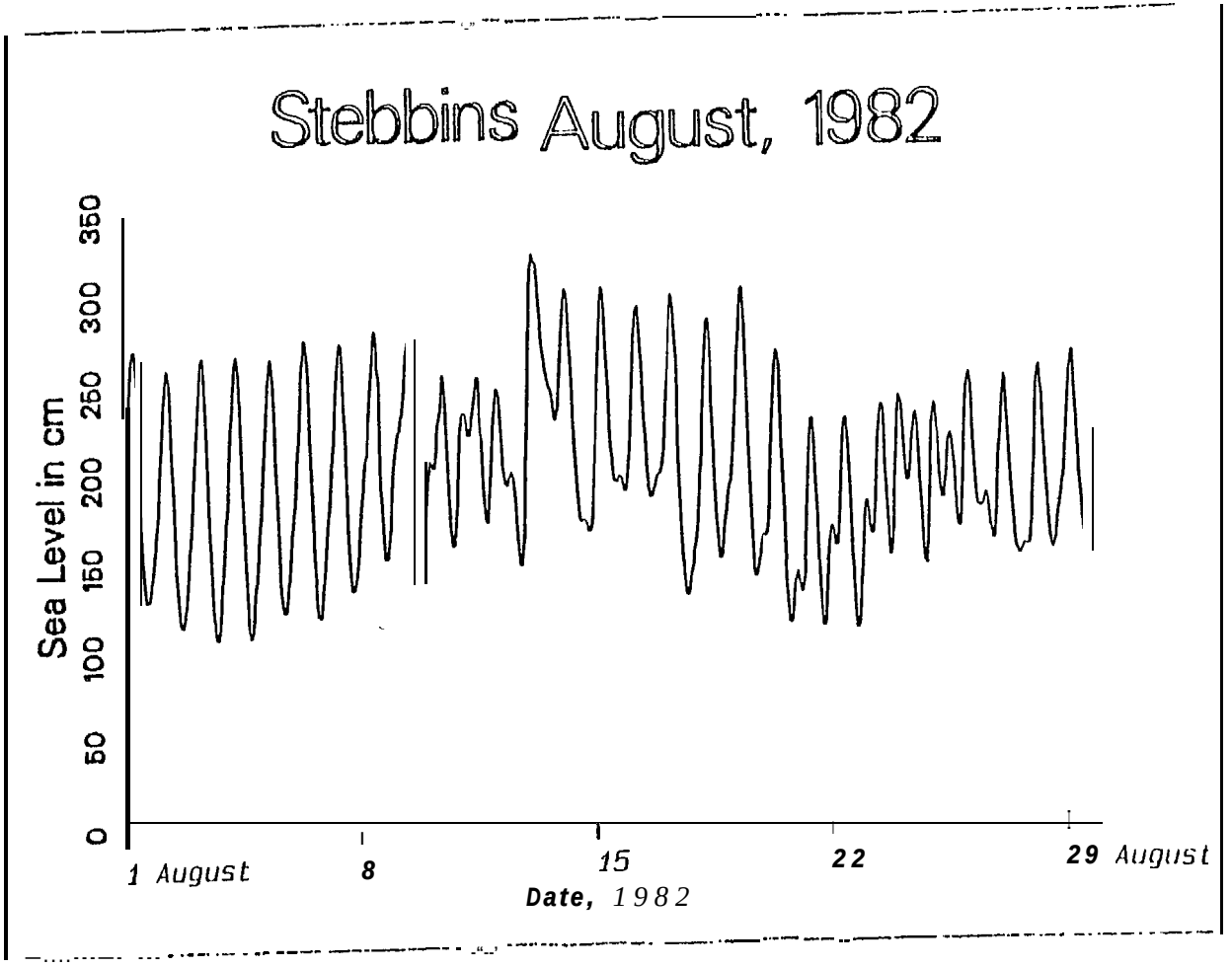

FIG. 3b

Time series of sea level measurements from Stebbins, Alaska, August, 1982.

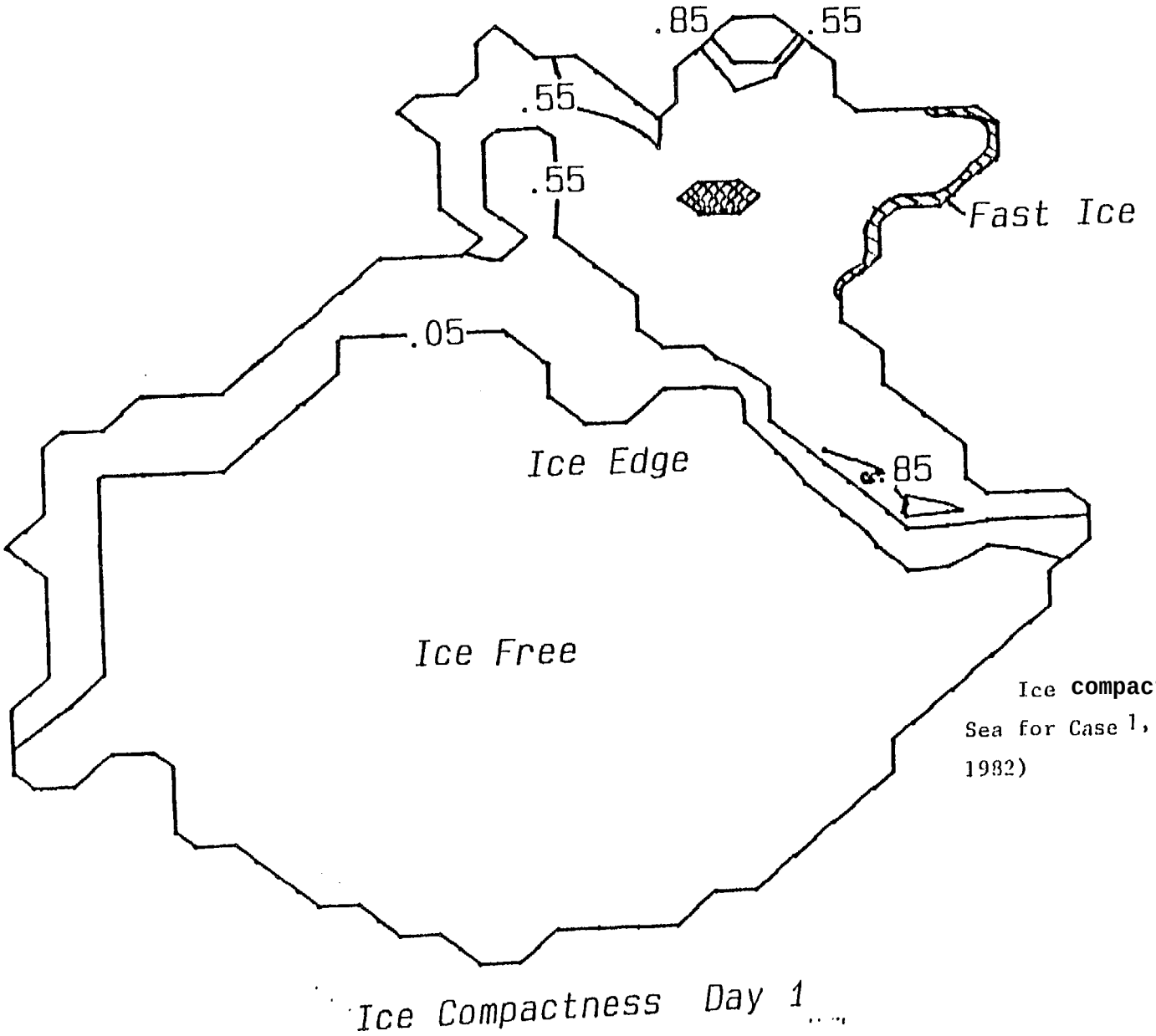

FIG.4

Ice compactness in the Bering Sea for Case 1, Day 1 (February 13, 1982)

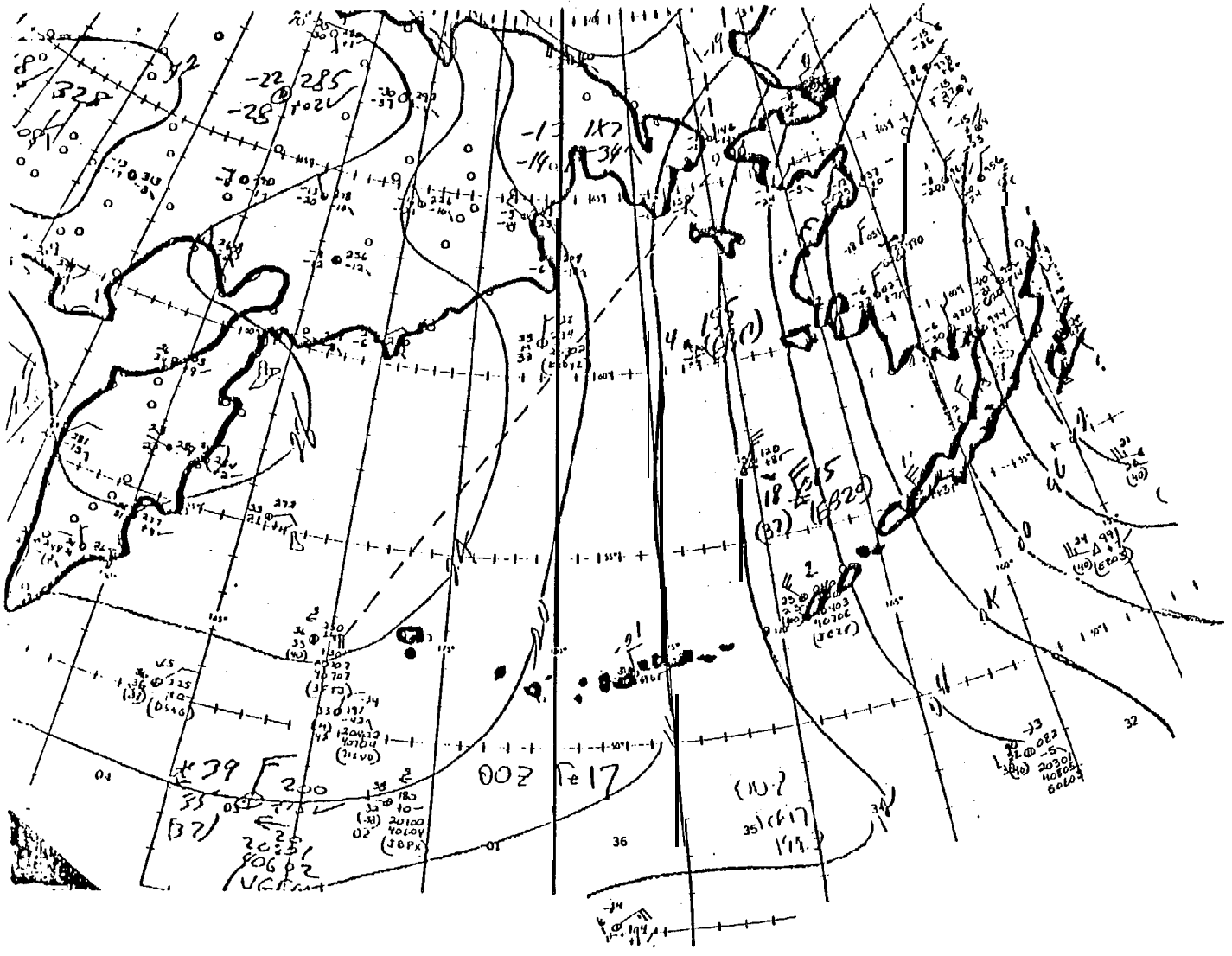

FIG.5

Surface weather chart for 00Z, 17 Feb., 1982. Pressure is given in millibars.

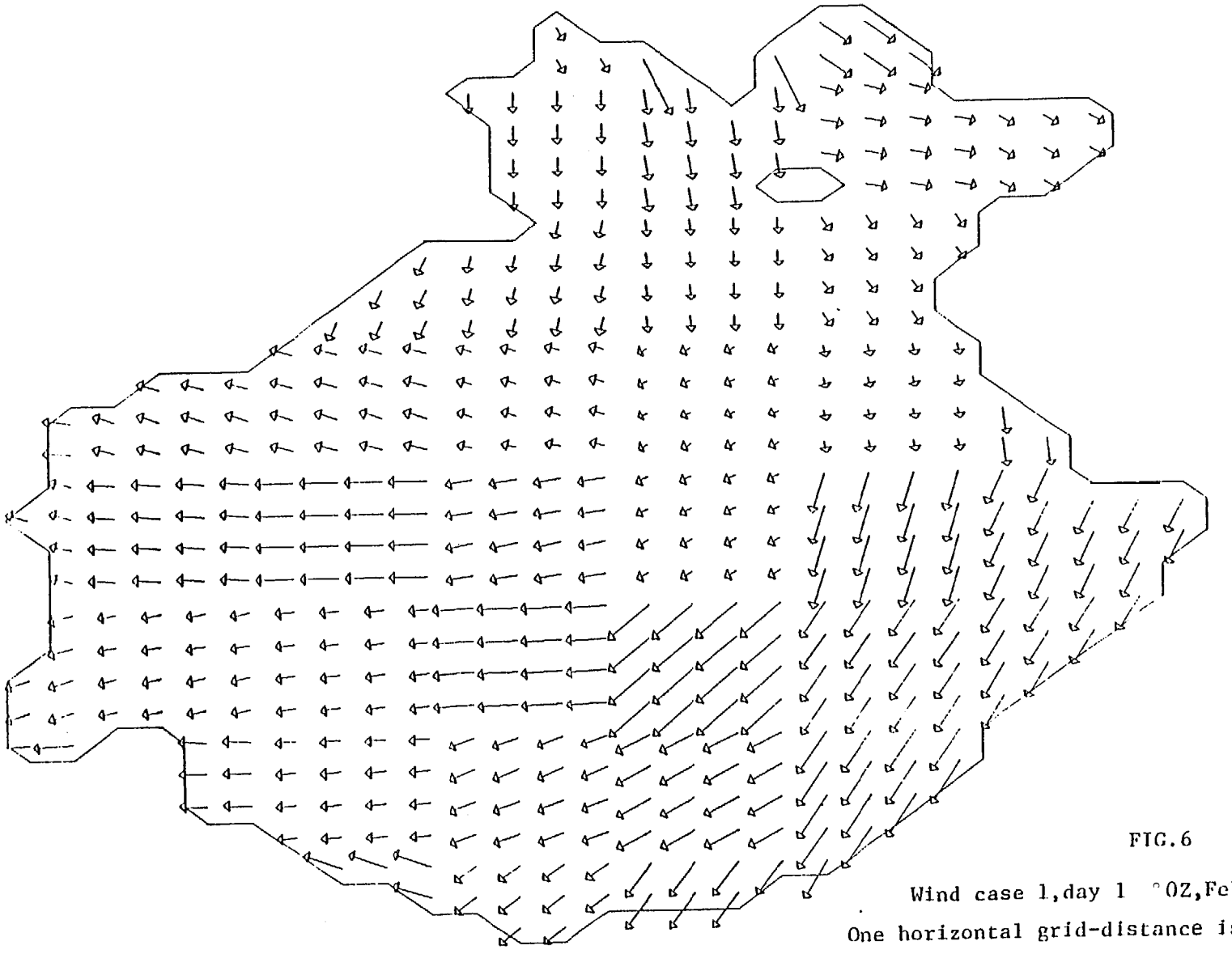

FIG.6

Wind case 1,day 1 °0Z,Feb 3, 982).
One horizontal grid-distance is scaled to10m/s.

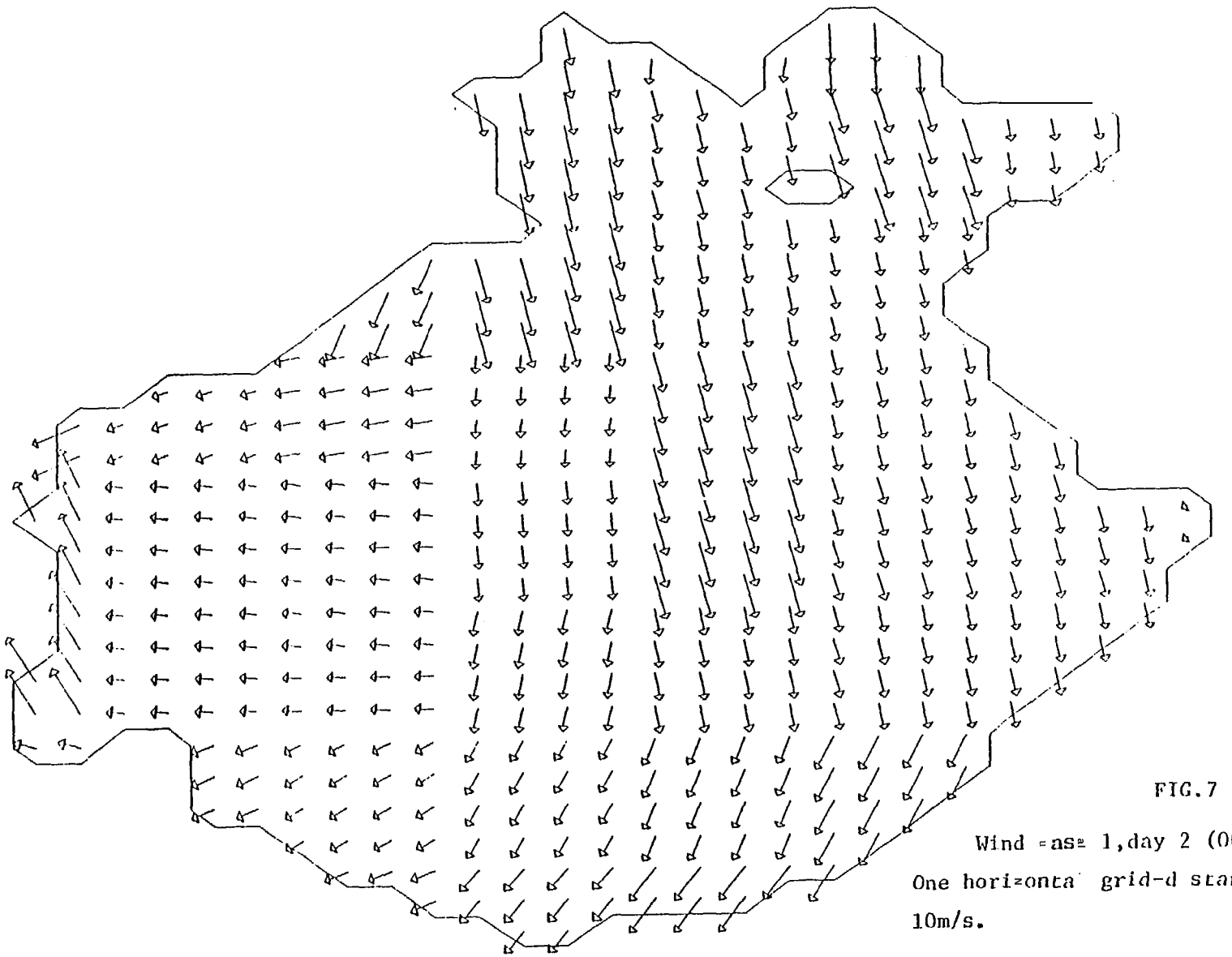

FIG.7

Wind =as= 1,day 2 (00Z,Feb.14,1982)
One hori=onta' grid-d stance is scal=d to 10m/s.

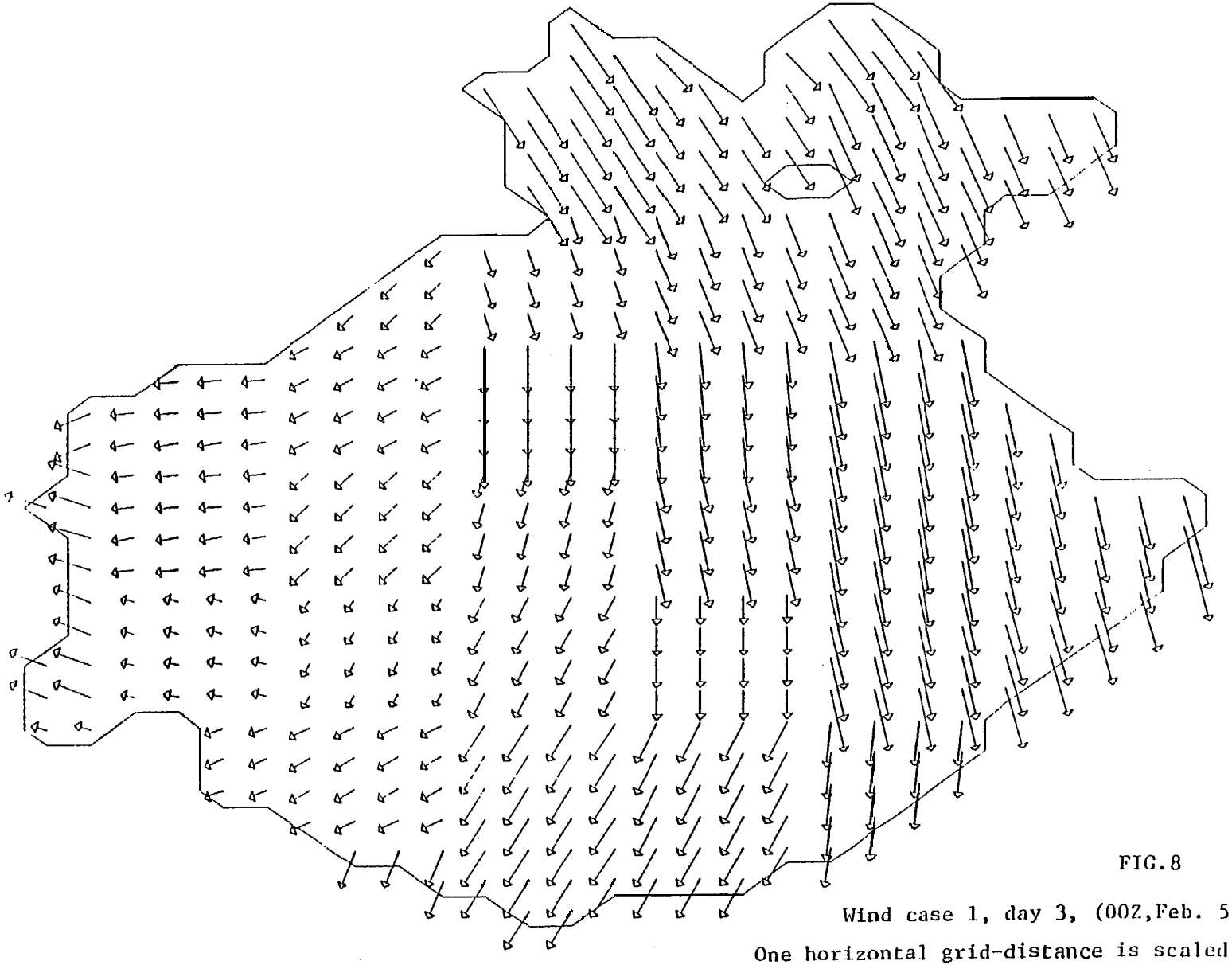

FIG.8

Wind case 1, day 3, (00Z,Feb. 5,1982)

One horizontal grid-distance is scaled to 10m/s.

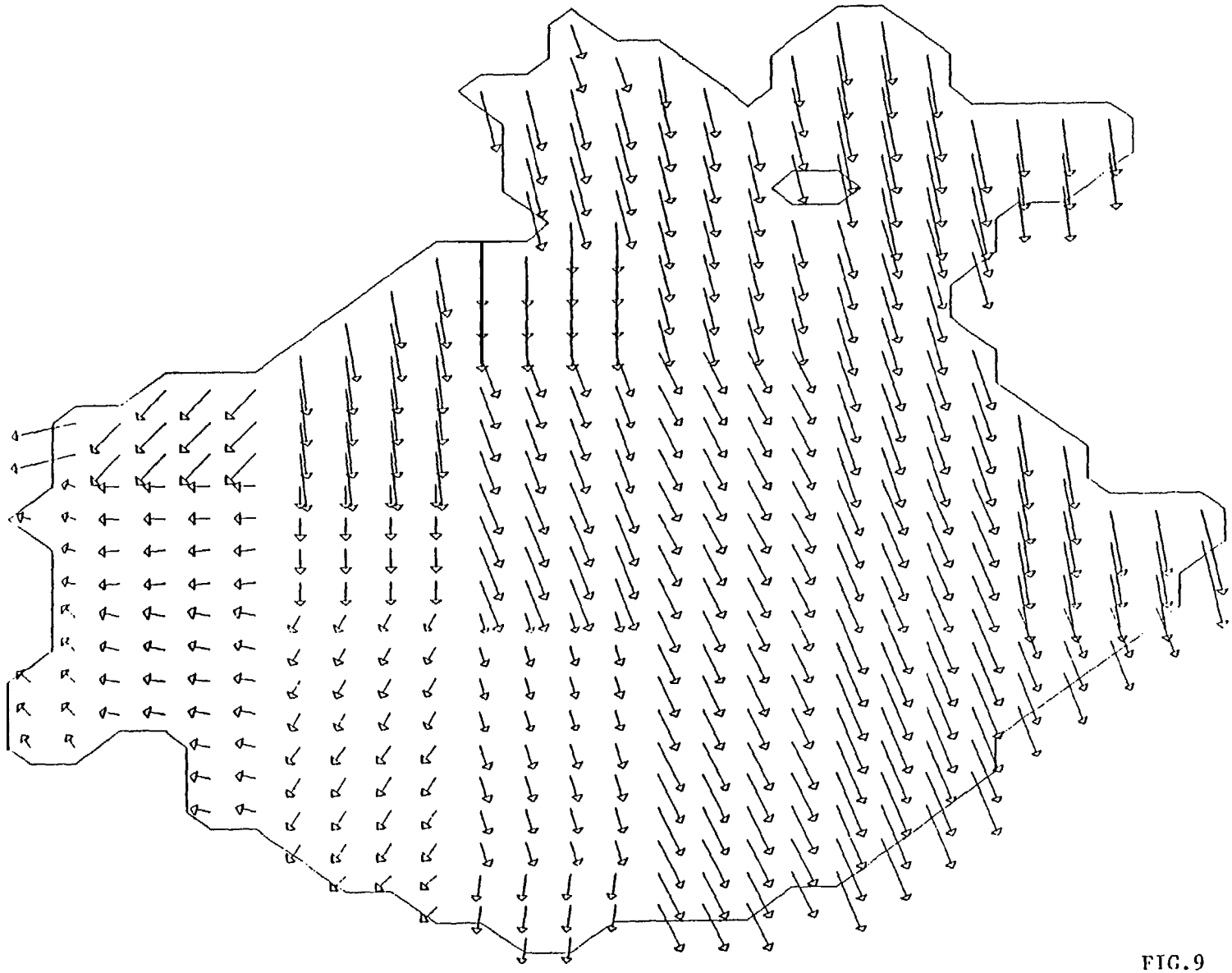

FIG.9

Wind case 1,day 4 (00Z,Feb.16,1982)

One horizontal grid-distance is scaled to 40 0m/s.

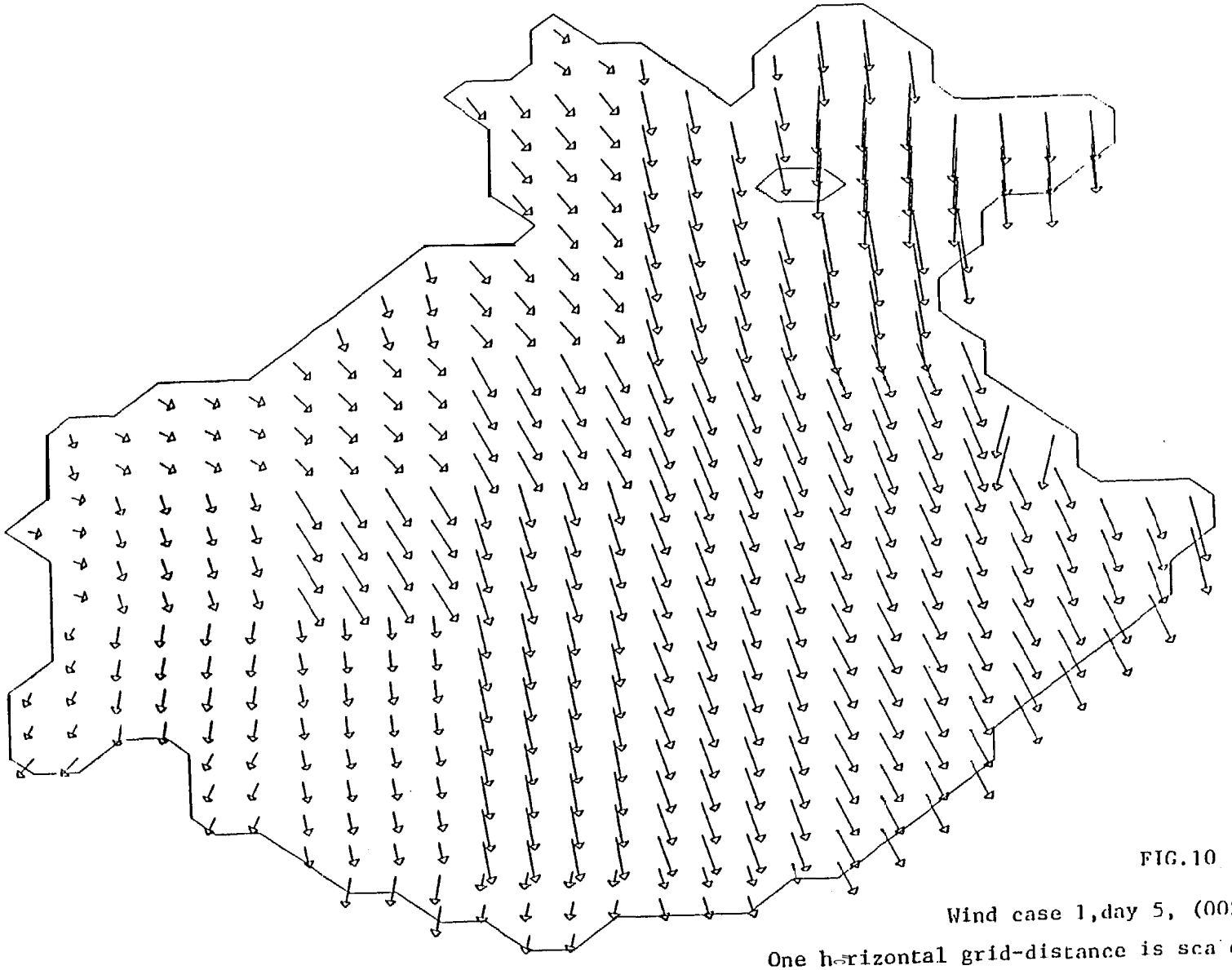

FIG.10

Wind case 1,day 5, (00Z,Feb.17,1982)

One horizontal grid-distance is scaled to 0[illegible]s.

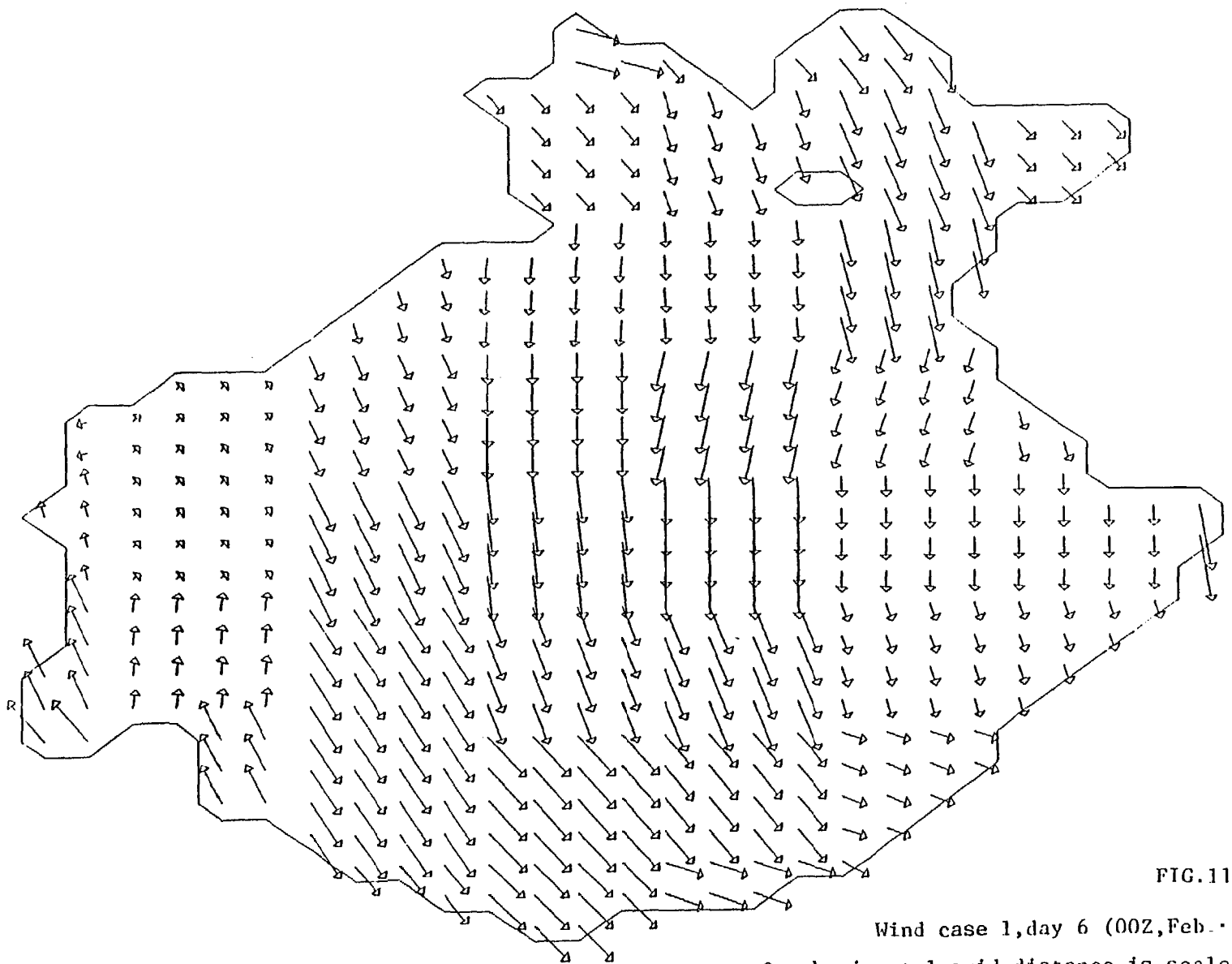

FIG.11

Wind case 1,day 6 (00Z,Feb. · ×, 982)

One horizontal grid-distance is scaled to 10m/s.

WIND 144 HOURS

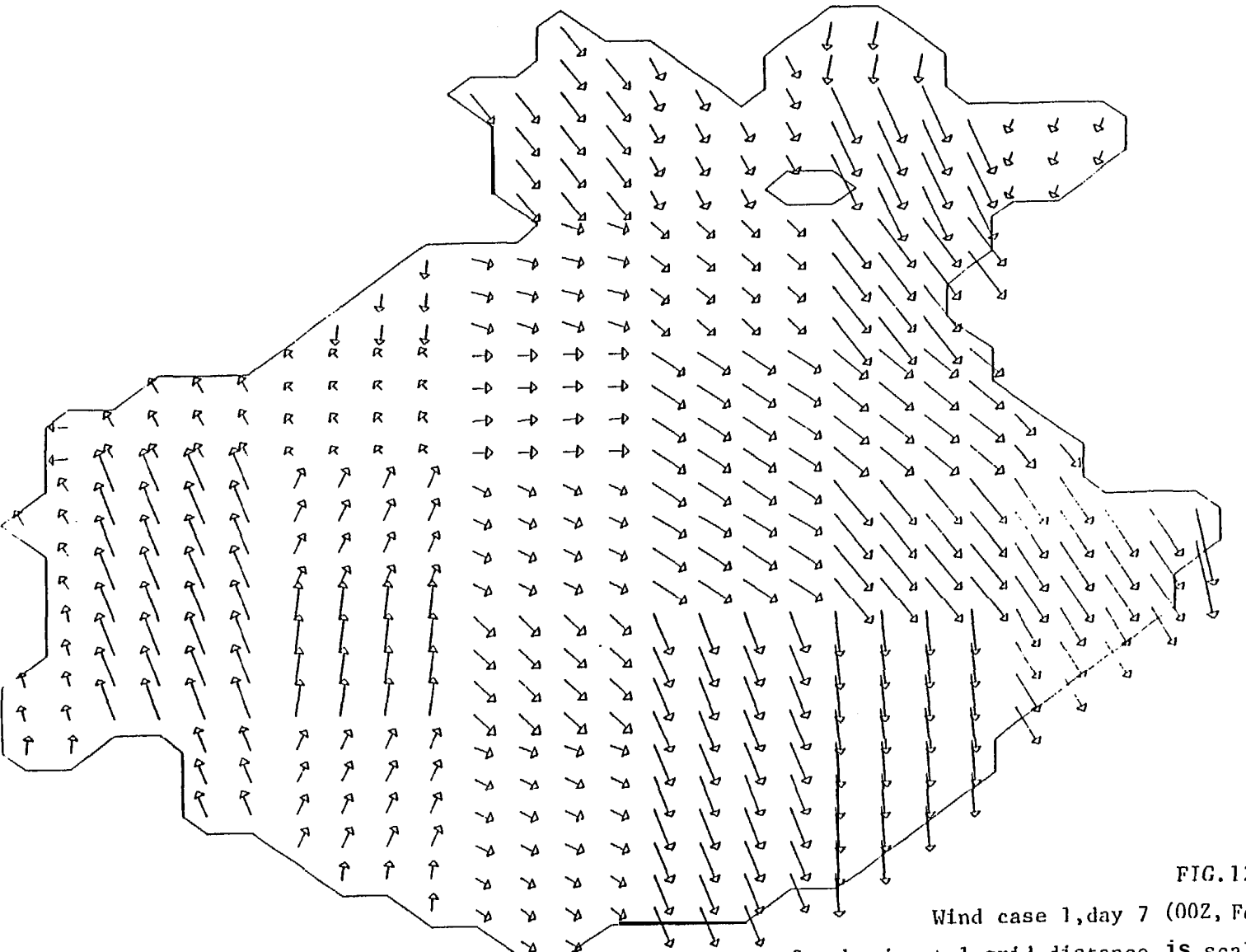

FIG.12

Wind case 1,day 7 (00Z, Feb. 19,1982)

One horizontal grid-distance is scaled to 10m/s.

WIND 168 HOURS

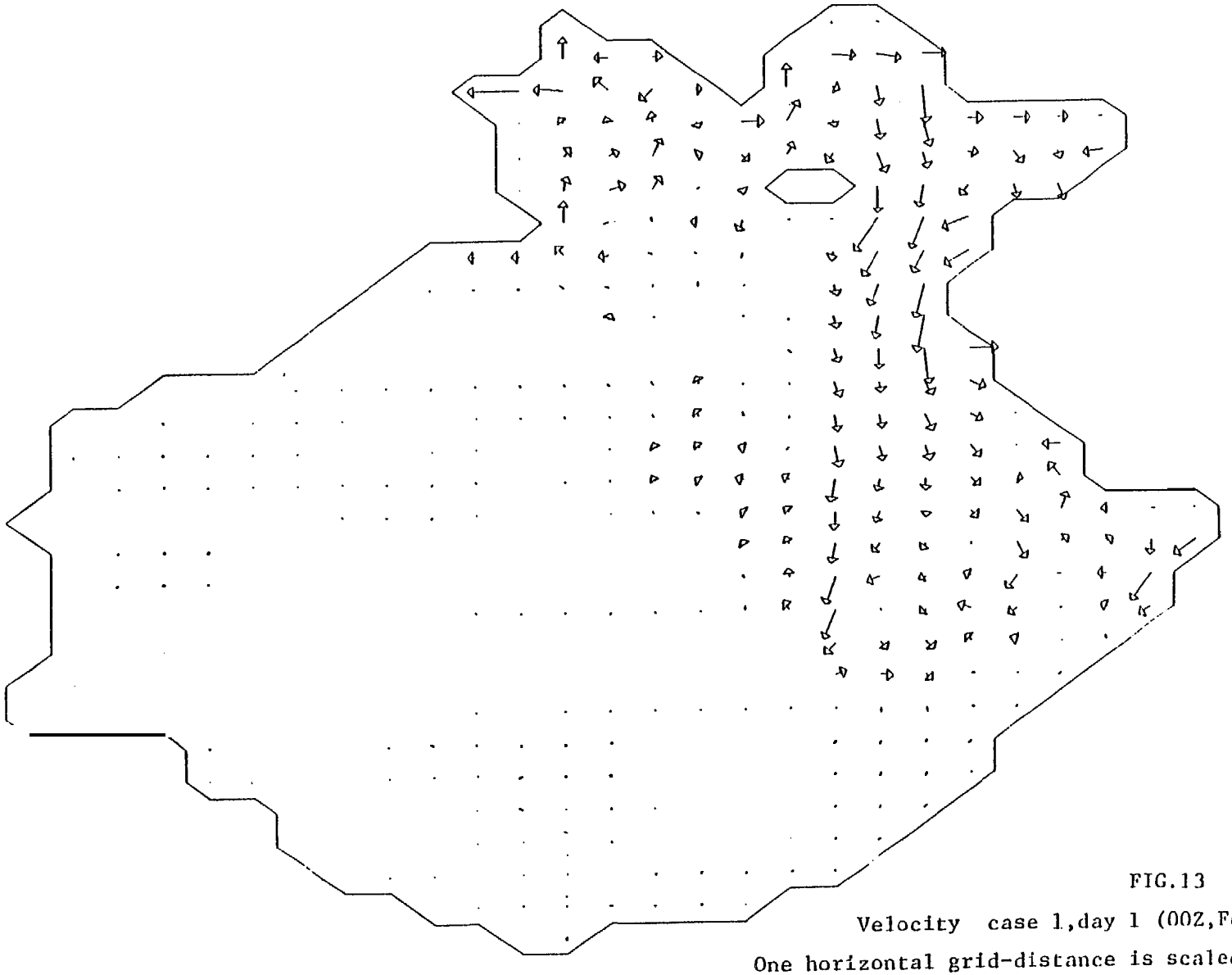

FIG.13

Velocity case 1,day 1 (00Z,Feb. 3, 982)

One horizontal grid-distance is scaled to 10cm/s.

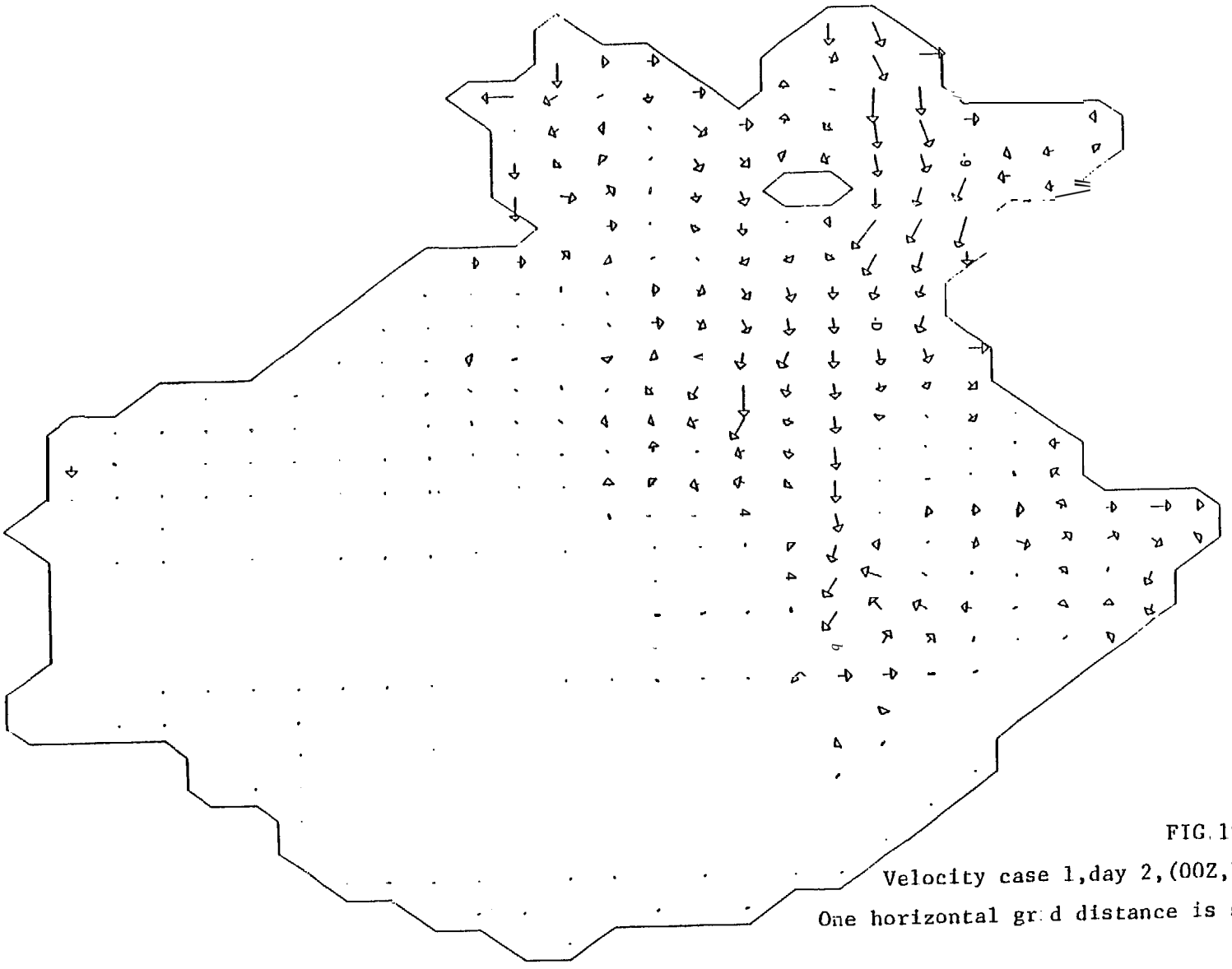

FIG. 1=

Velocity case 1, day 2, (00Z, Feb. 1=, 1982)

One horizontal grid distance is scaled to 10cm s.

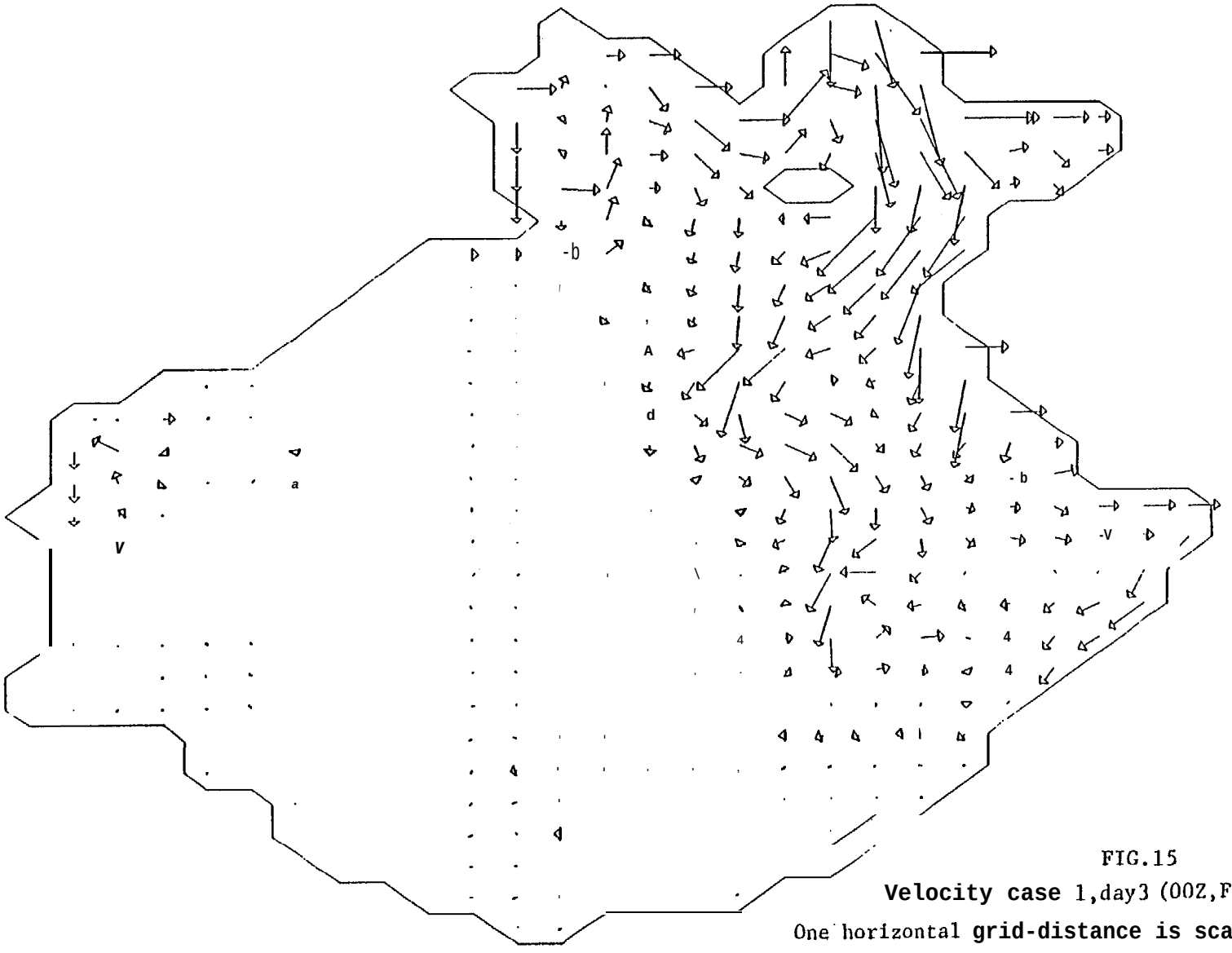

FIG.15

Velocity case 1,day3 (00Z,Feb.15,1982)

One horizontal **grid-distance is scaled. to** 10cm/s.

V 72 HOURS

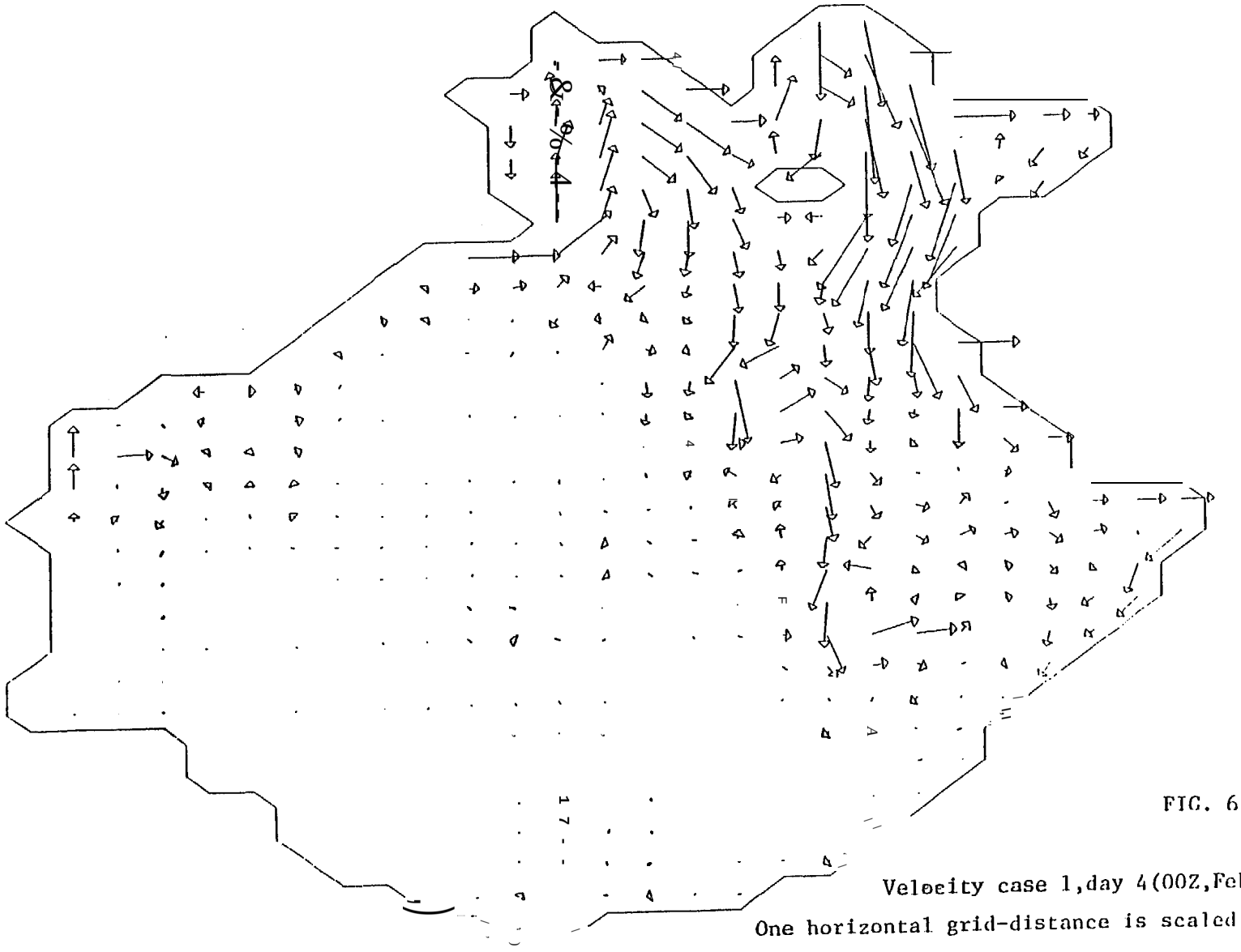

FIG. 6

Veloeity case 1,day 4(00Z,Fel 6. 982)
One horizontal grid-distance is scaled to 10cm/s.

V 96 HOURS

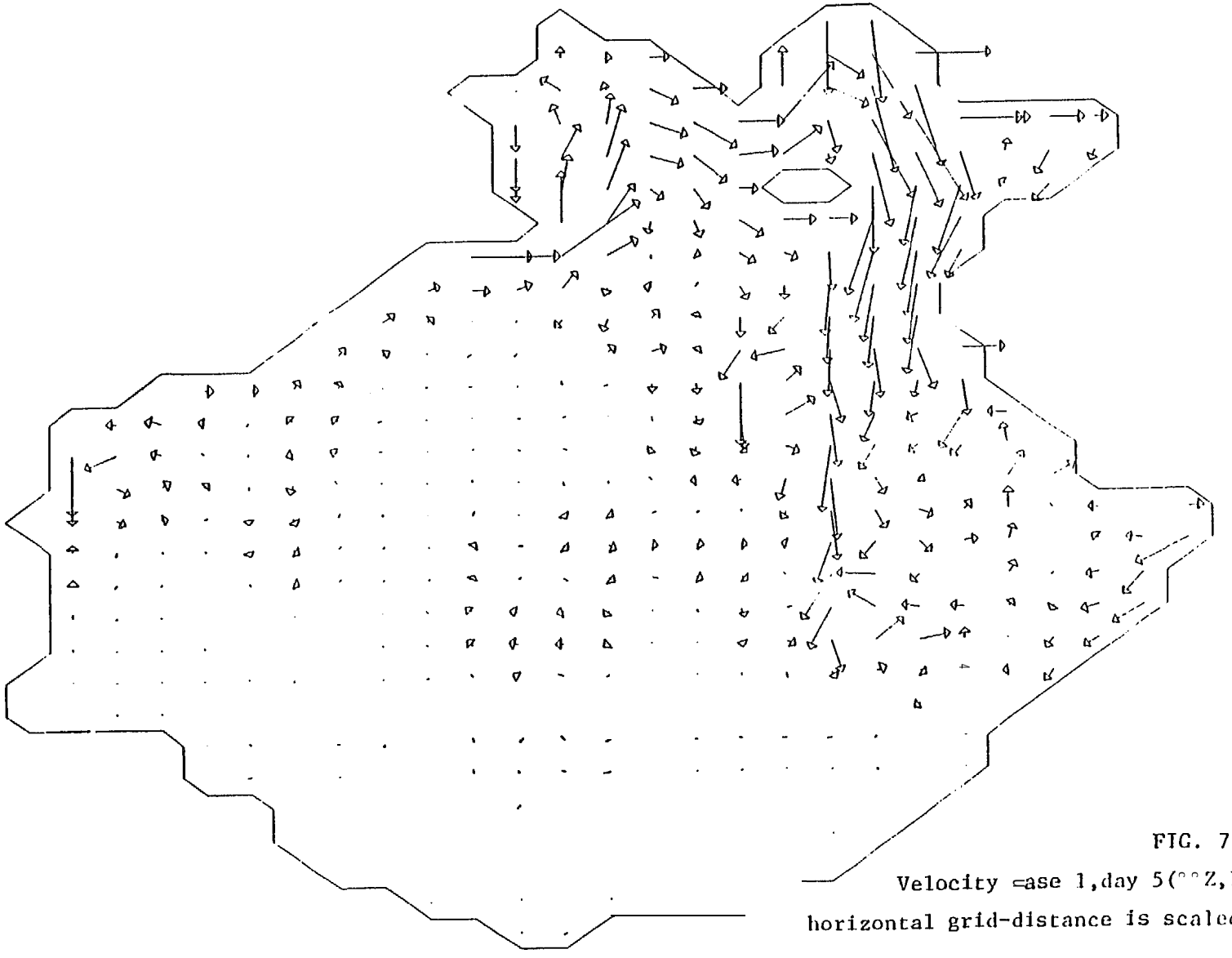

FIG. 7

Velocity case 1, day 5 (00Z, Feb. 17, 1982)

horizontal grid-distance is scaled to 0cm/s

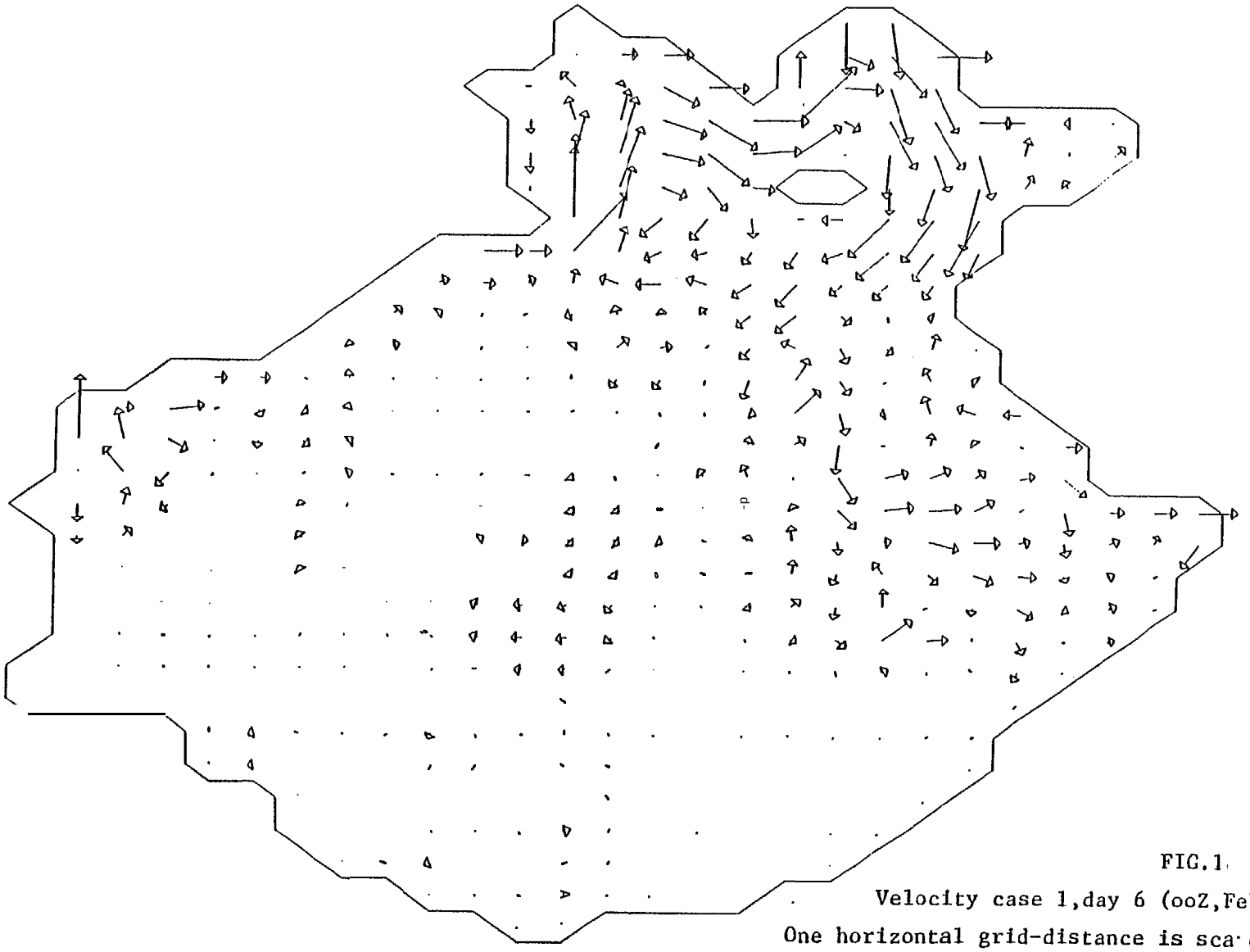

FIG.1

Velocity case 1,day 6 (ooZ,Feb.18,1982)

One horizontal grid-distance is sca·ed·to 10cm/s.

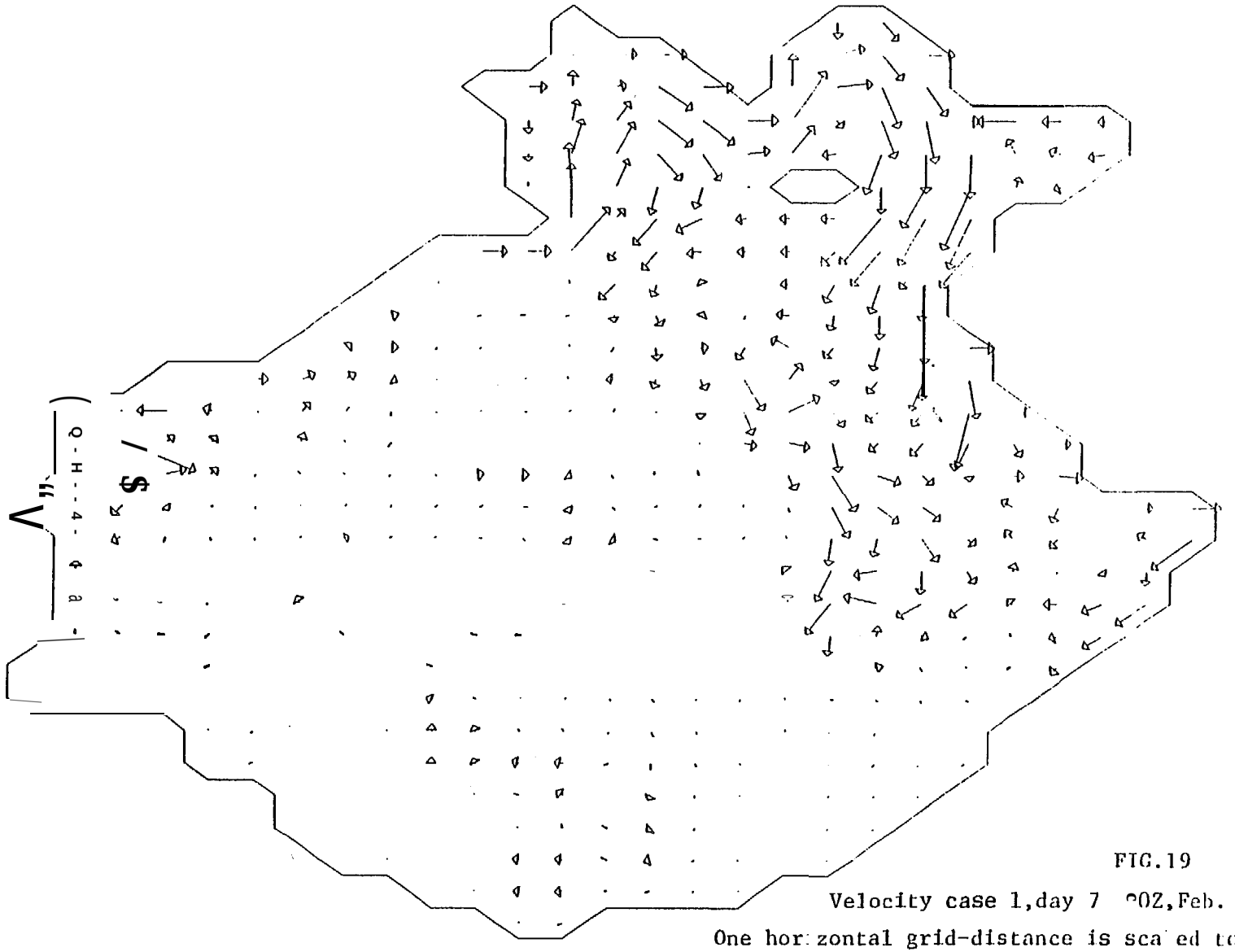

FIG.19

Velocity case 1,day 7 (02Z,Feb. 9, 982)

One horizontal grid-distance is scaled to 10cm/s.

V 168 OURS

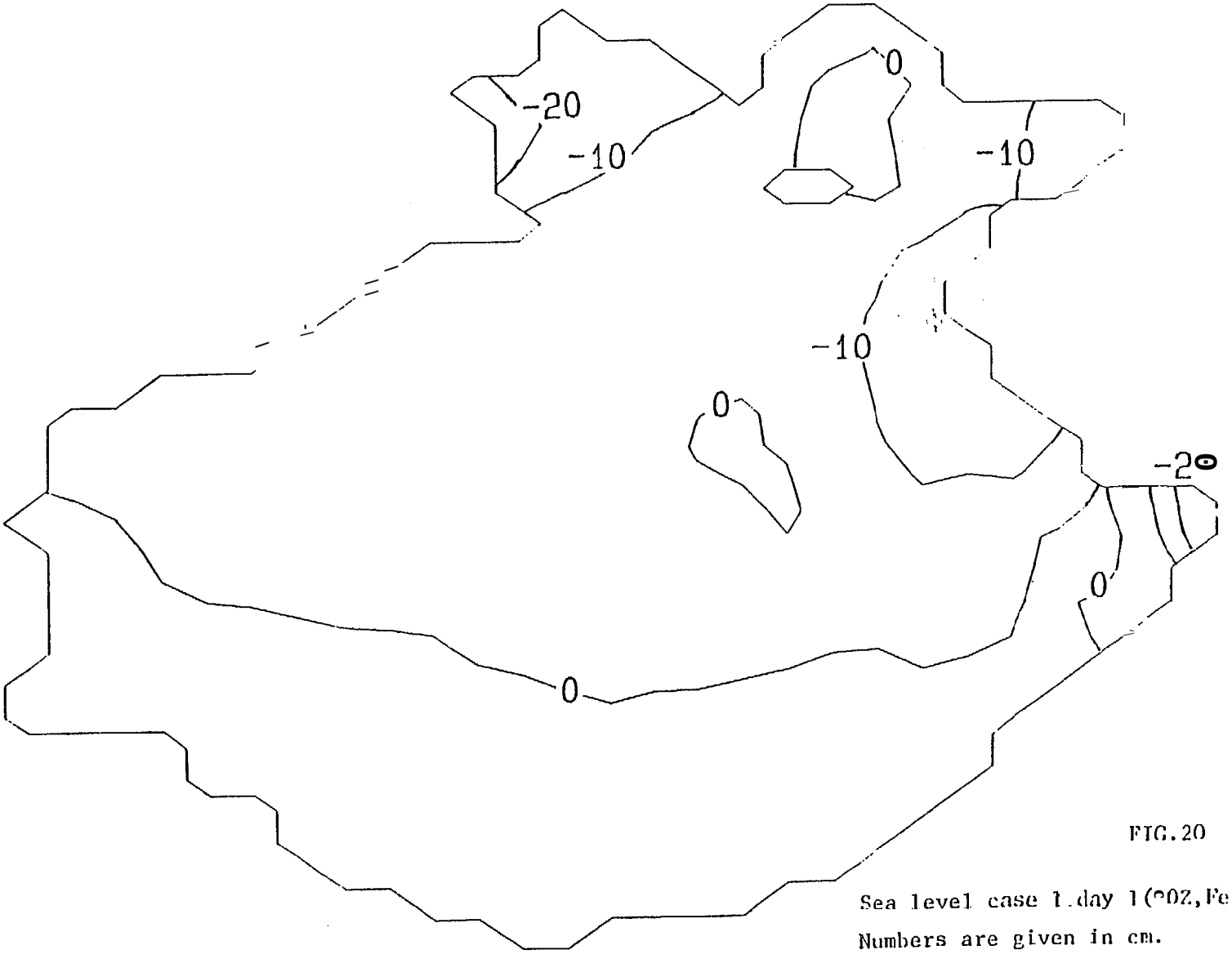

FIG.20

Sea level case 1 day 1 (00Z, Feb. 13, 1982)
Numbers are given in cm.

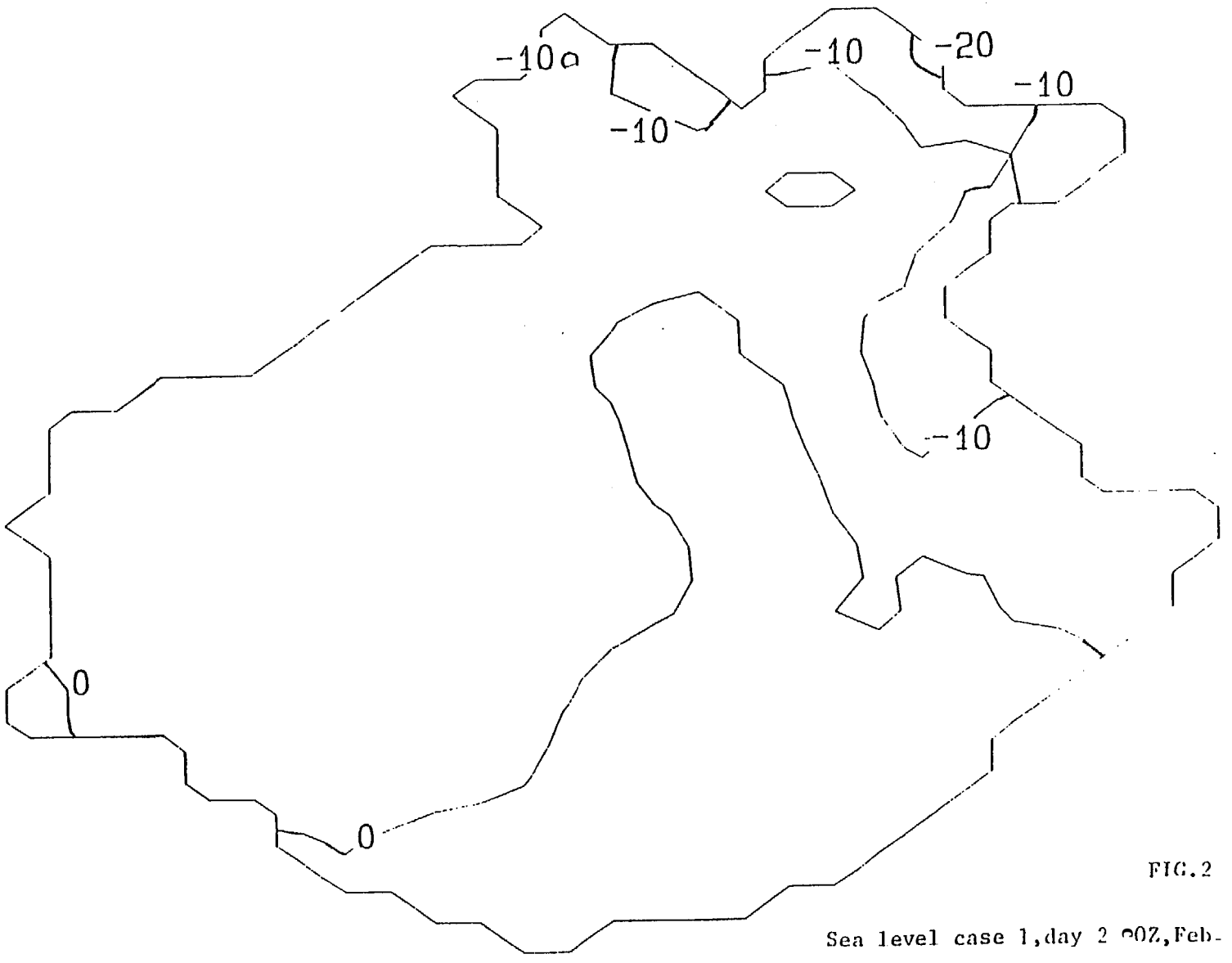

FIG. 2

Sea level case 1, day 2 00Z, Feb. 4, 982)
Numbers are given in cm.

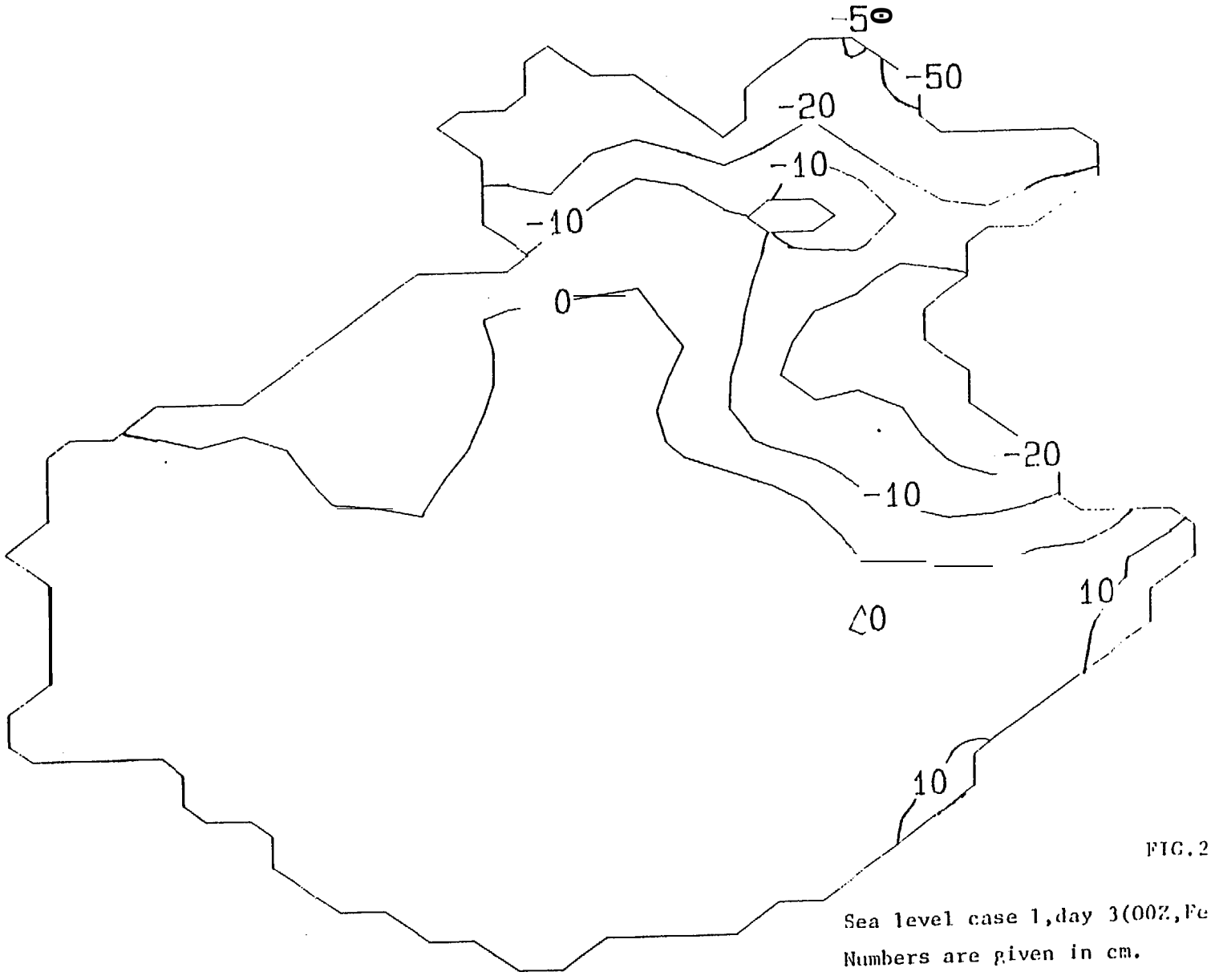

FIG. 22

Sea level case 1, day 3(00Z, Feb. 5, 982)
Numbers are given in cm.

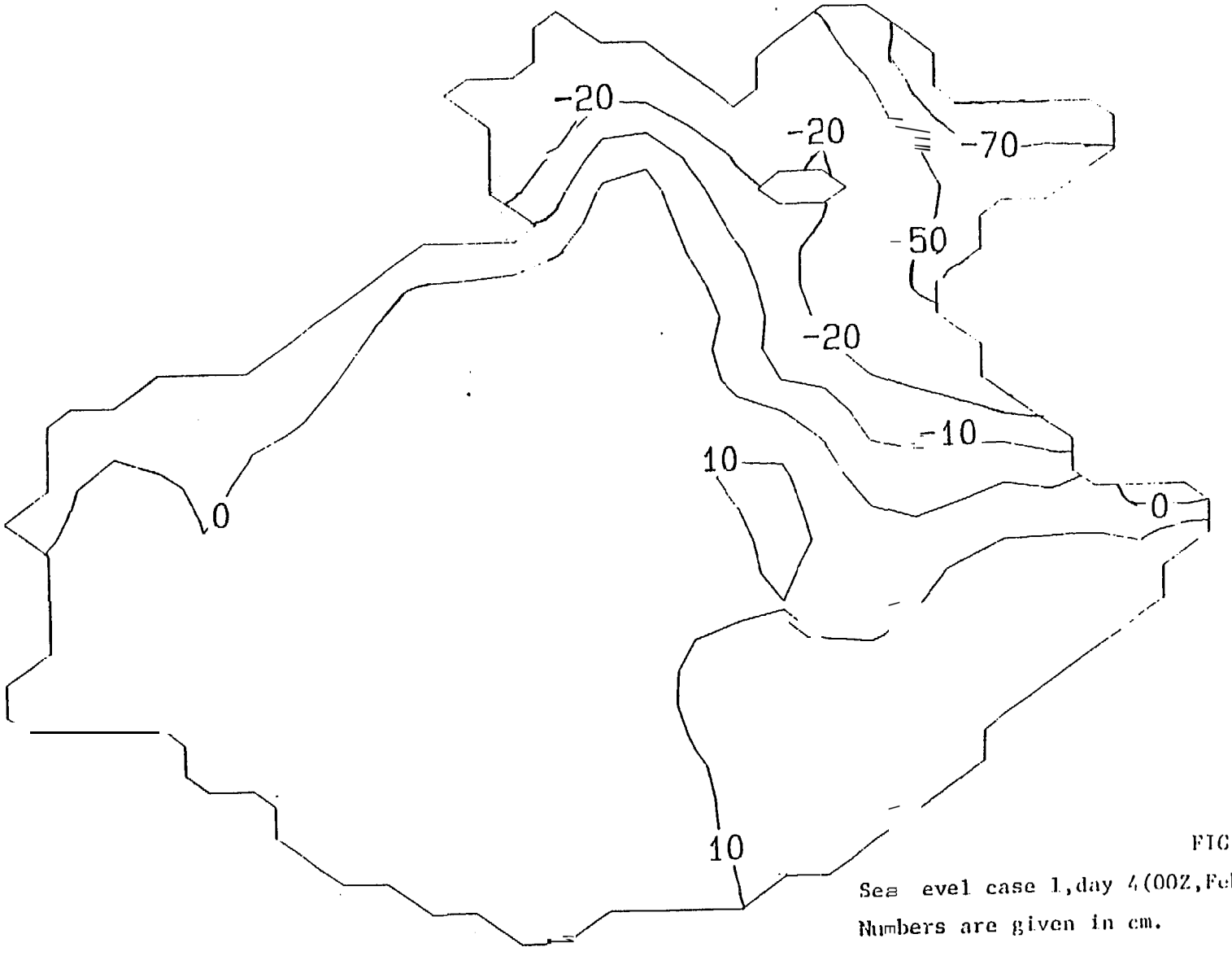

FIG. 23

Sea evel case 1, day 4 (00Z, Feb. 16, 982)

Numbers are given in cm.

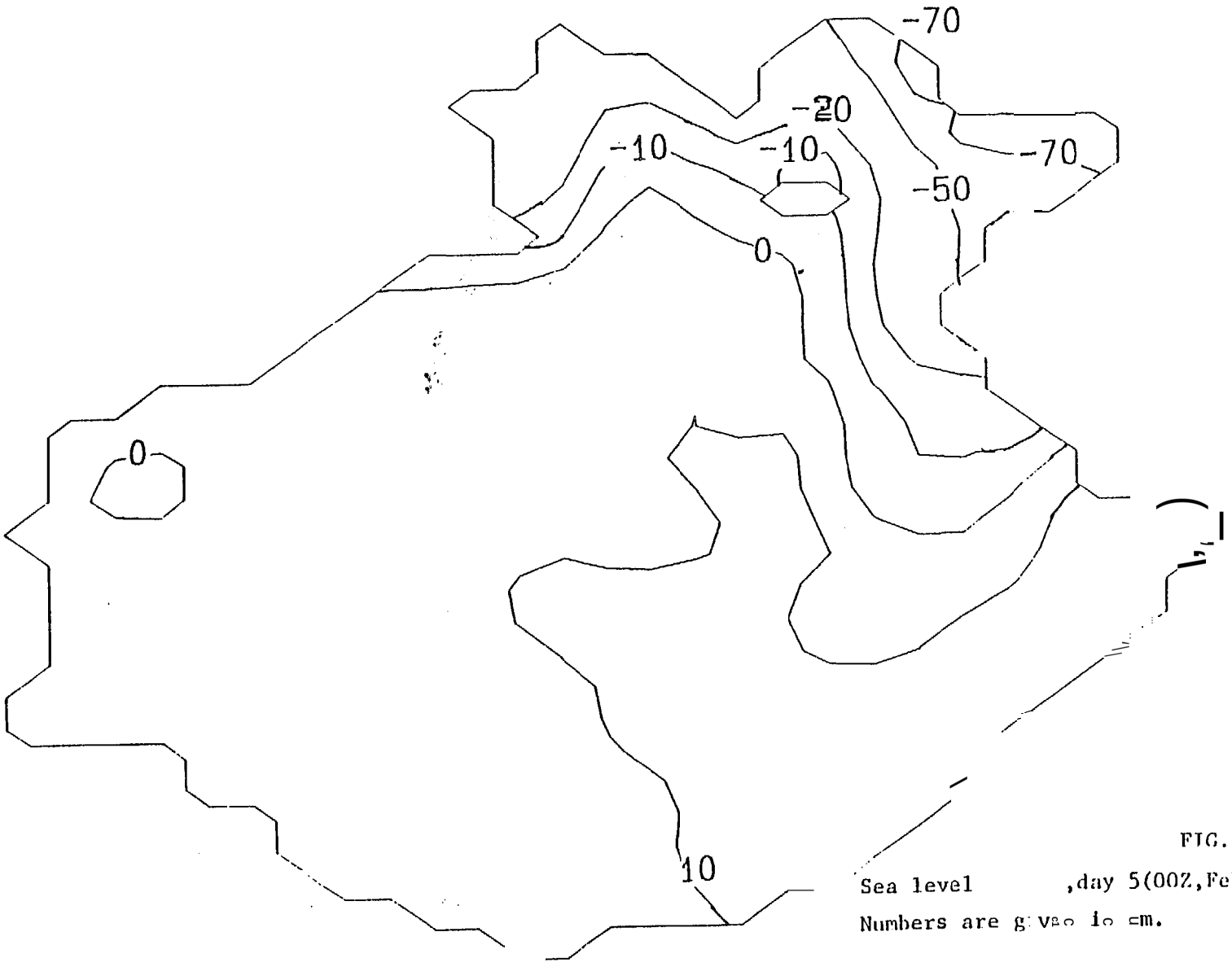

FIG. 24

Sea level ,day 5(00Z,Feb.17,1982)

Numbers are given in cm.

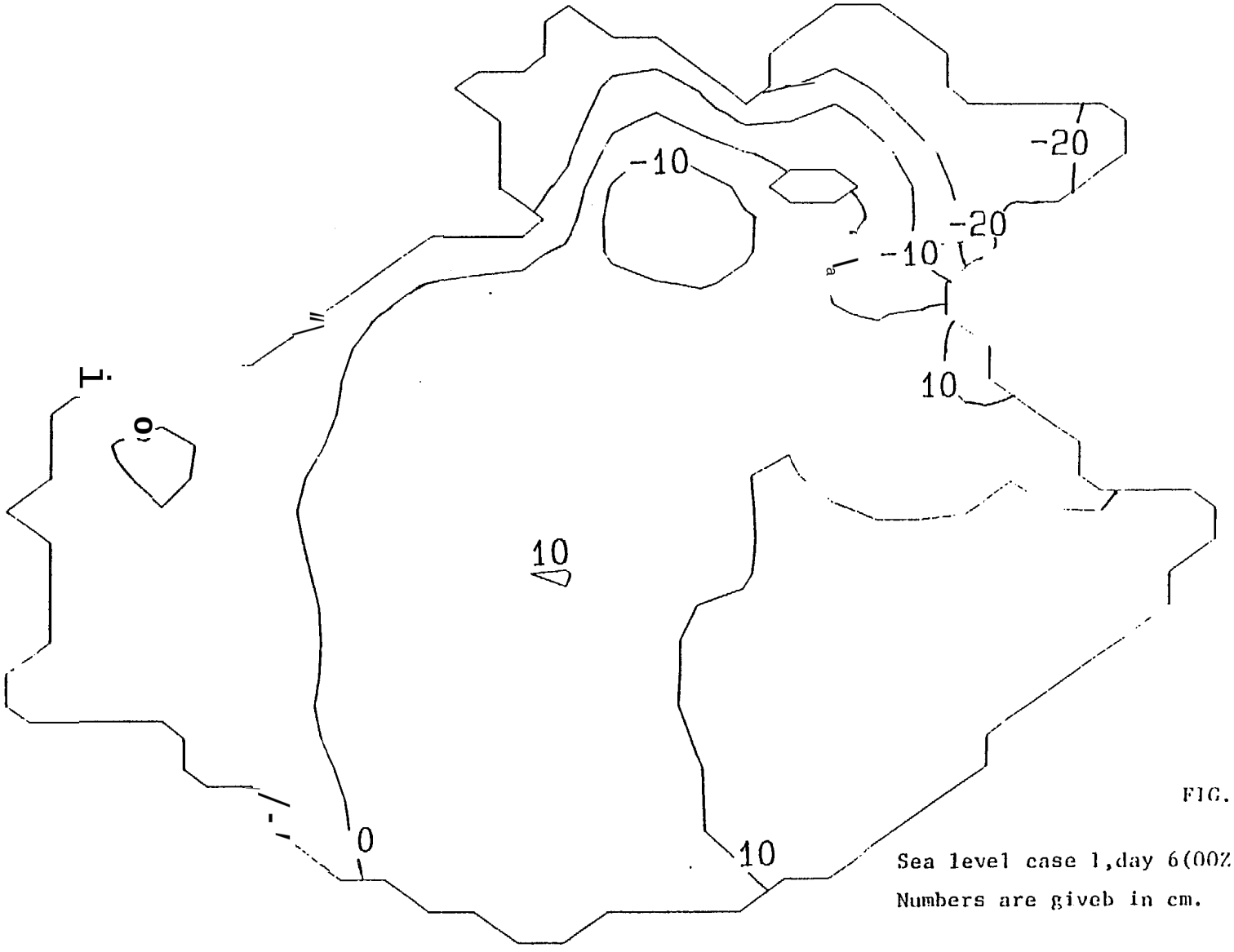

FIG.25

Sea level case 1,day 6(00Z,Feb. 8, 982)
Numbers are giveb in cm.

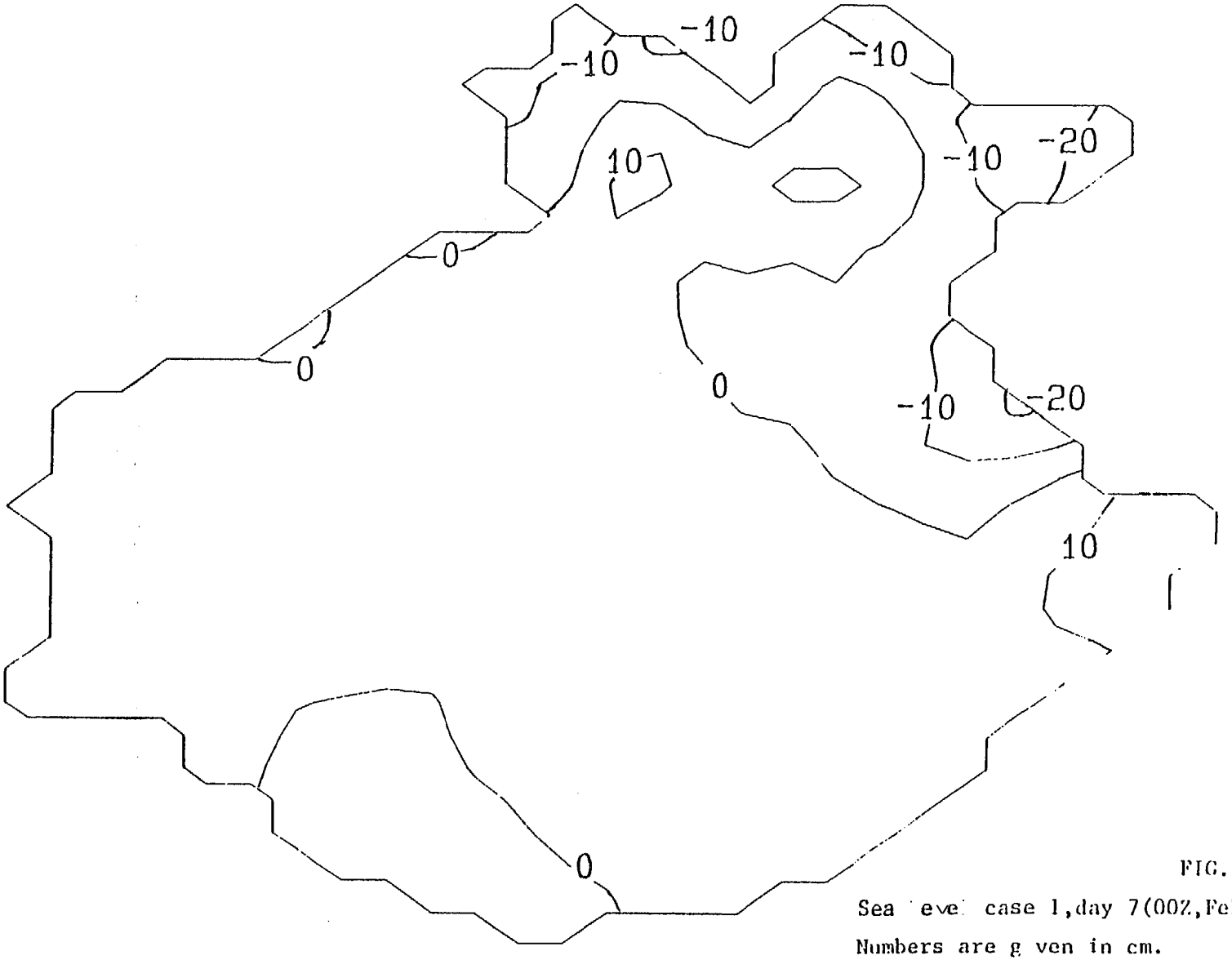

FIG.26

Sea level case 1, day 7 (00Z, Feb. 9, 982)

Numbers are given in cm.

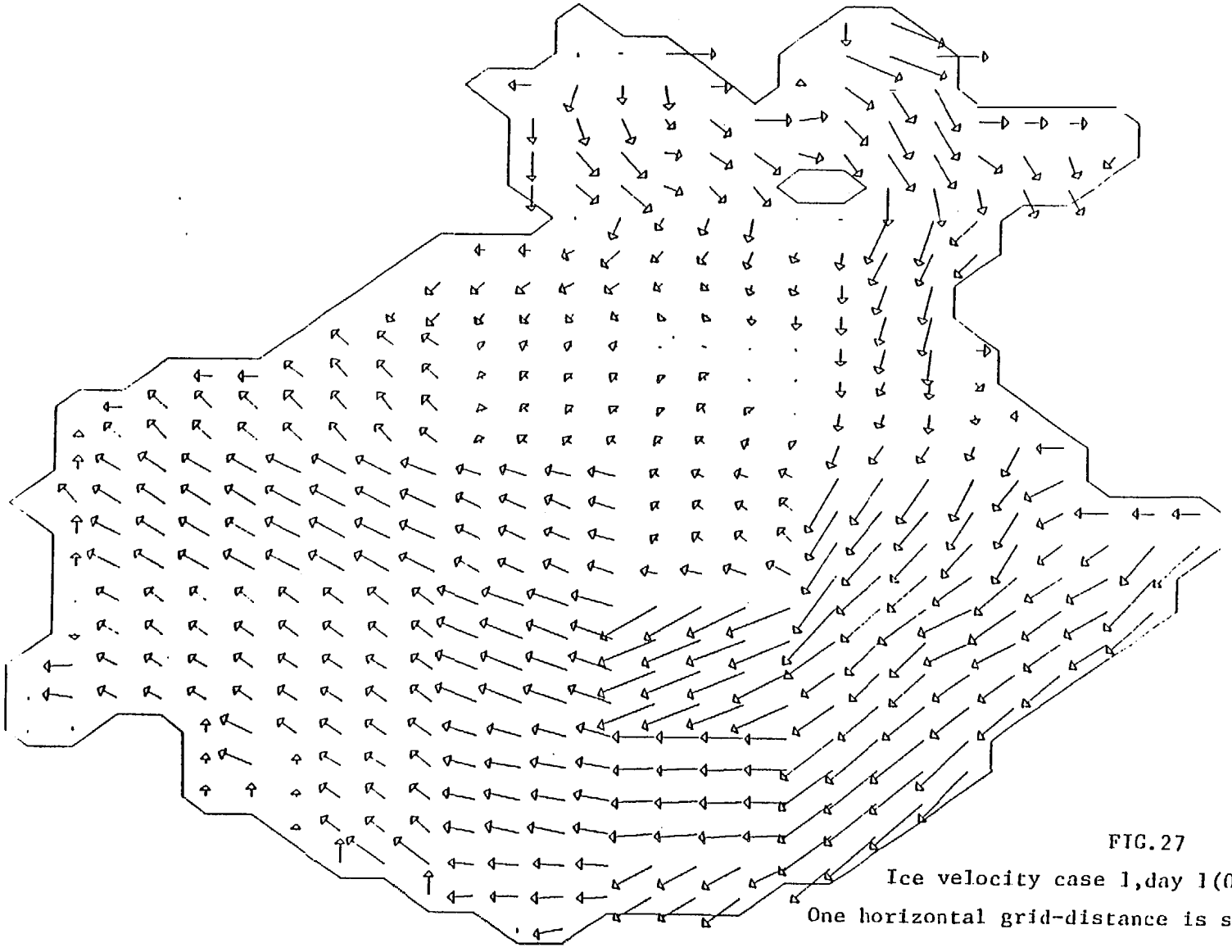

FIG. 27

Ice velocity case 1, day 1 (00Z, Feb. 13, 1982)

One horizontal grid-distance is scaled to 10cm/s.

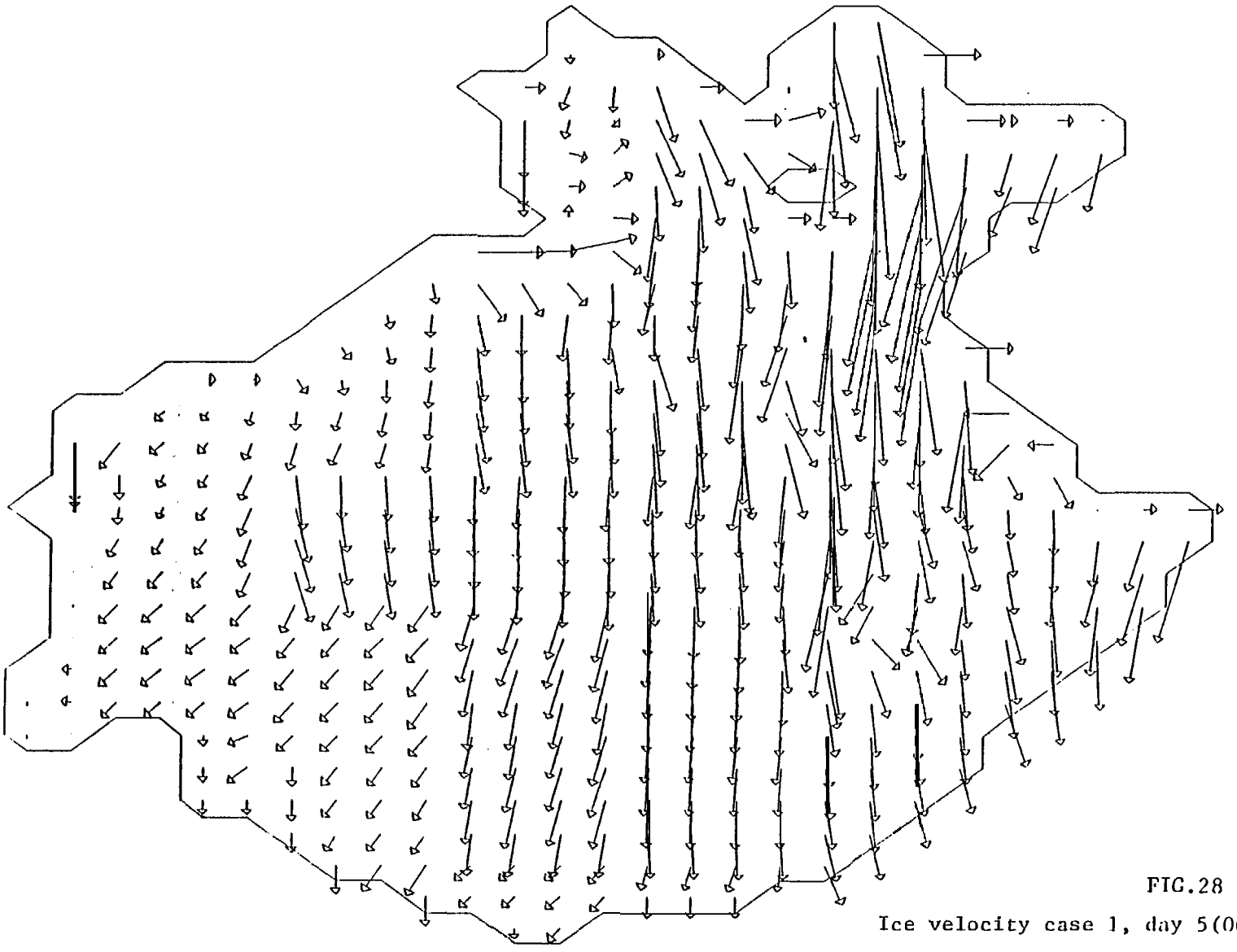

FIG.28

Ice velocity case 1, day 5(00Z,Feb. 7,1982)

One horizontal grid-distance is scaled to 0cm/s

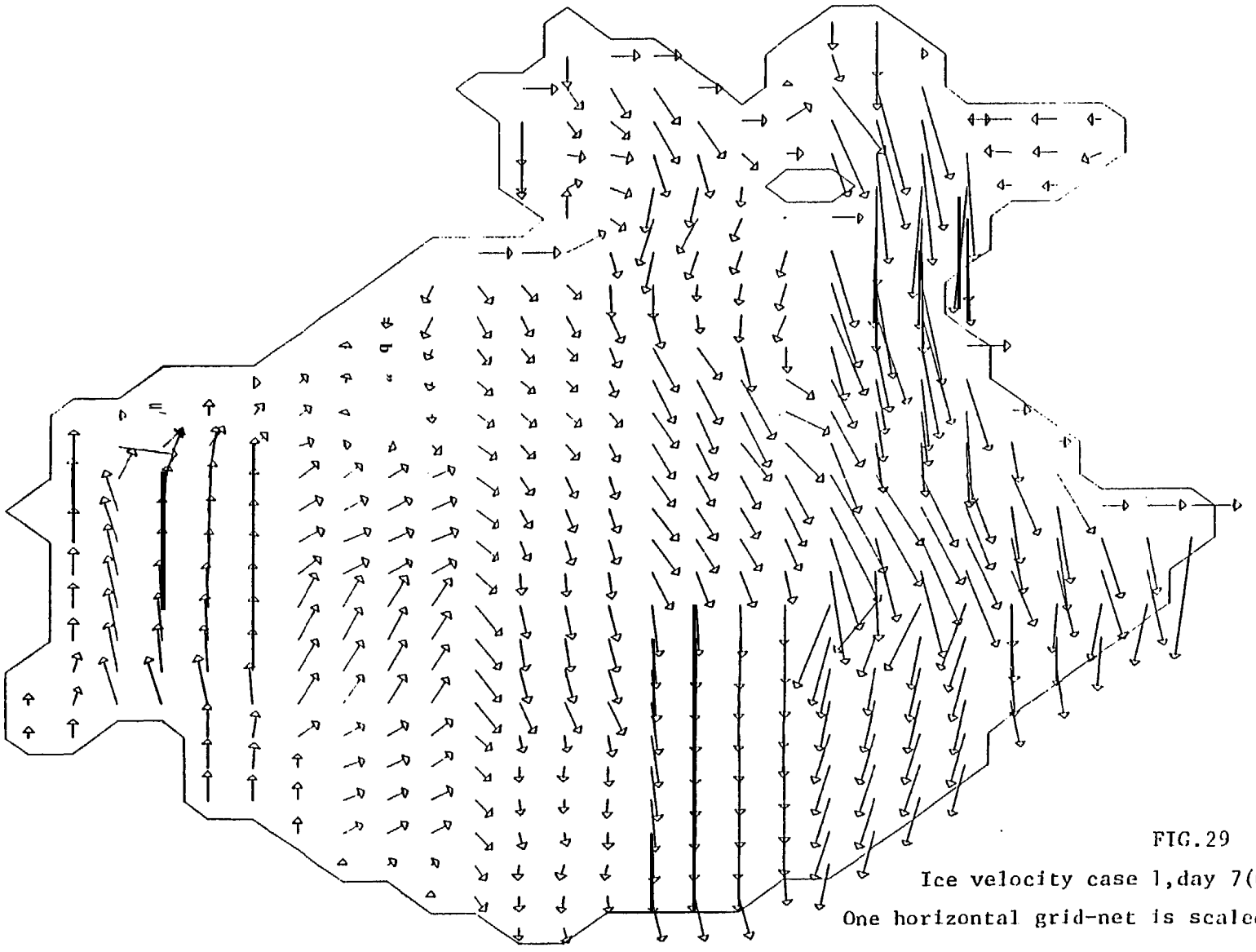

FIG.29

Ice velocity case 1,day 7(00Z,Feb.19,1982)

One horizontal grid-net is scaled to 10cm/s.

'CE VELOCITY 168 HOURS

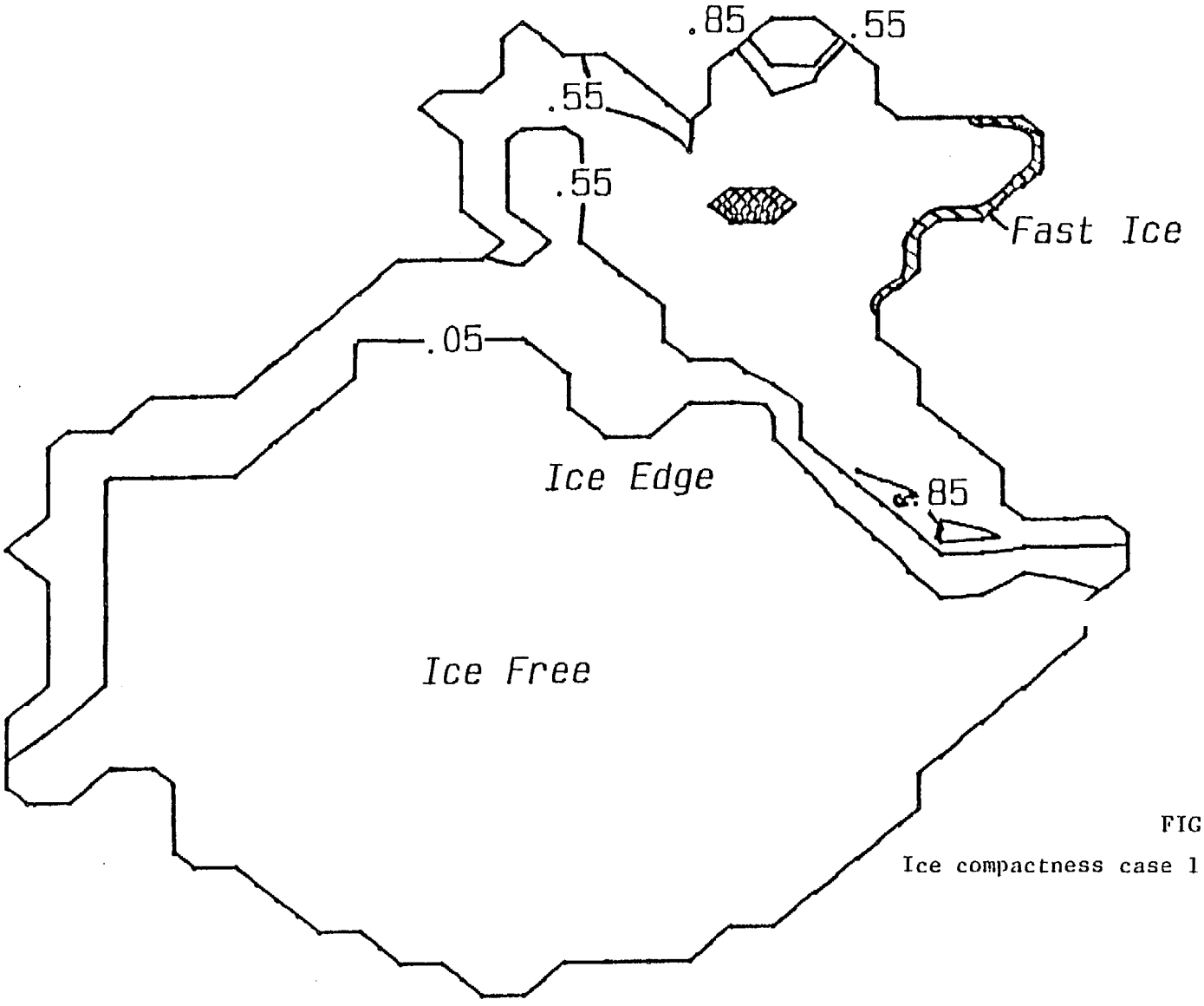

FIG.3c

Ice compactness case 1,day 1(00Z,Feb. 3, 982)

FIG. 31

Ice compactness case 1 ,day 5(00Z, Feb. 17,1982)

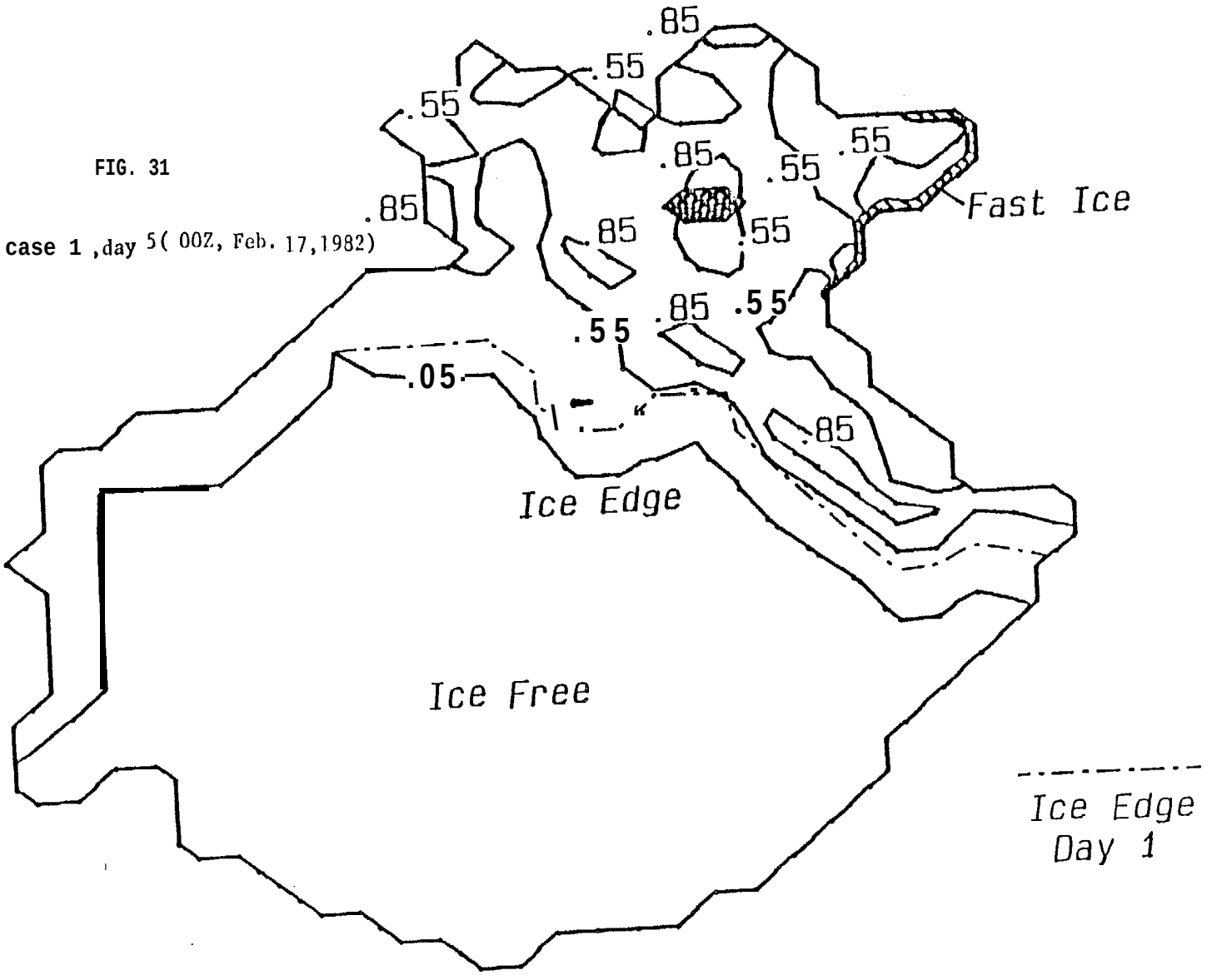

Ice Compactness Day 5

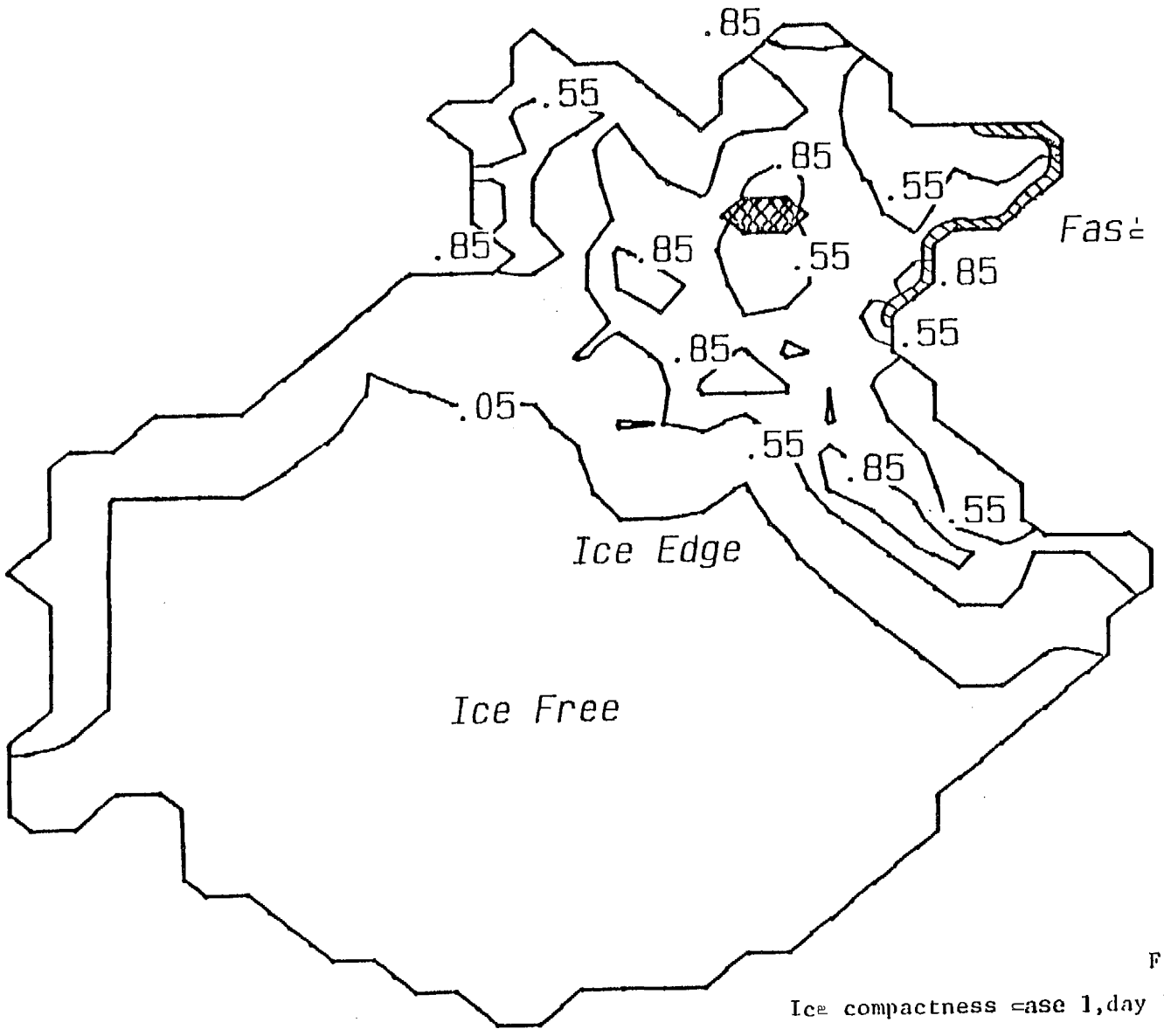

FIG.32

Ice compactness =ase 1,day 7(00Z,Feb. 9, 982)

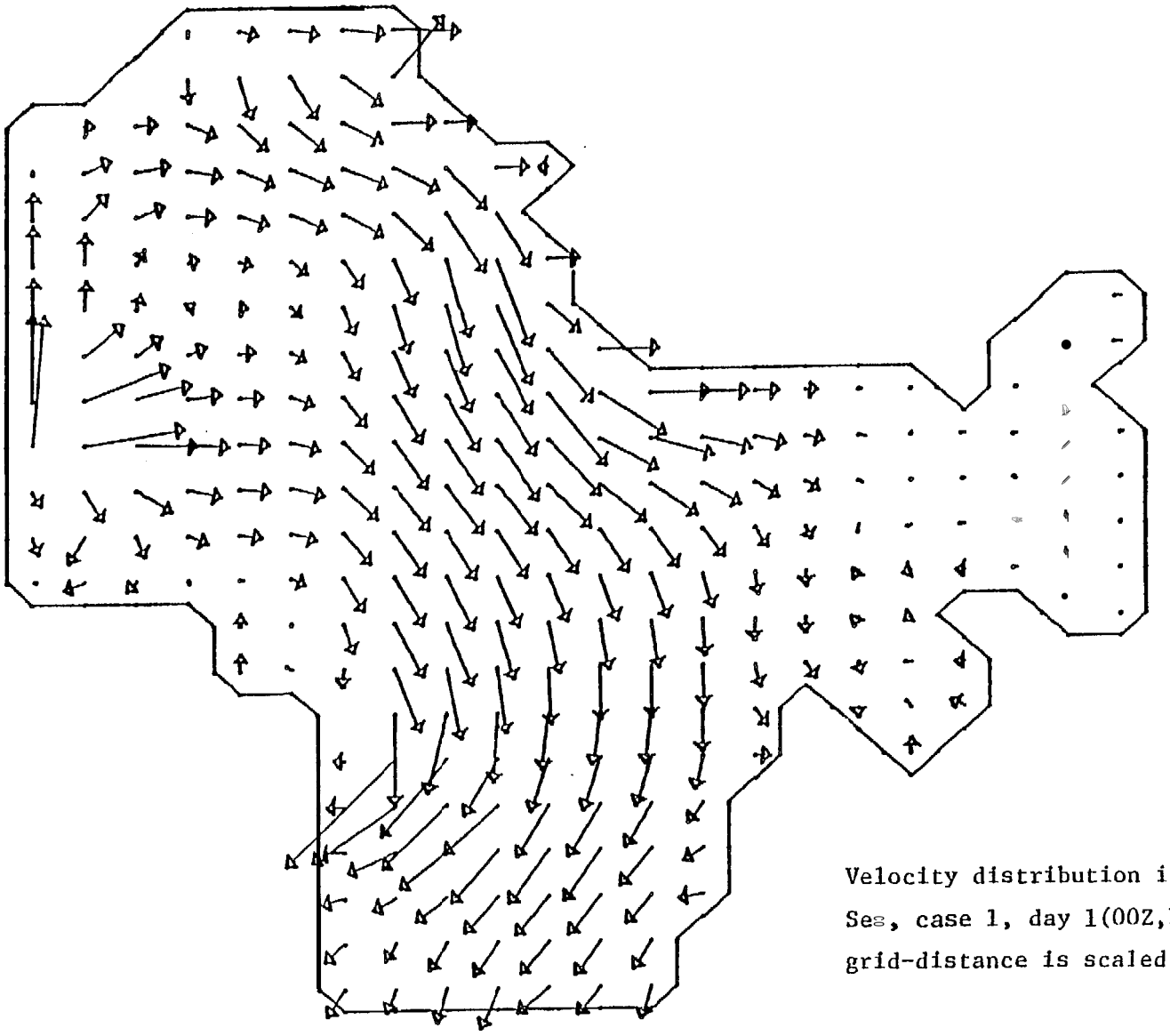

FIG.33

Velocity distribution in the northeastern Bering Sea, case 1, day 1(00Z,Feb.13,1982). One horizontal grid-distance is scaled to 10cm/s.

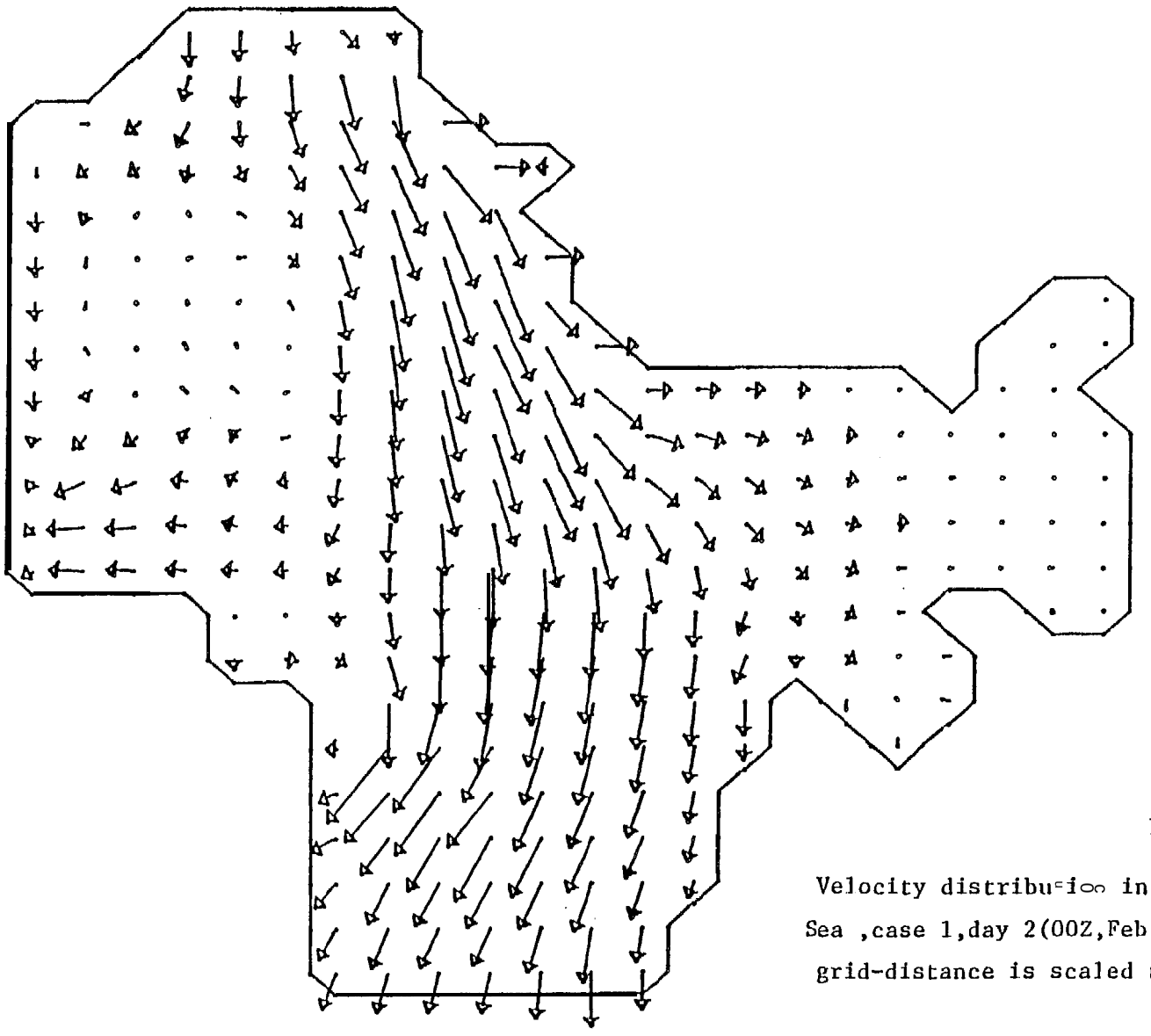

FIG. 34

Velocity distribution in the northeastern Bering Sea ,case 1,day 2(00Z,Feb.14,1982).One horizontal grid-distance is scaled to 10cm/s.

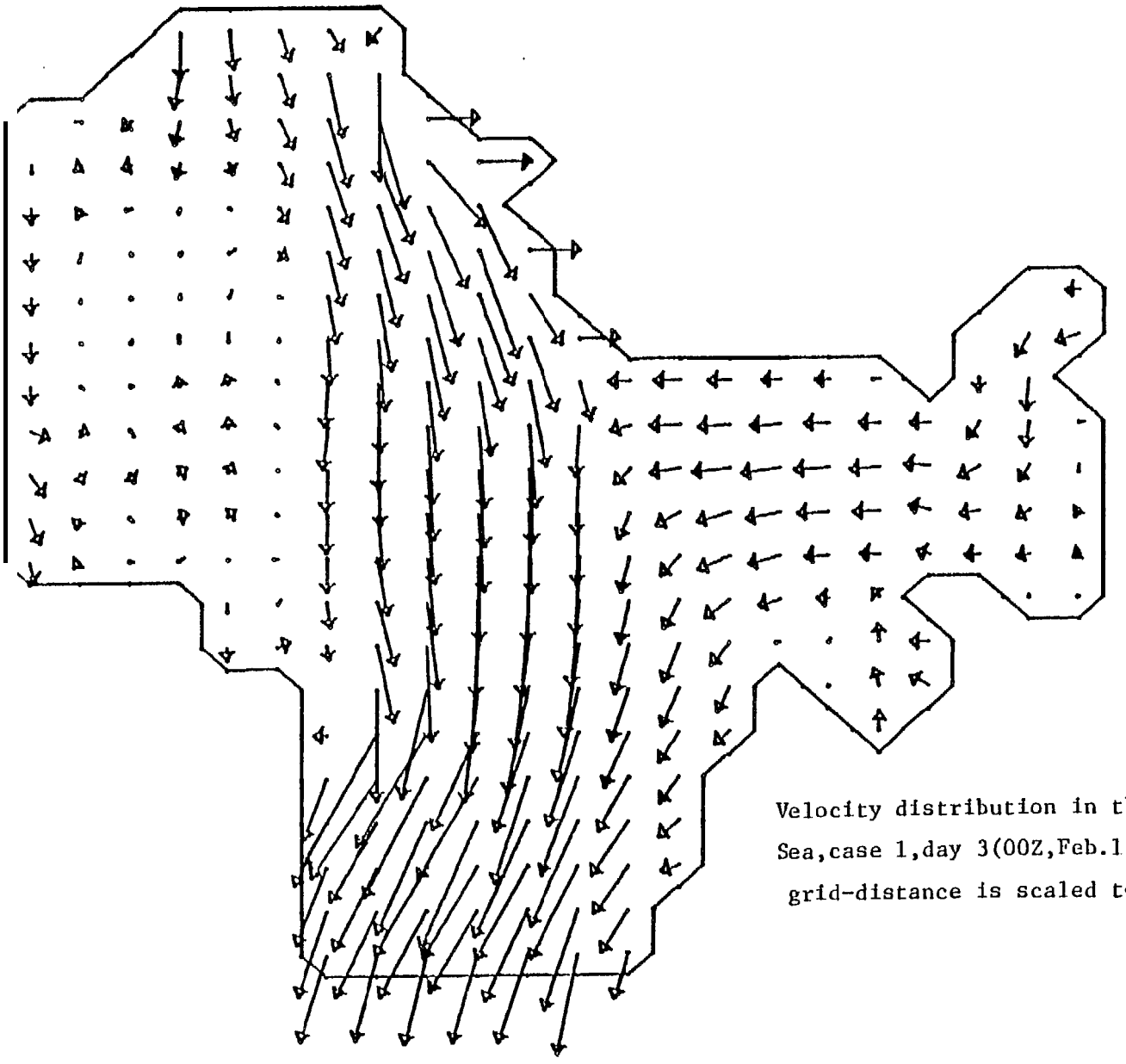

FIG.35

Velocity distribution in the northeastern Bering Sea, case 1, day 3(00Z, Feb.15, 1982). One horizontal grid-distance is scaled to 20cm/s.

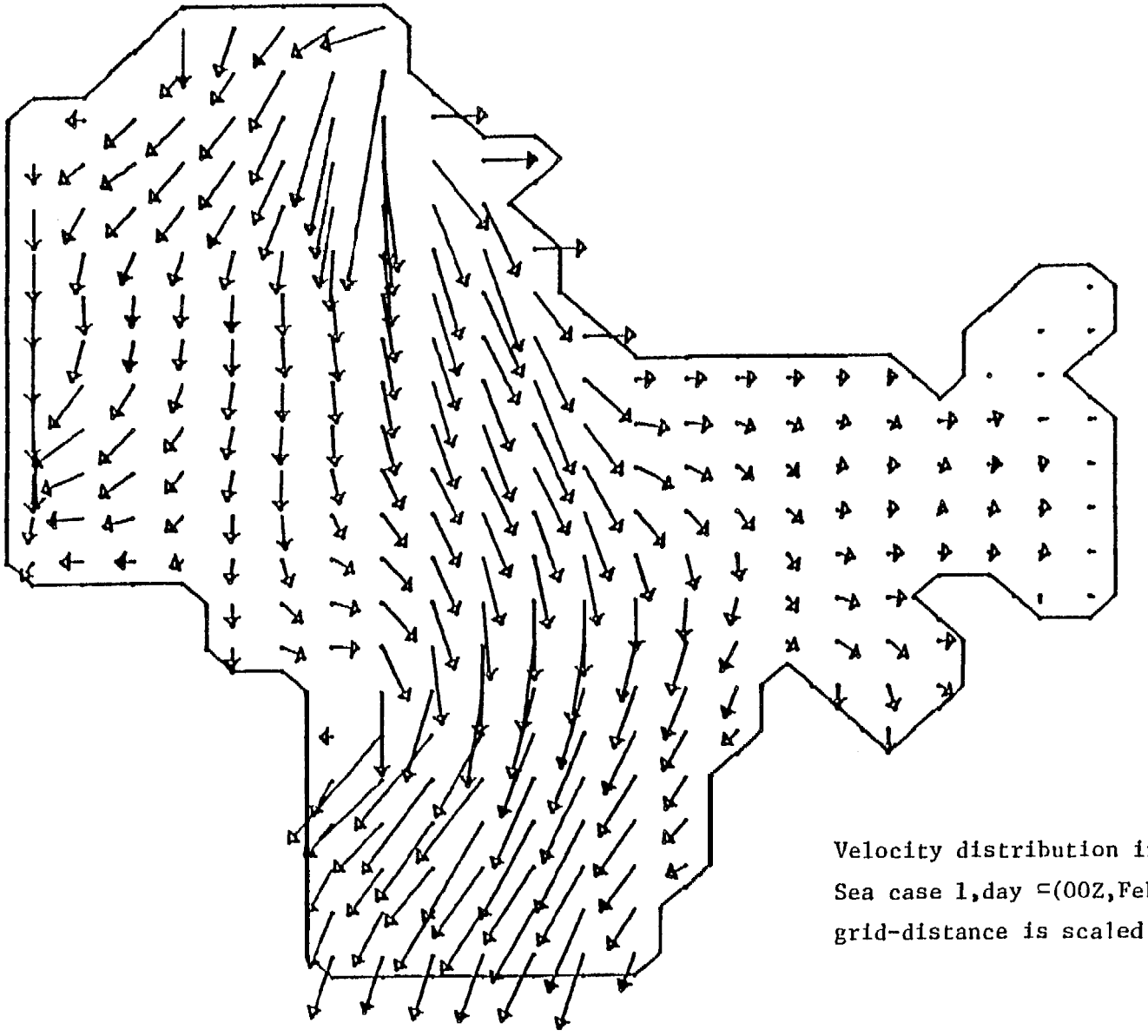

FIG. 36

Velocity distribution in the northeastern Bering Sea case 1, day 4 (00Z, Feb. 16, 1982). One horizontal grid-distance is scaled to 20cm/s.

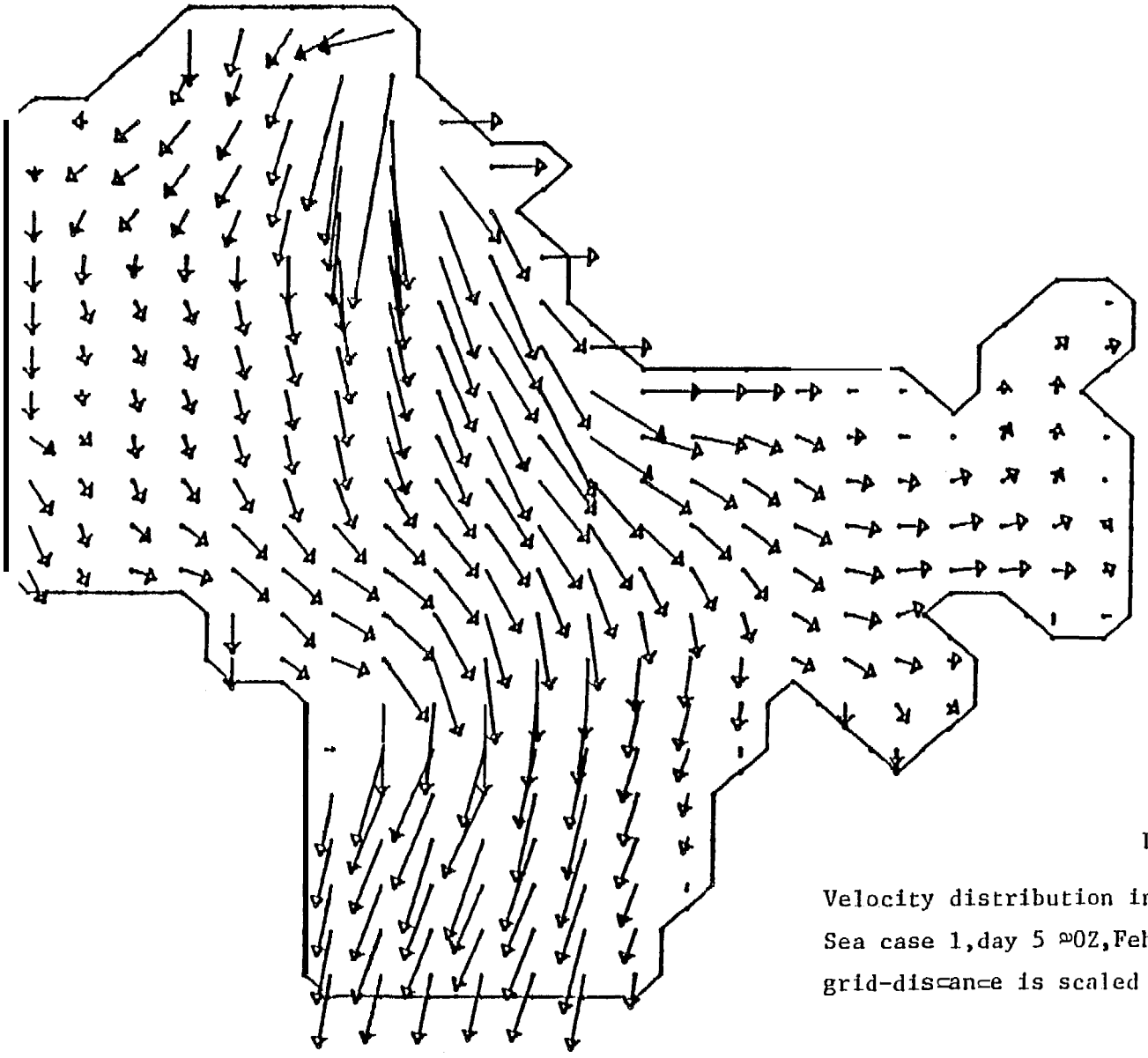

FIG.37

Velocity distribution in the northeastern Bering Sea case 1,day 5 (0Z,Feb.17 1982).One horizontal grid-distance is scaled to 20 cm/s.

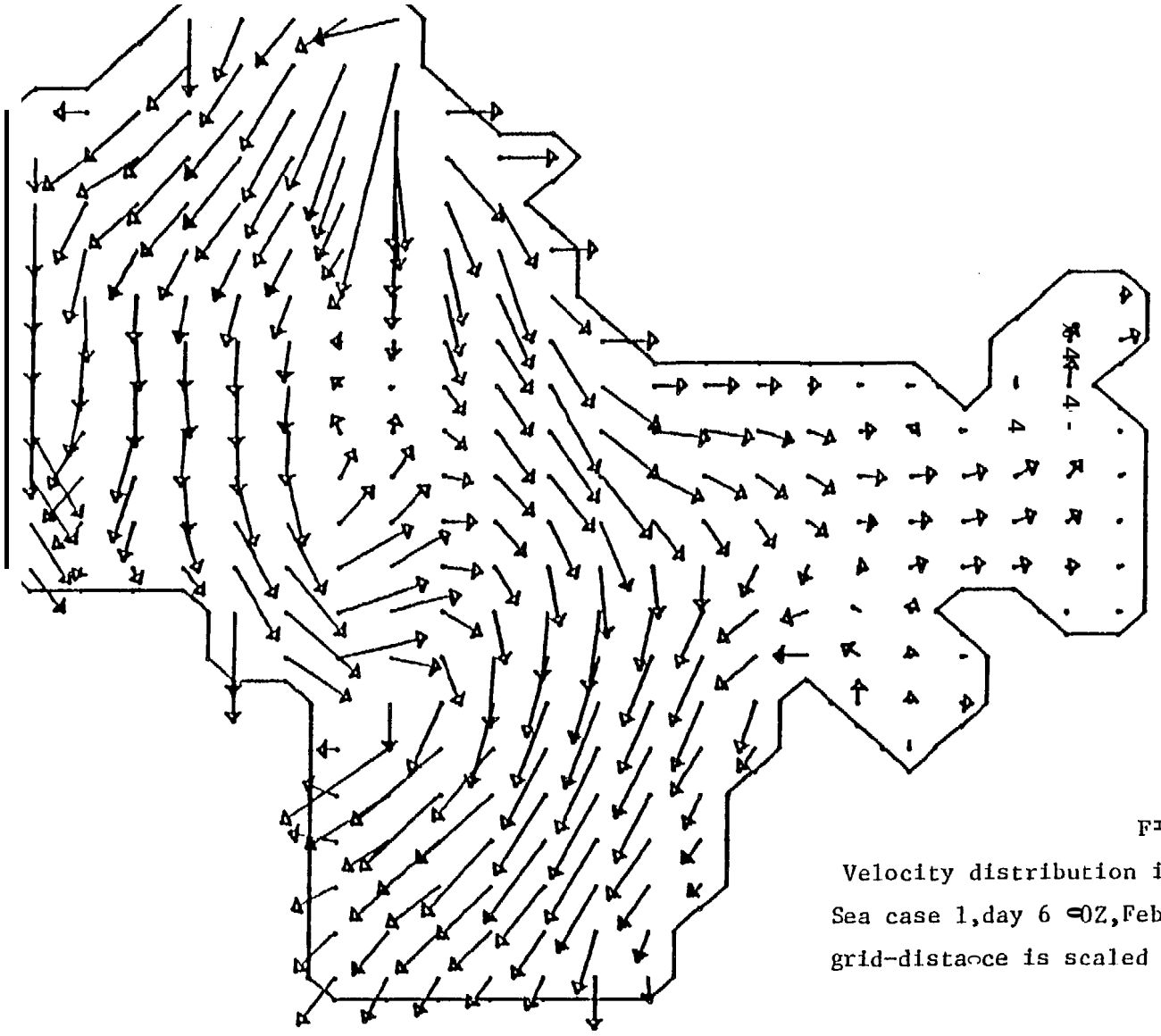

FIG. 38

Velocity distribution in the northeastern Bering Sea case 1, day 6 (0Z, Feb. 18, 1982) One horizontal grid-distance is scaled to 10 cm/s.

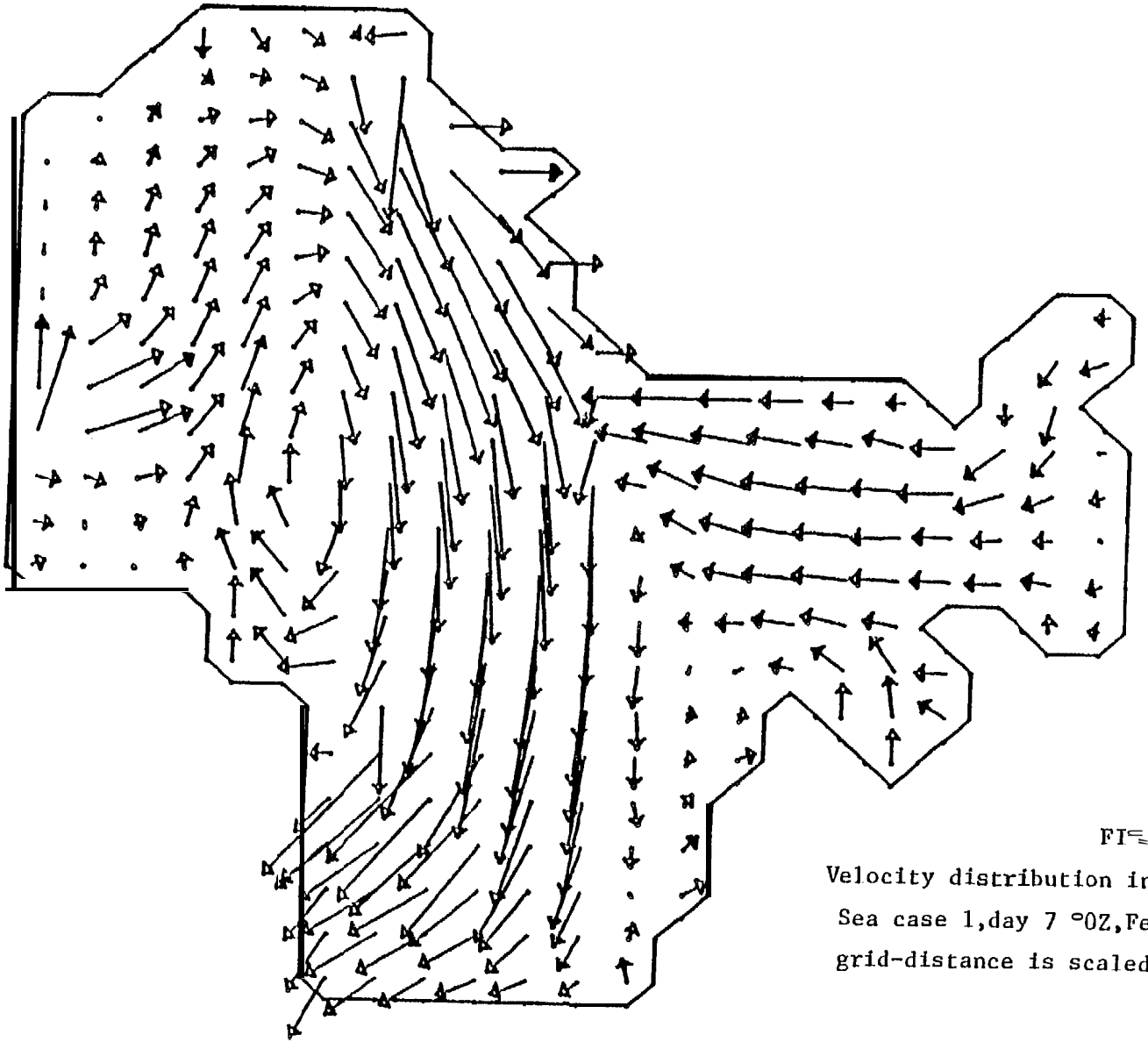

FI⩽ 39

Velocity distribution in the northeastern Bering Sea case 1,day 7 °0Z,Feb.19, 982) One horizonta grid-distance is scaled ⩽⊖ ∩ ⊏m/s.

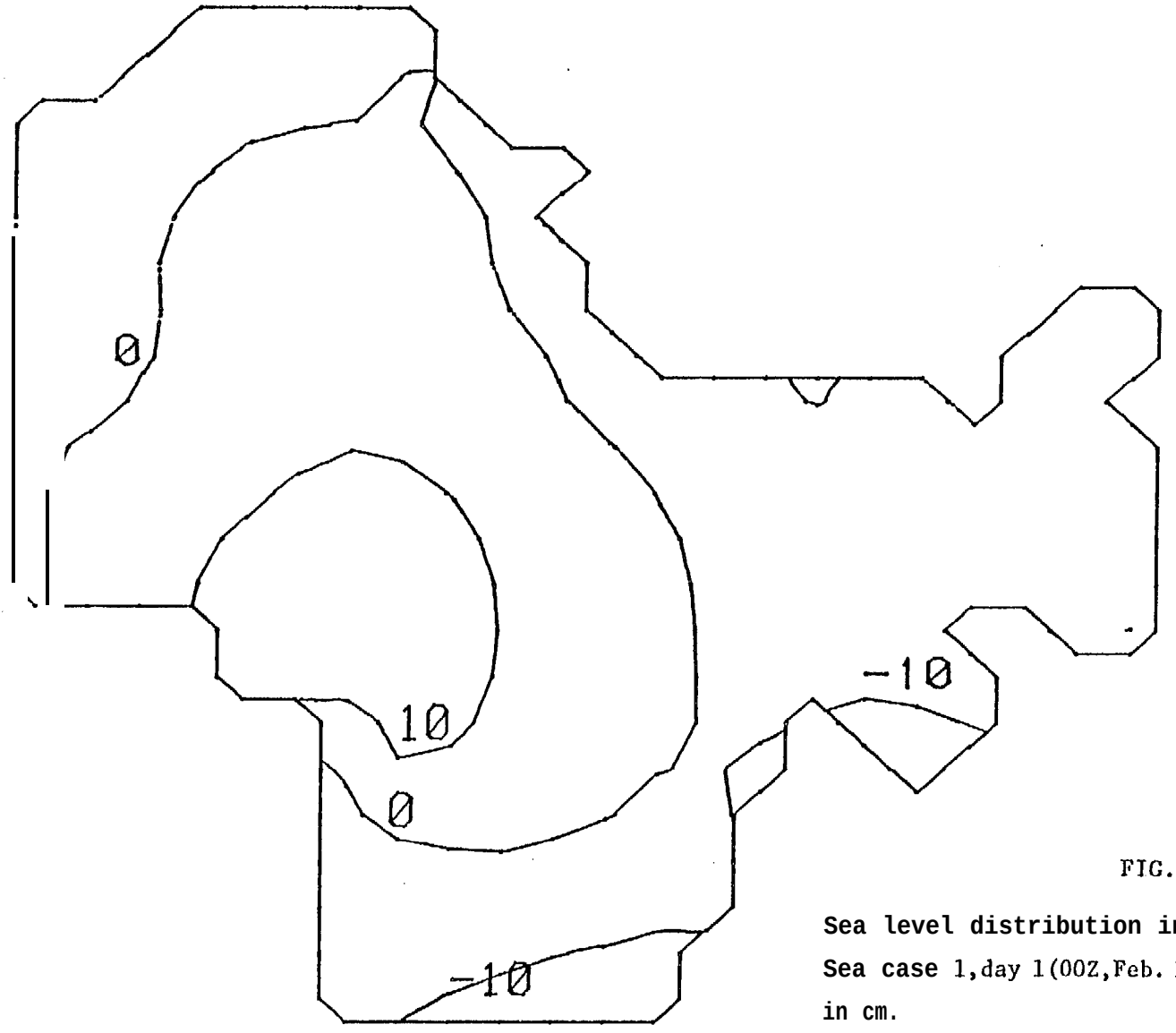

FIG.40

Sea level distribution in the northeastern Bering Sea case 1, day 1 (00Z, Feb. 13, 1982). Numbers are given in cm.

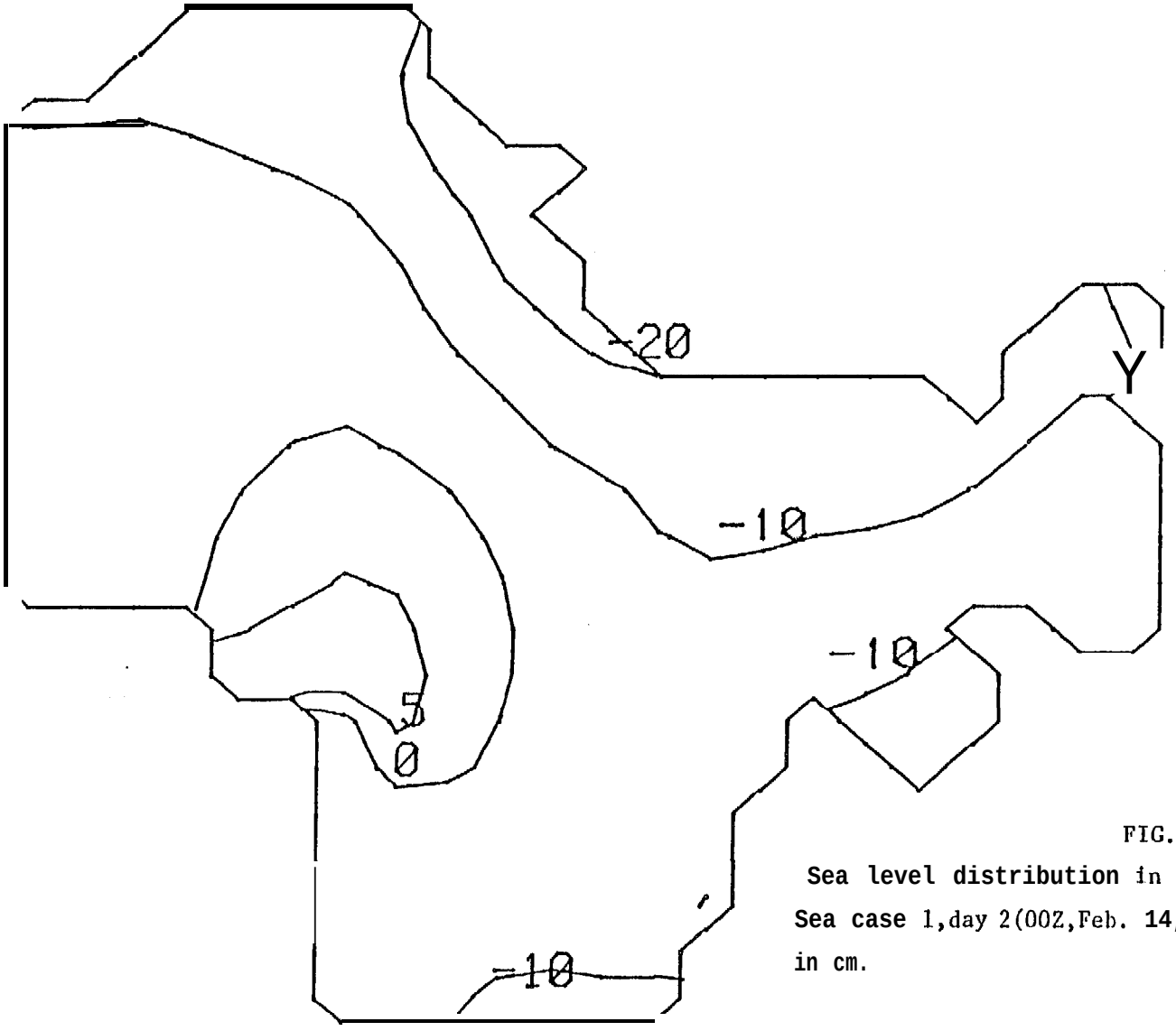

FIG.41

Sea level distribution in the northeastern Bering Sea case 1, day 2 (00Z, Feb. 14, 1982). Numbers are given in cm.

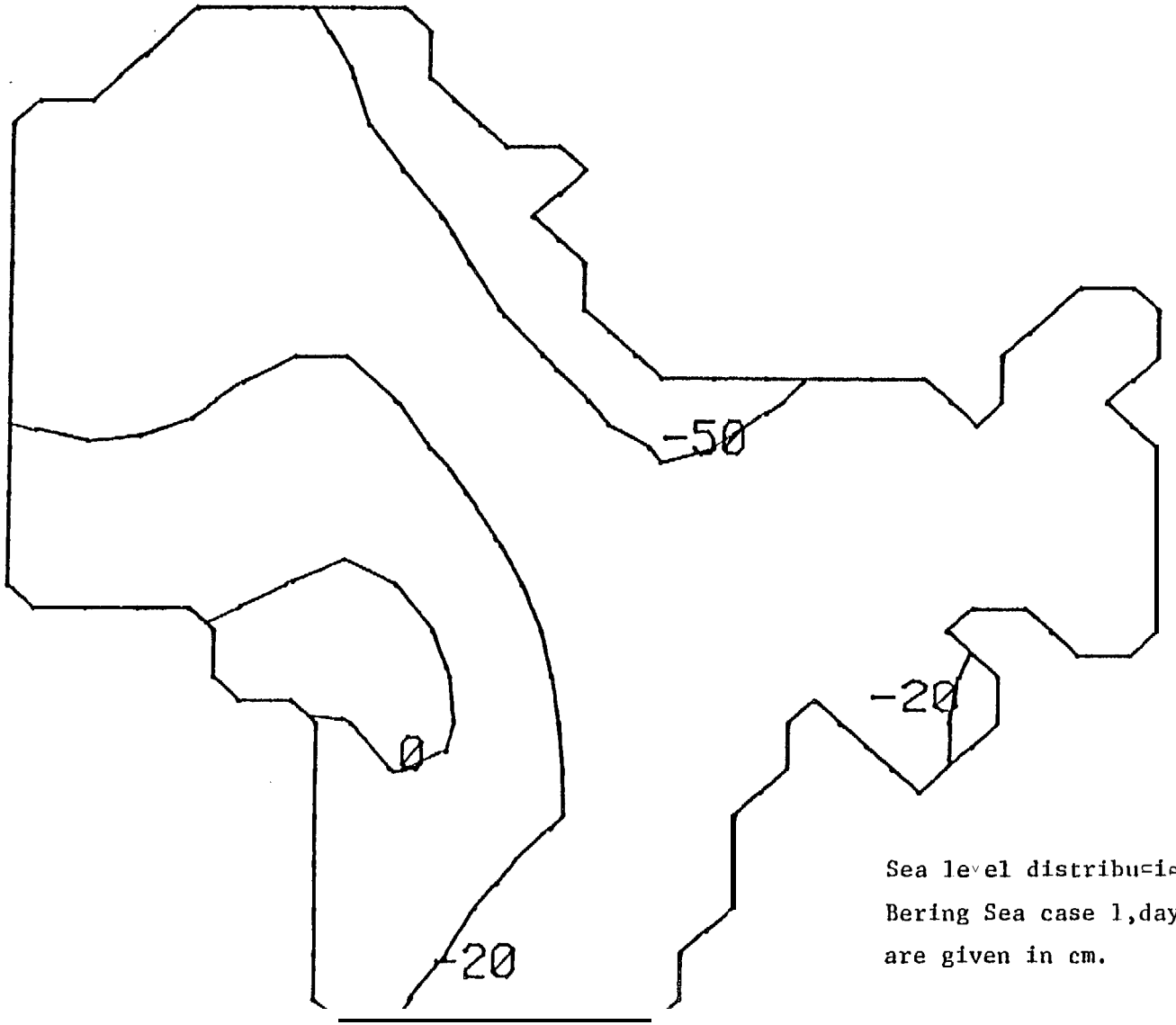

SEA LEVEL DAY 3.

FIG. 2

Sea level distribution in the northeastern Bering Sea case 1, day 3 (00Z, Feb. 15, 1982). Numbers are given in cm.

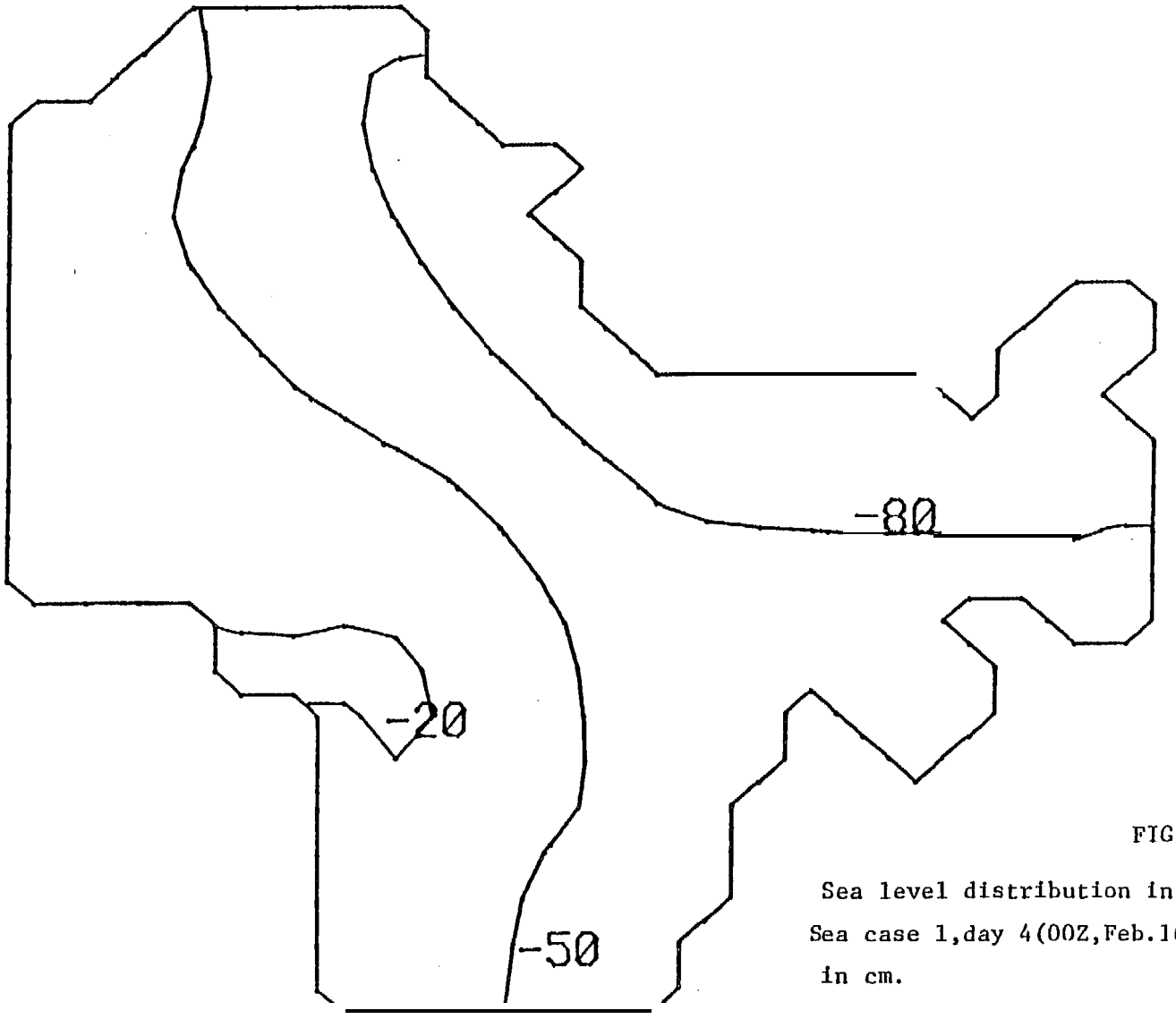

FIG.43

Sea level distribution in the northeastern Bering Sea case 1,day 4(00Z,Feb.16,1982) rs are given in cm.

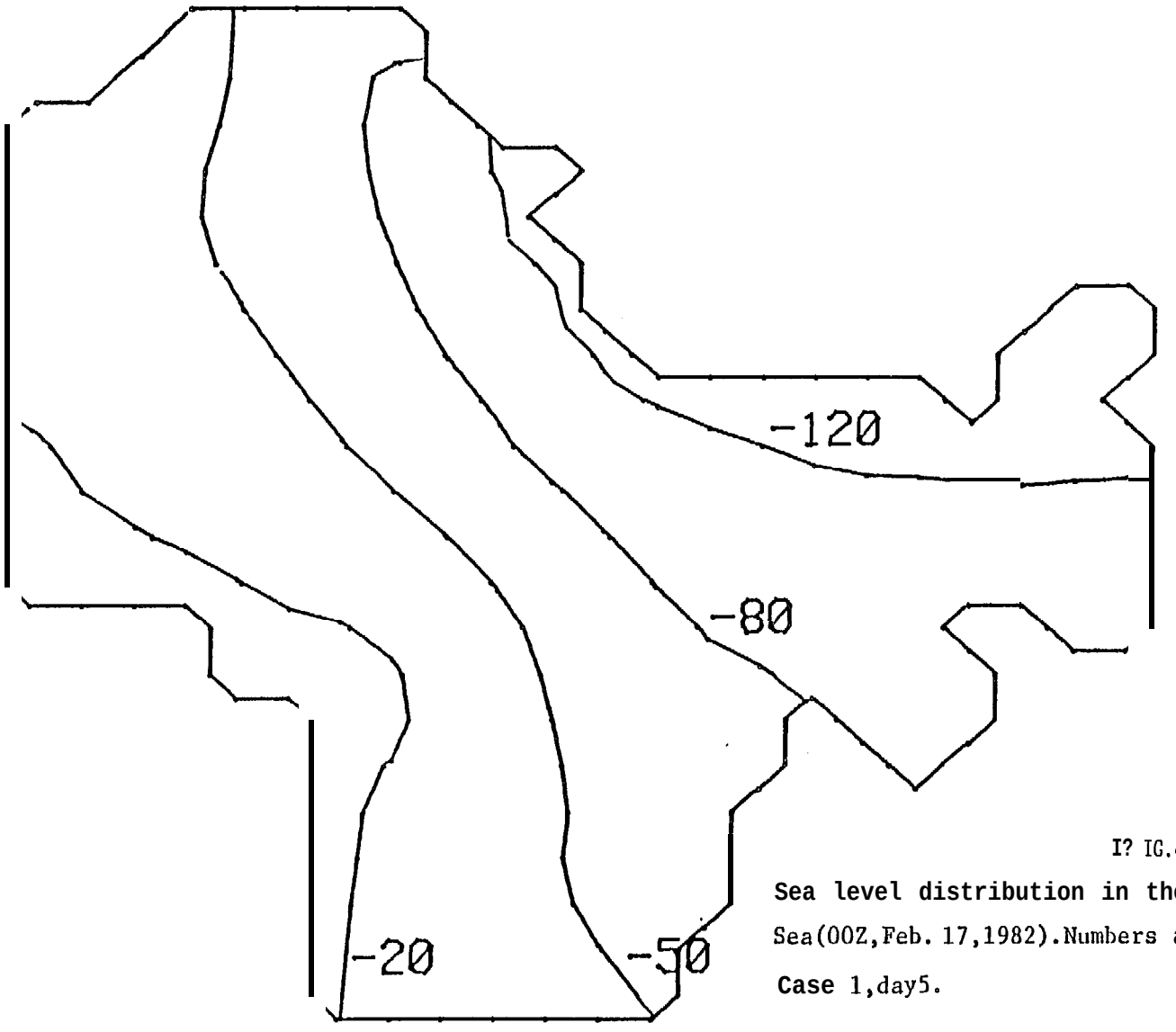

I? IG.44

Sea level distribution in the northeastern Bering Sea(00Z,Feb. 17,1982).Numbers are given in cm. Case 1,day5.

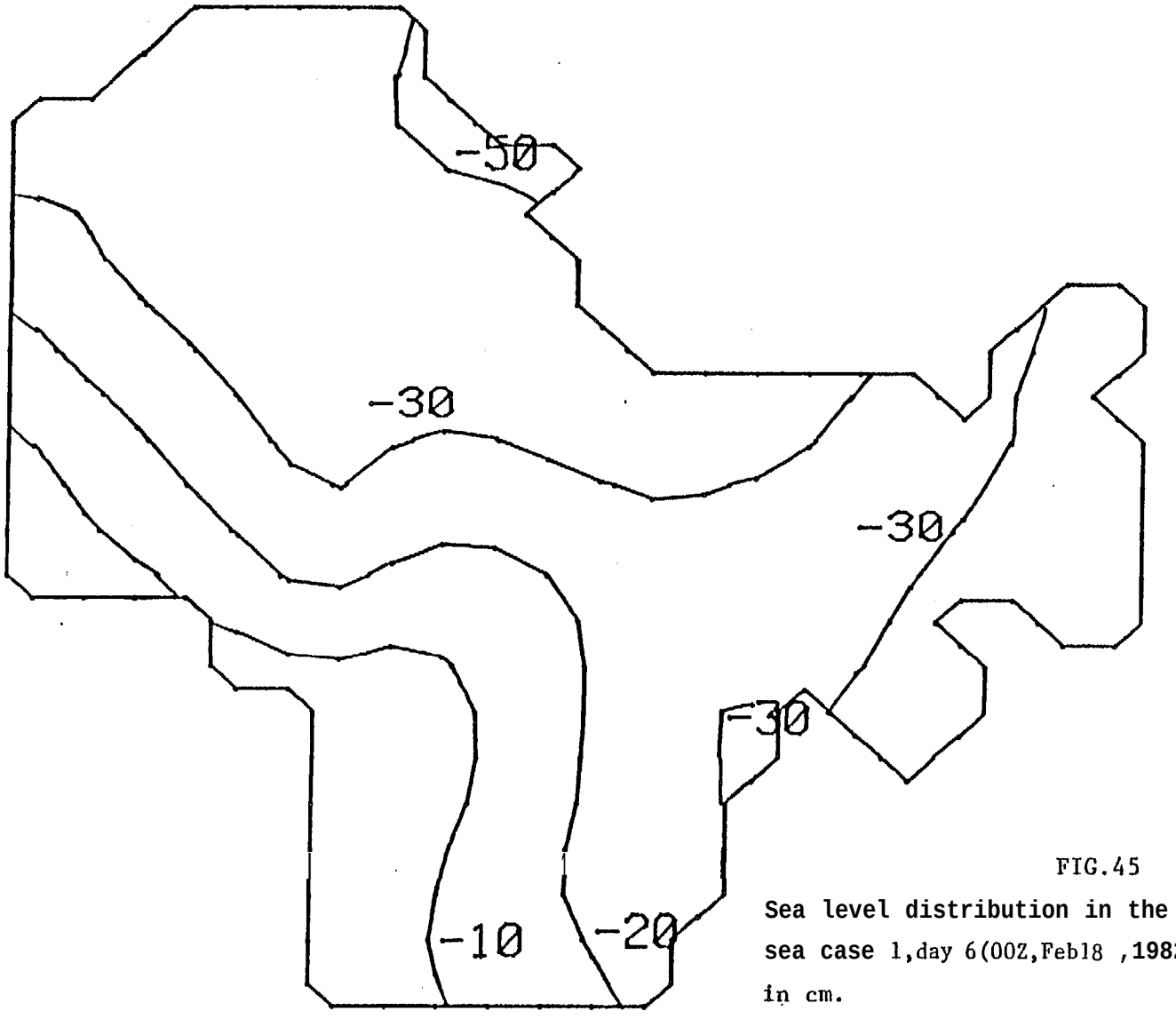

FIG.45

Sea level distribution in the northeastern Bering sea case 1,day 6(00Z,Feb18 ,1982). Numbers are given in cm.

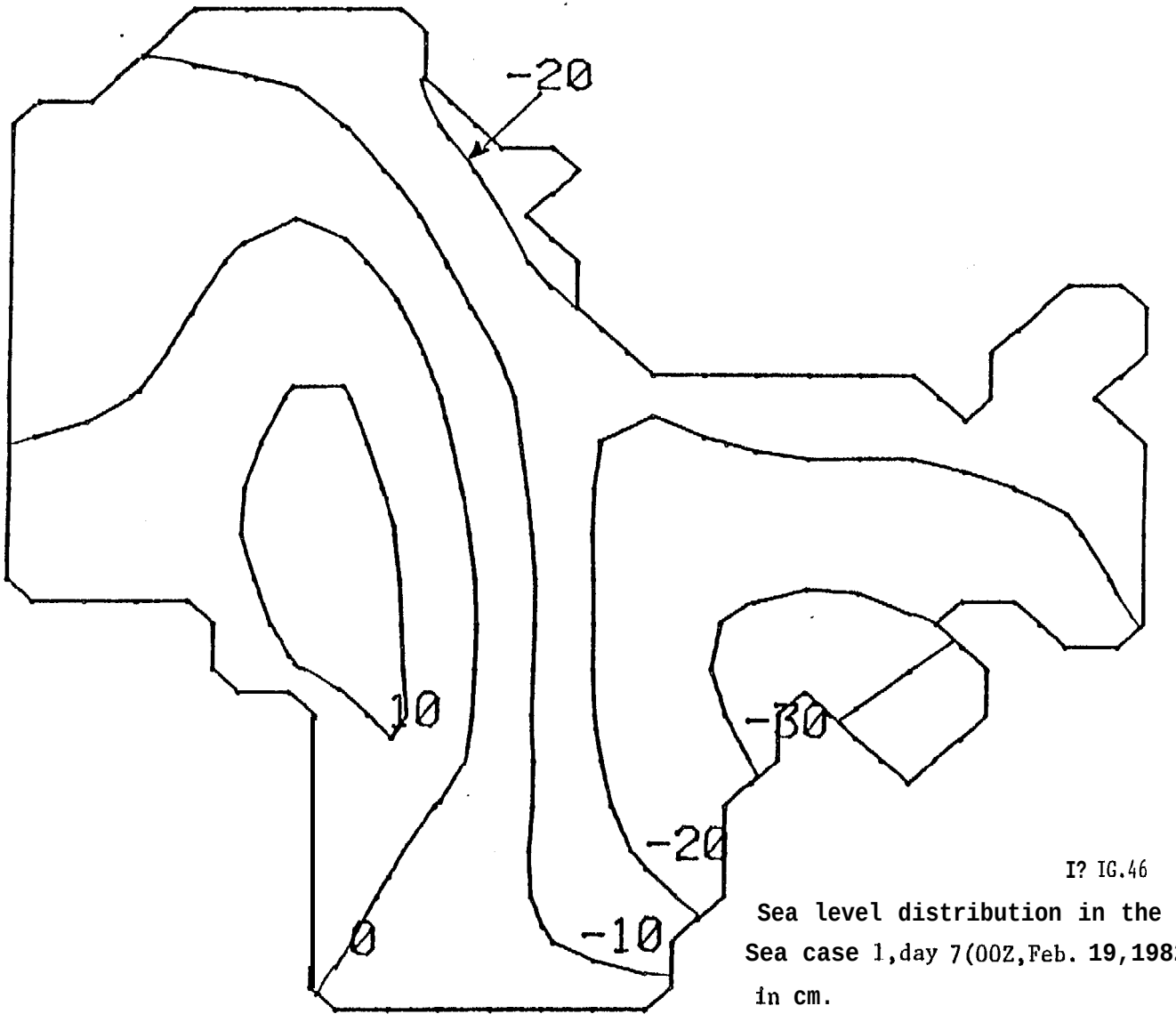

I? IG.46

Sea level distribution in the northeastern Bering Sea case 1,day 7(00Z,Feb. **19,1982).** Numbers **are given** in cm.

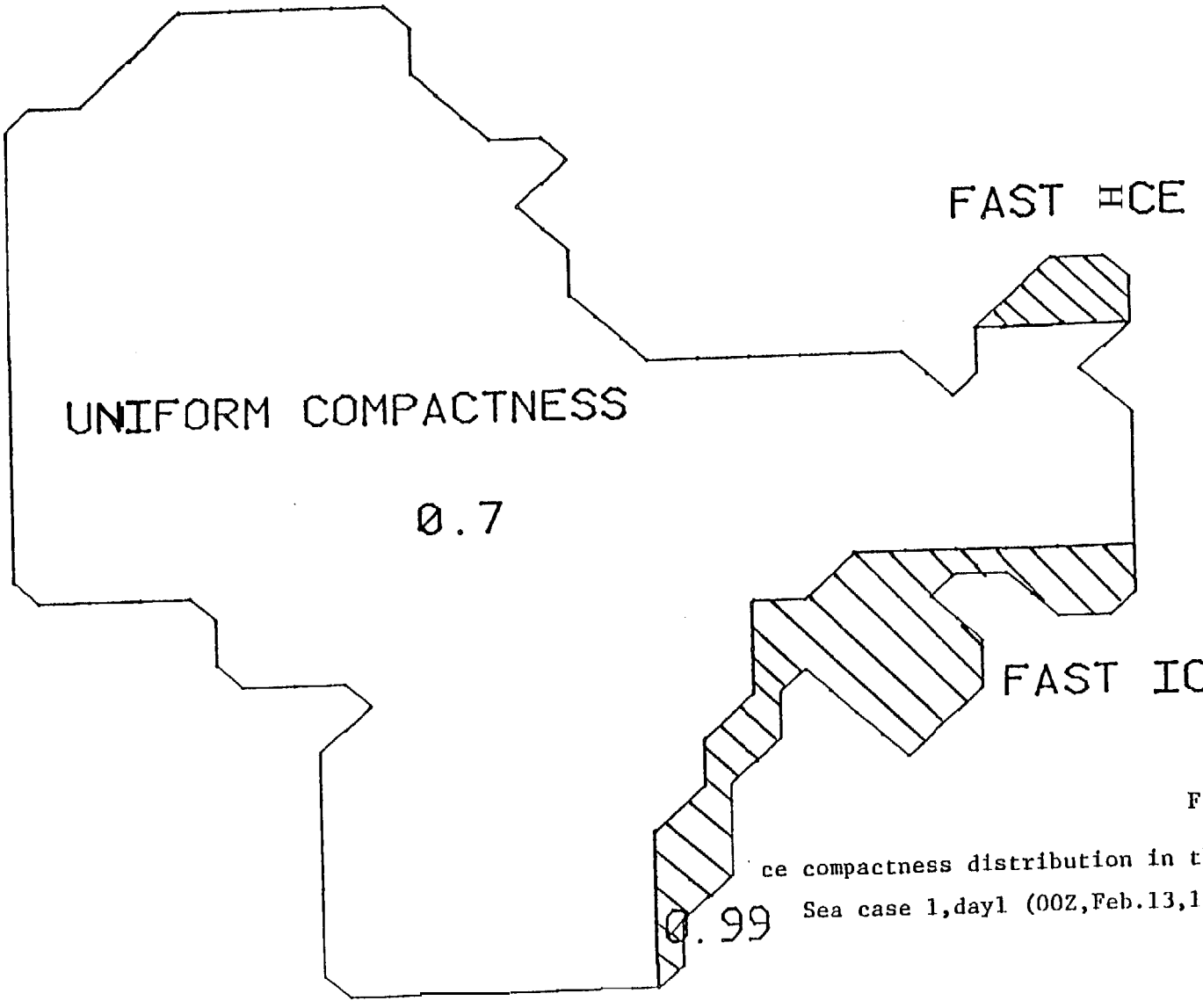

FIG.47

ce compactness distribution in the northeastern Bering Sea case 1,day1 (00Z,Feb.13,1982).

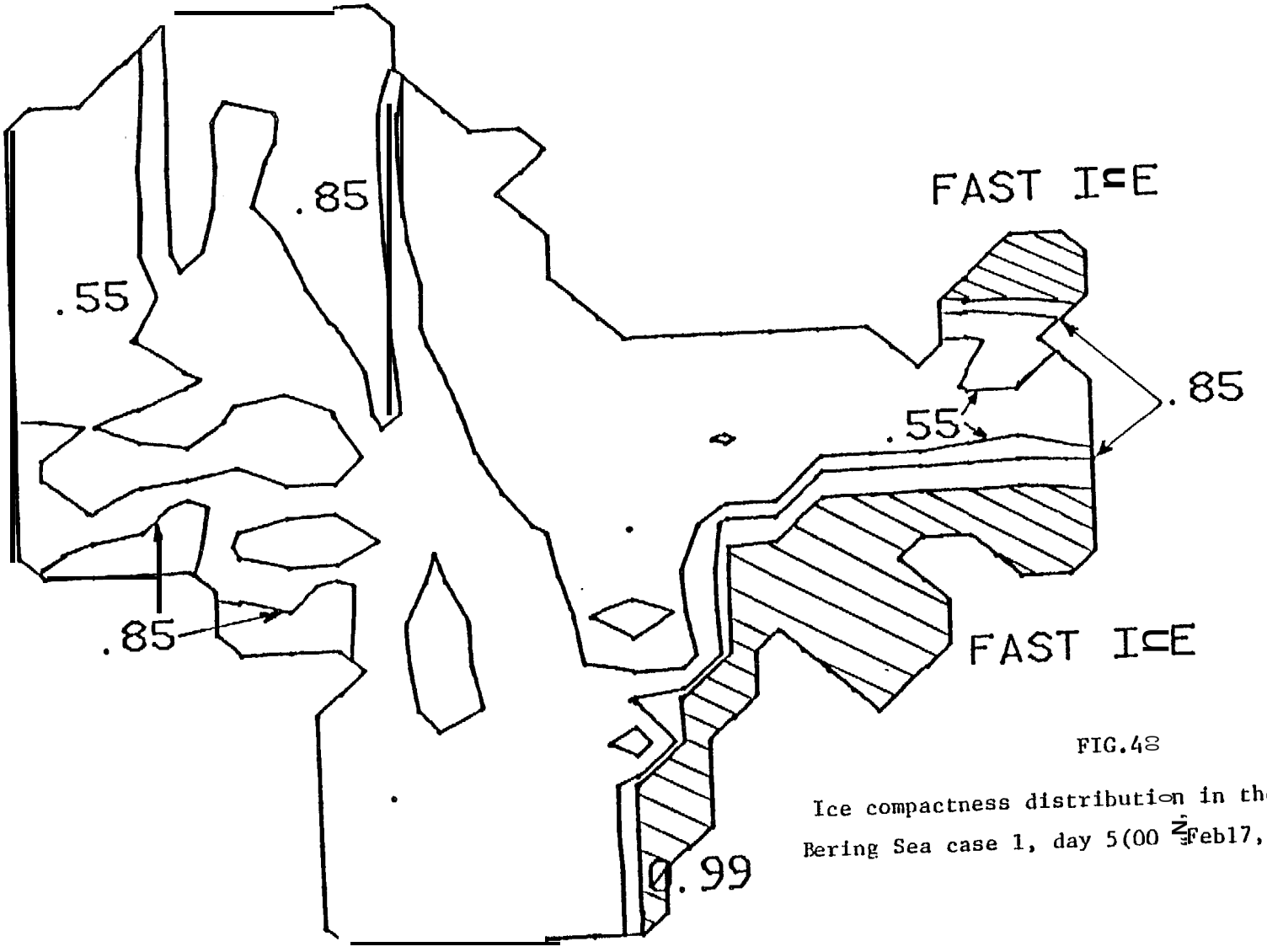

FIG.48

Ice compactness distribution in the northeastern Bering Sea case 1, day 5(00 Z Feb17,1982).

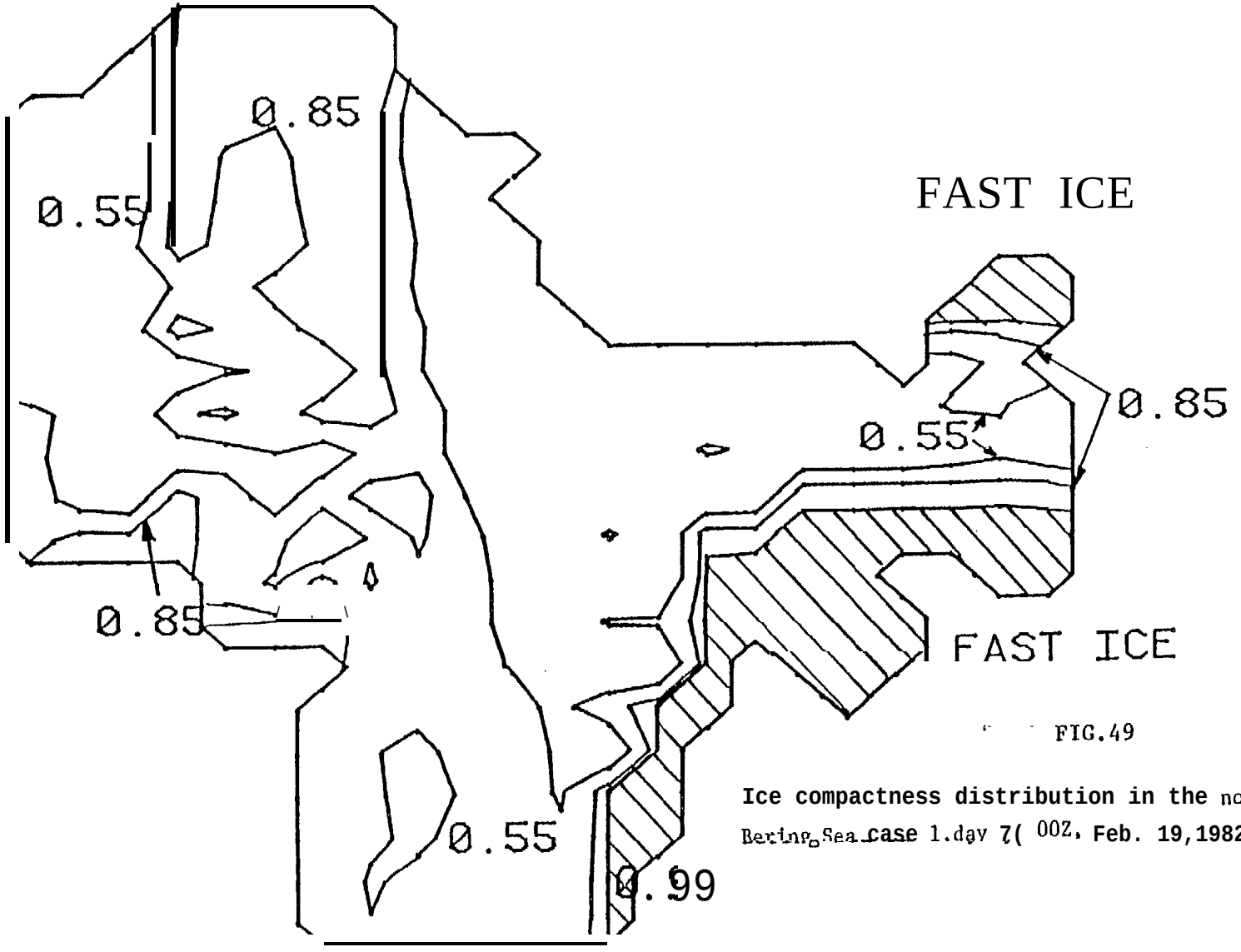

FIG.49

Ice compactness distribution in the northeastern Bering Sea case 1.day 7(00Z, Feb. 19,1982).

ICE COMPACTNESS) DAY 7

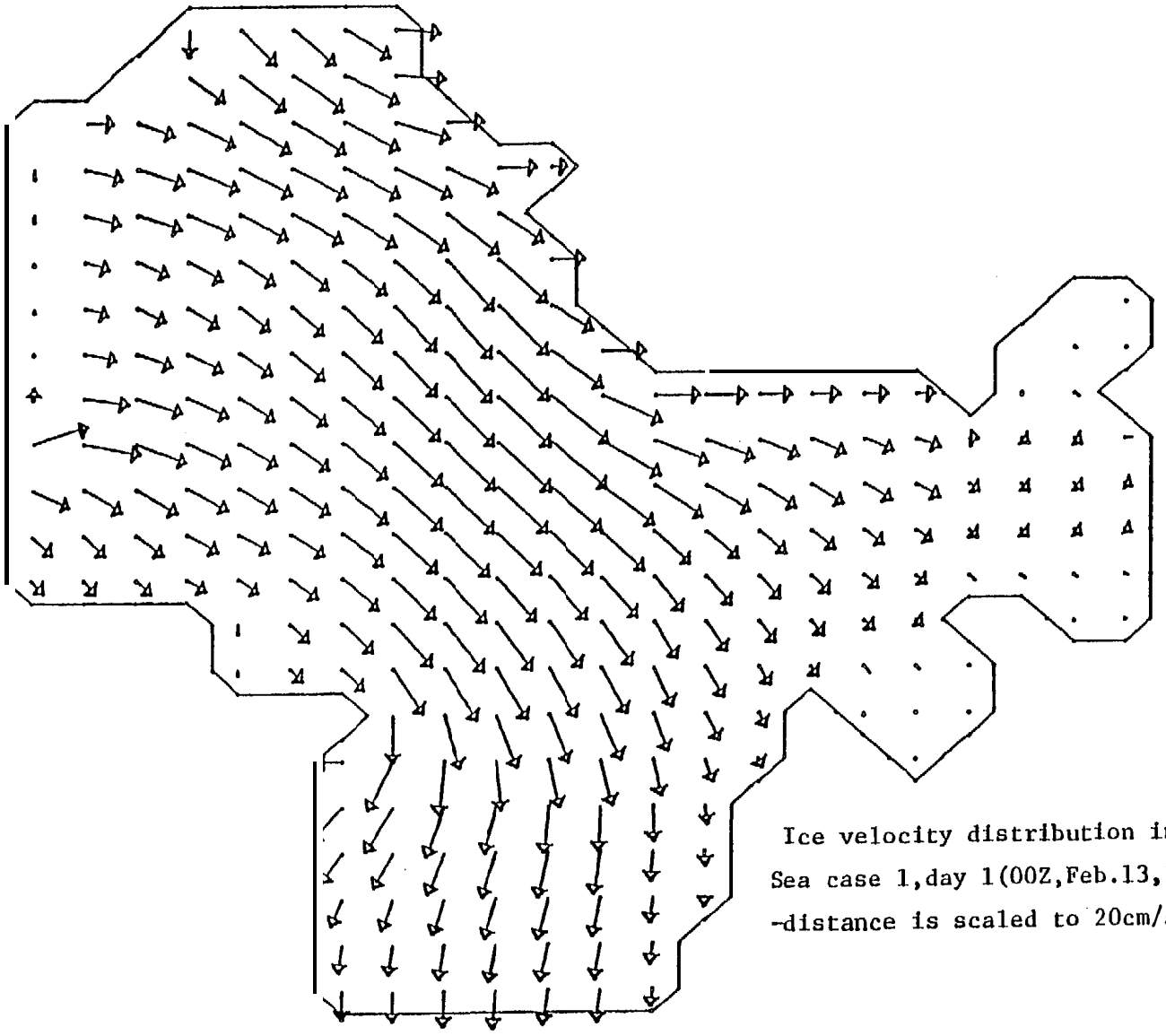

FIG.5

Ice velocity distribution in the northeastern Bering Sea case 1,day 1(00Z,Feb.13,1982).One horizontal grid-distance is scaled to 20cm/s.

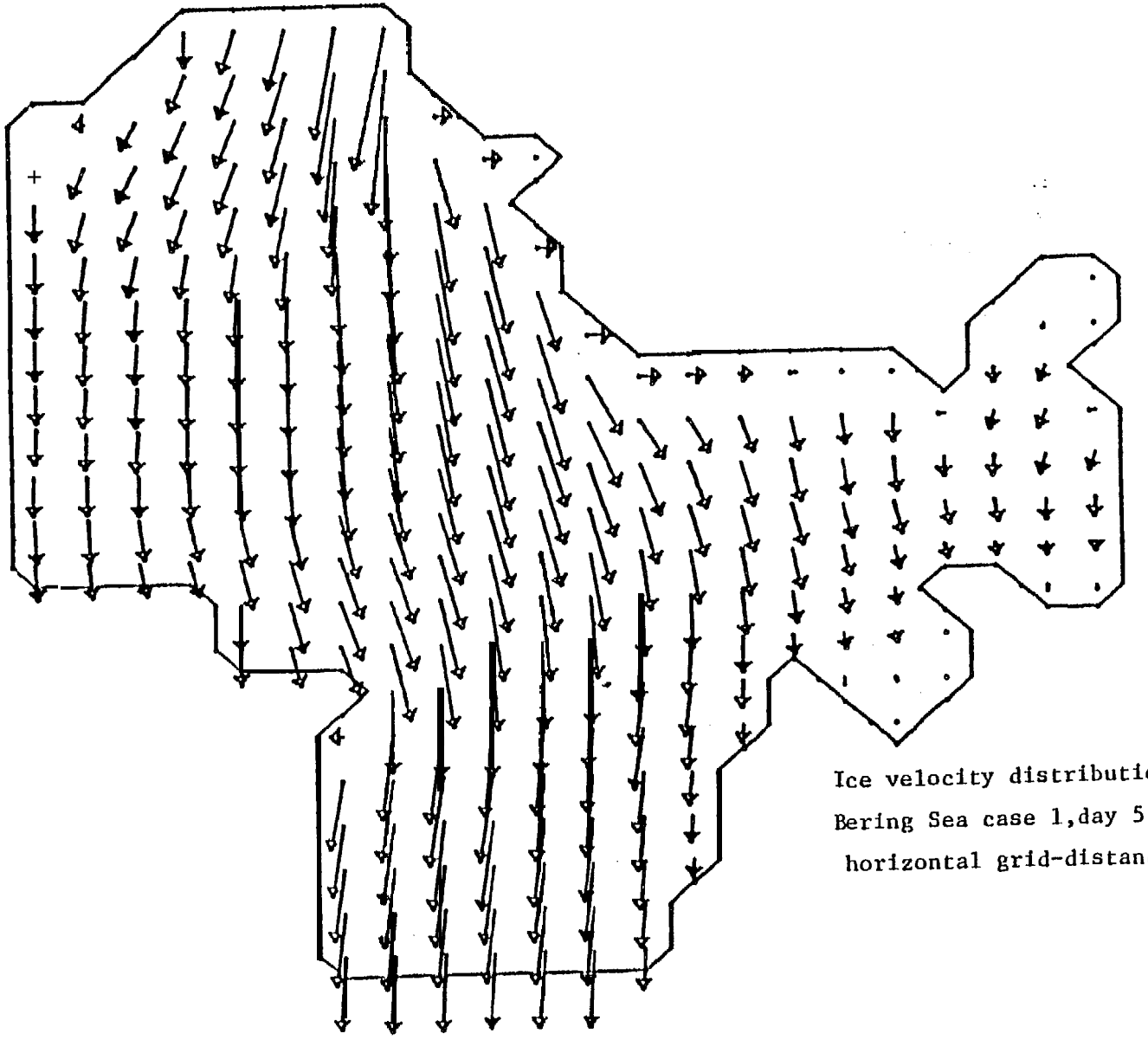

FIG.51

Ice velocity distribution in the northeastern Bering Sea case 1,day 5(00Z,Feb.17,1982). One horizontal grid-distance is scaled to 40 cm/s

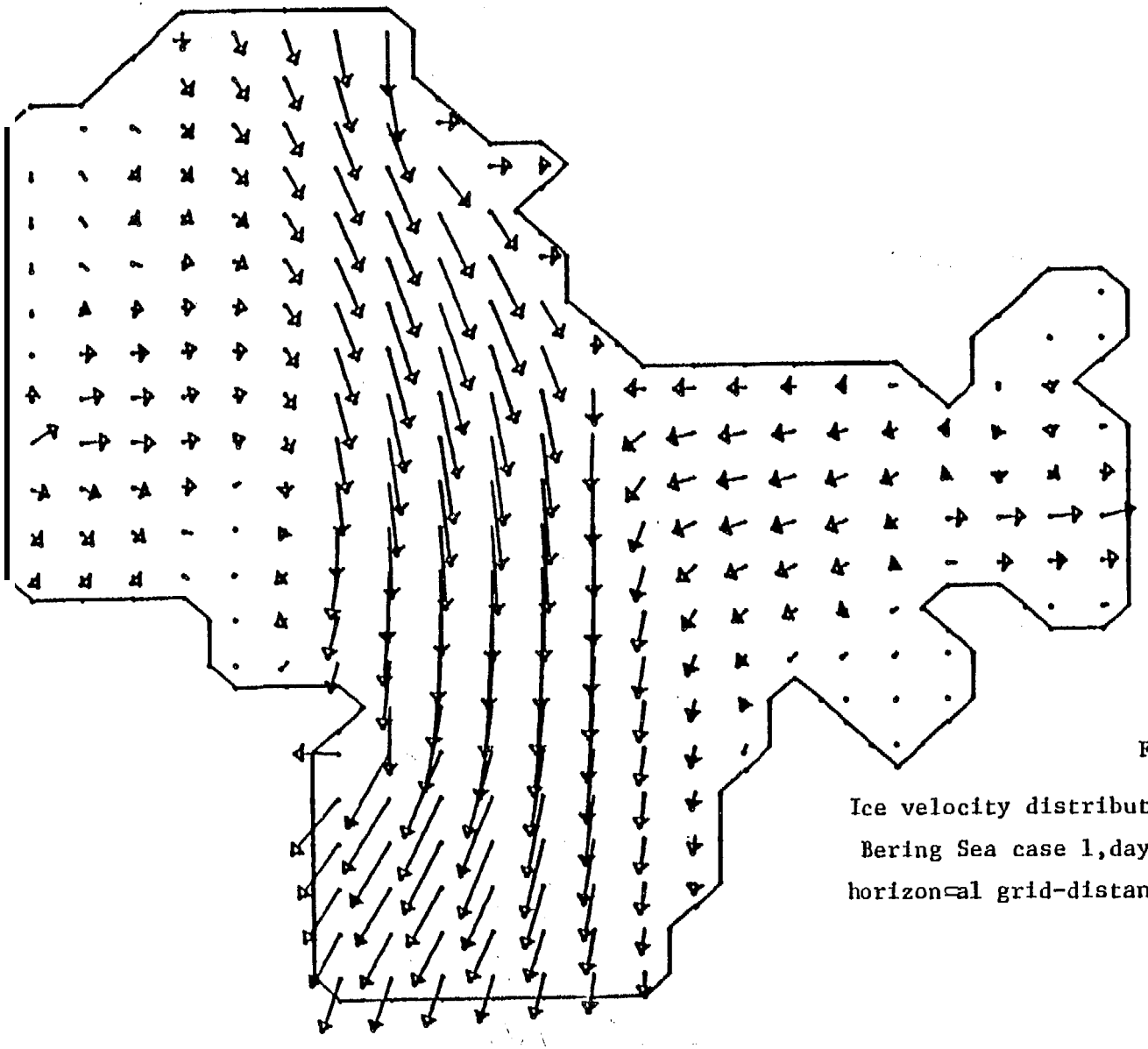

FIG.52

Ice velocity distribution in the northeastern Bering Sea case 1, day 7 (00Z, Feb.19, 1982). One horizontal grid-distance is scaled to 20 cm/s.

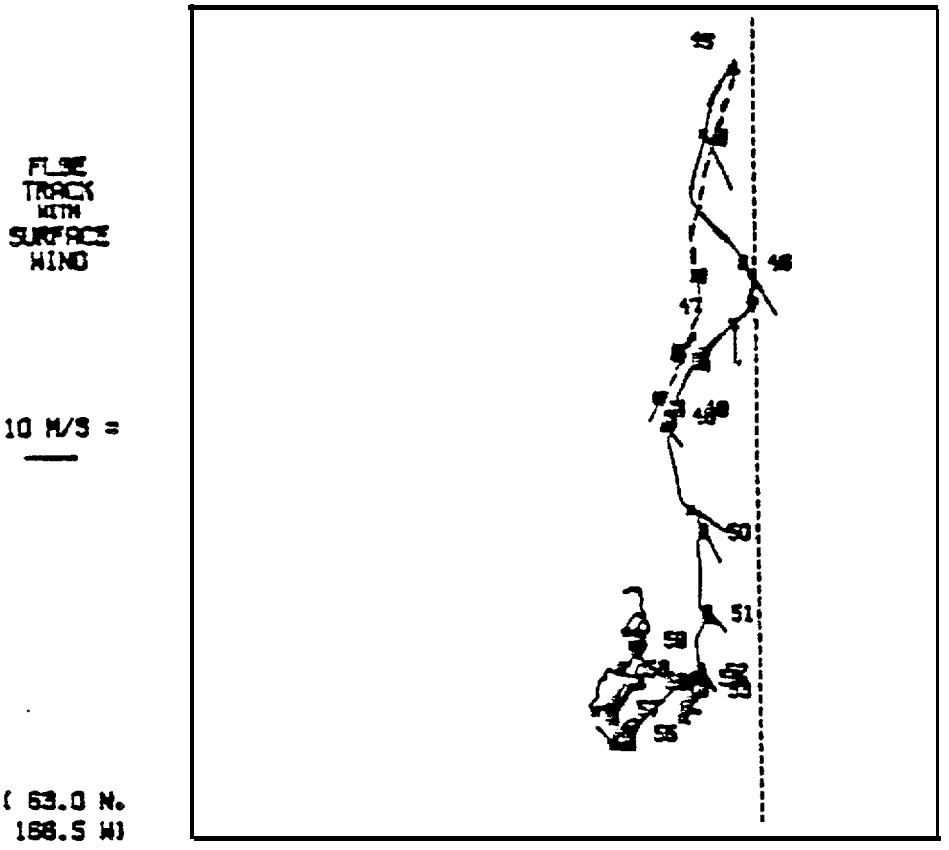

FIG.53

Ice drift floe track, case 1,February 14-28 (JD 45-59). Measured by lds and Pease(1984) (Floe station 2322B)- continuous line, and calculated from model - broken line.

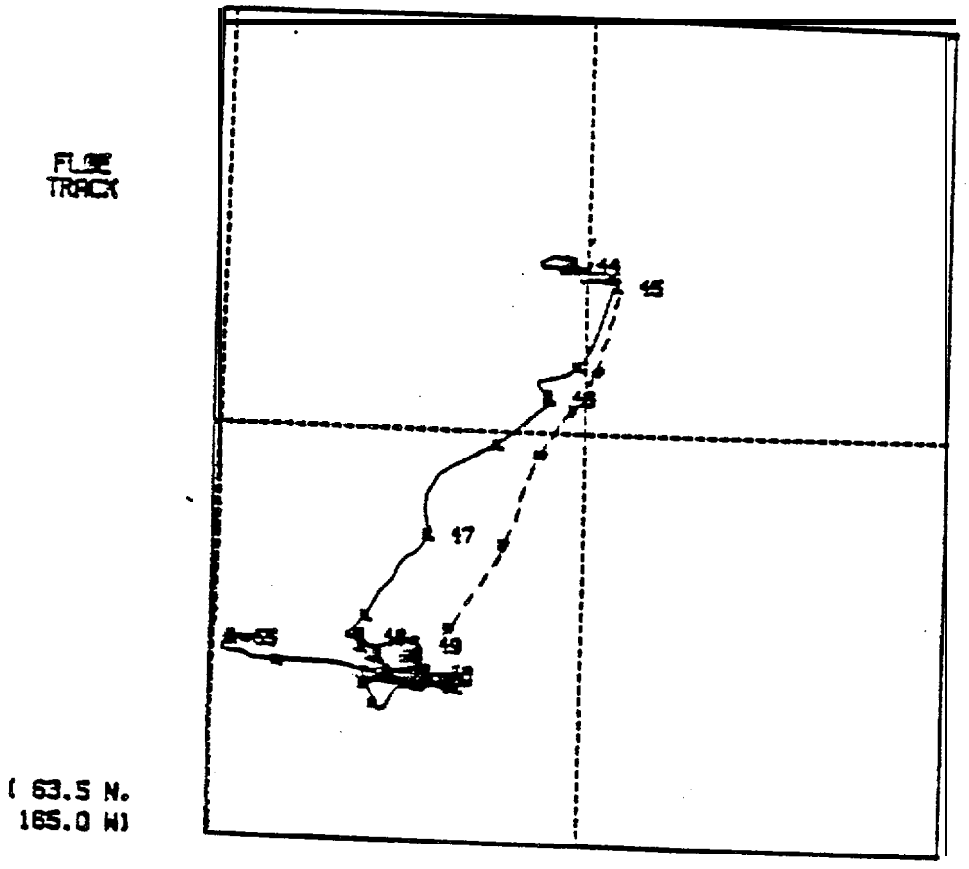

FIG.54

Ice drift floe track , case 1,February 13-28,1982 (JD 44-59) Measured by Reynolds and Pease (1984)(floe station 2321B)- continuous line , and calculated from model -broken line.

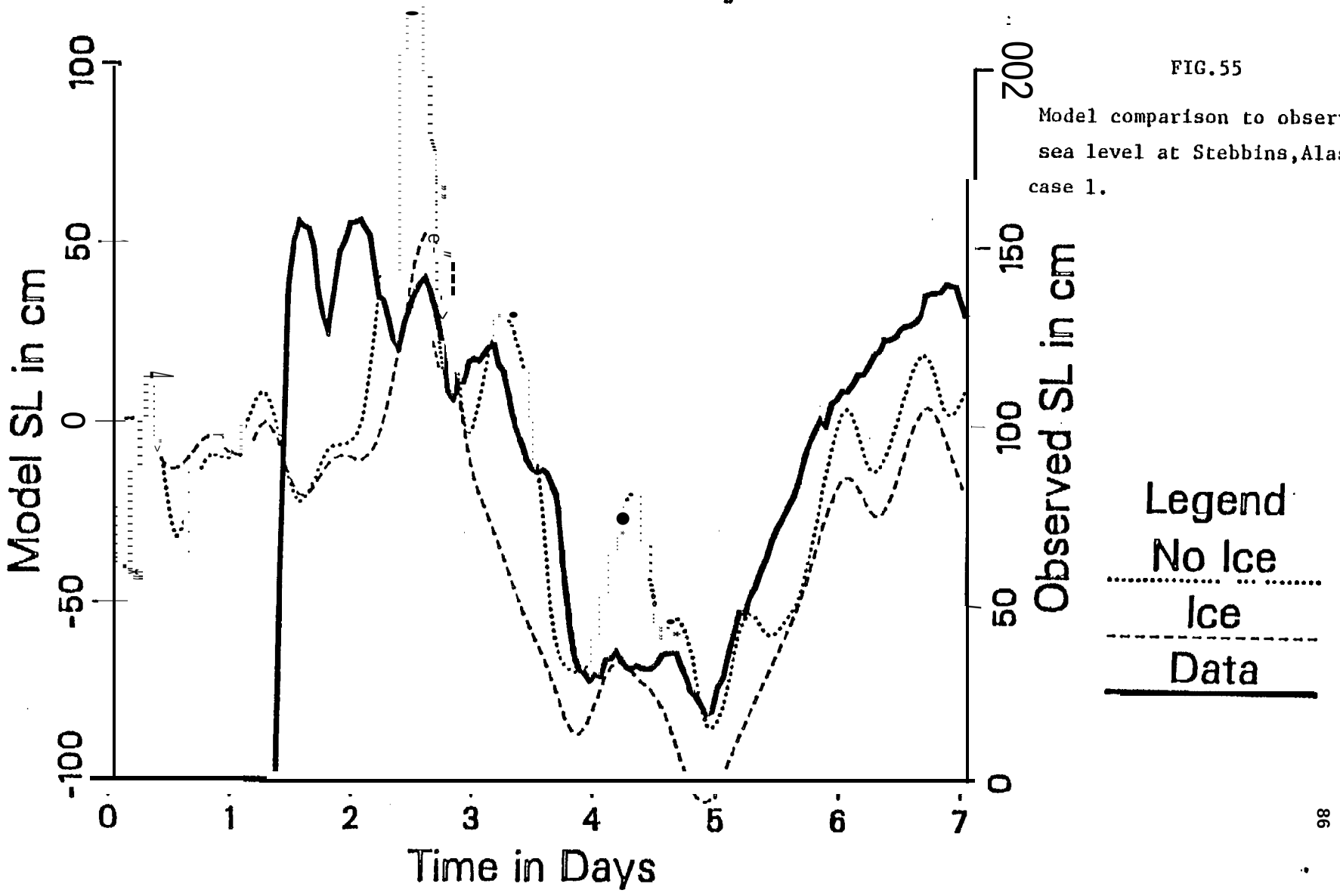

FIG.55

Model comparison to observed sea level at Stebbins,Alaska, case 1.

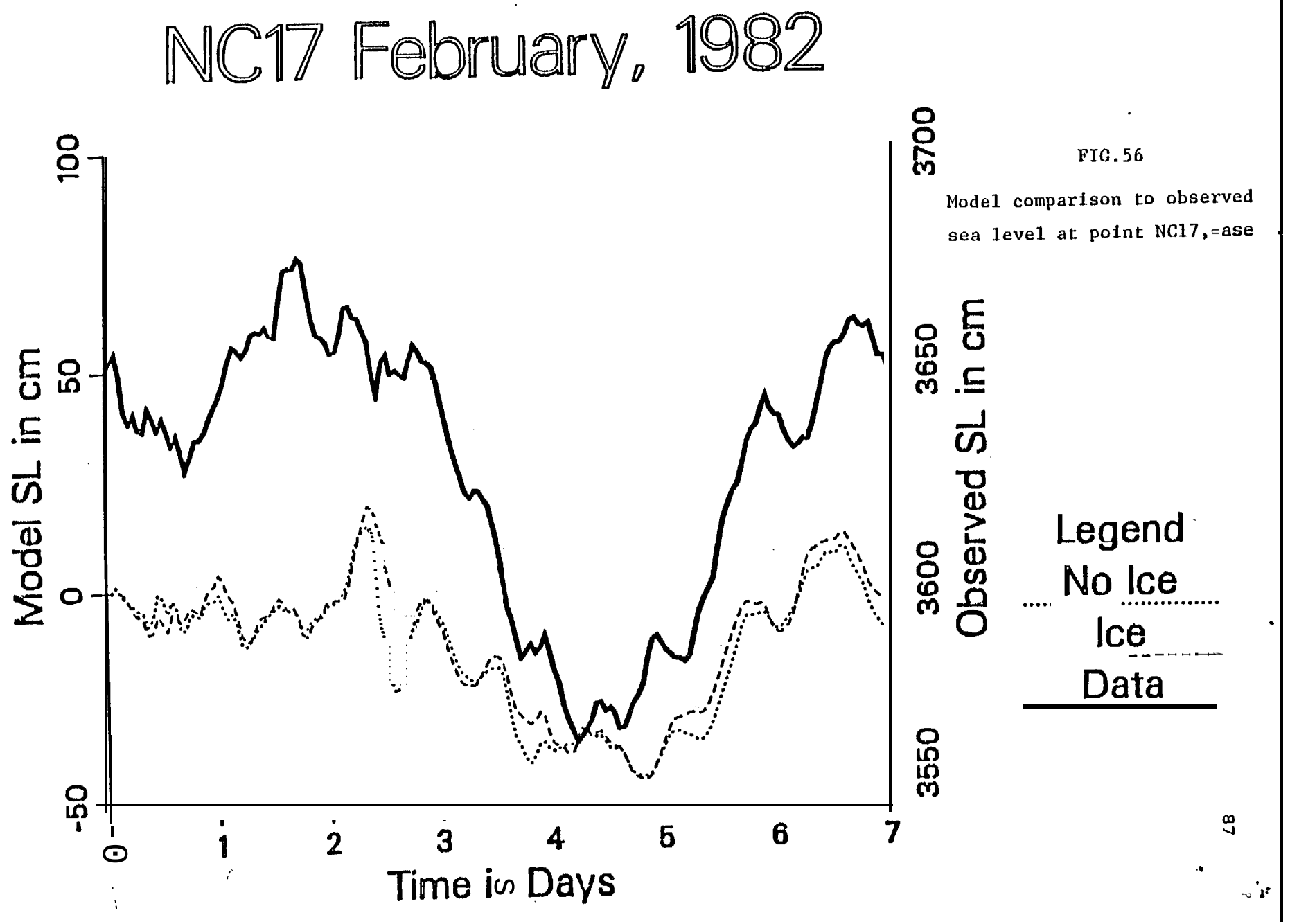

FIG.56

Model comparison to observed sea level at point NC17,=ase

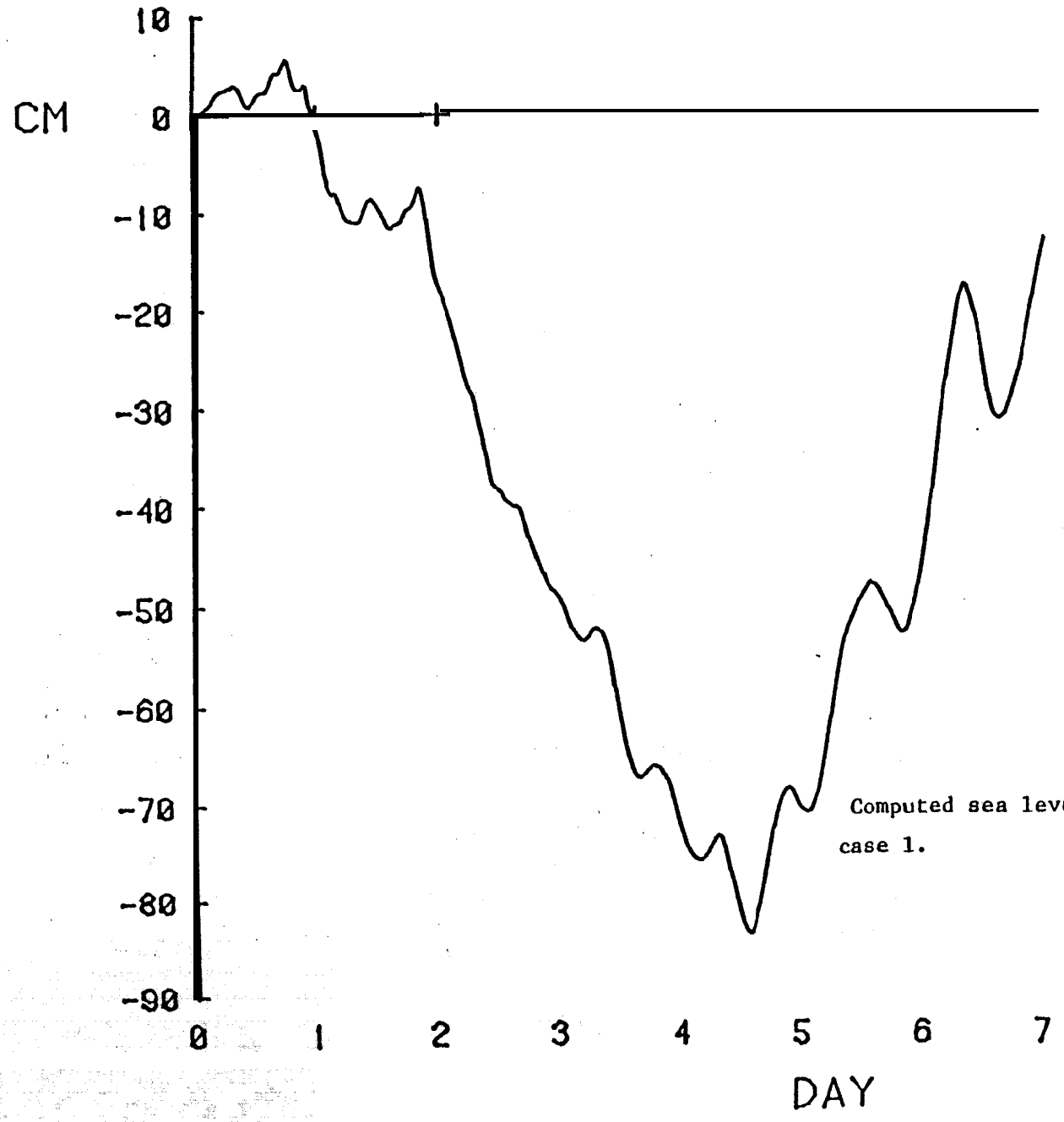

FIG.57

Computed sea level time series at Diomedes, case 1.

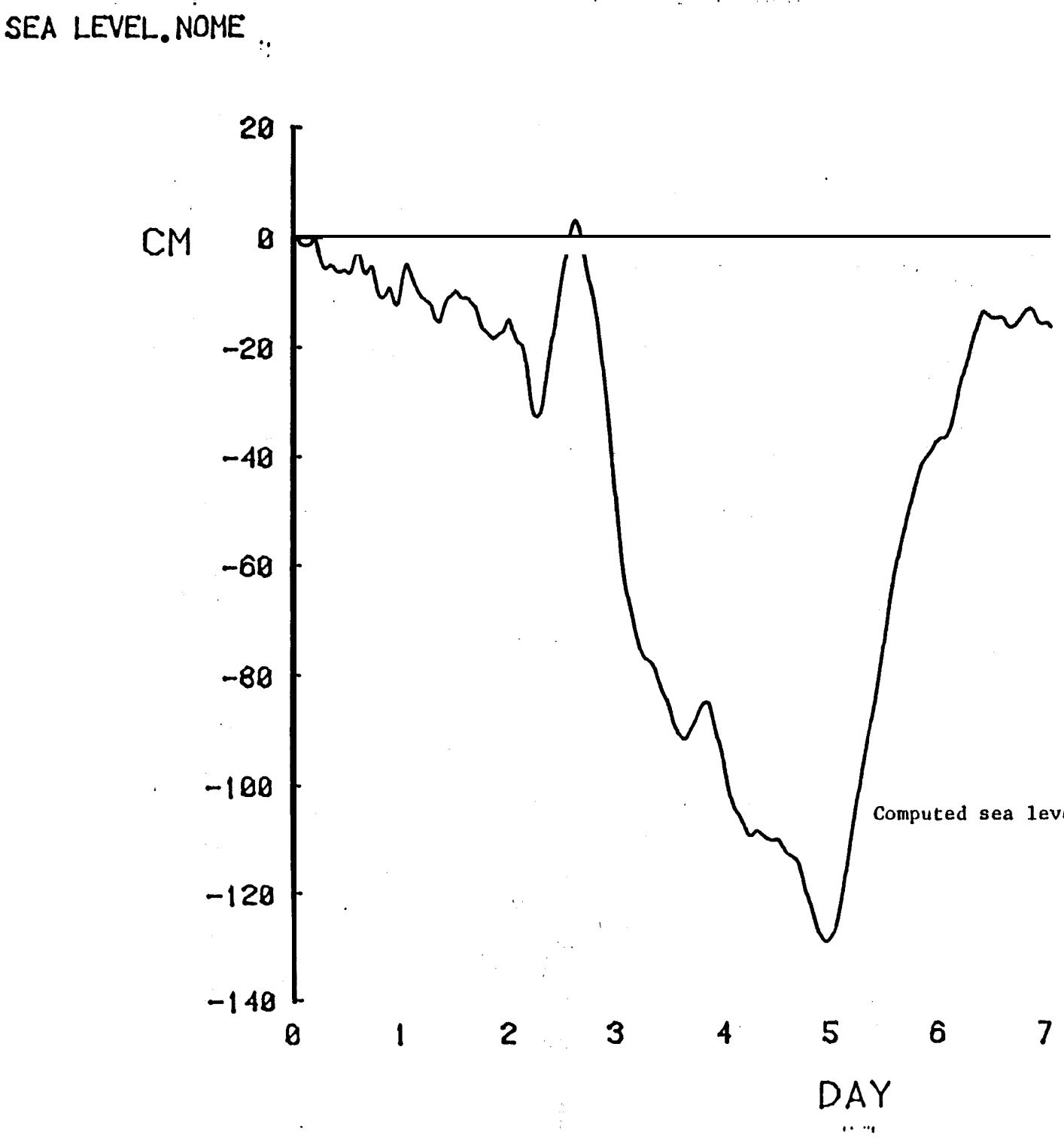

FIG.58

Computed sea level time series at Nome, case 1.

SEA LEVEL, UNALAKLEET

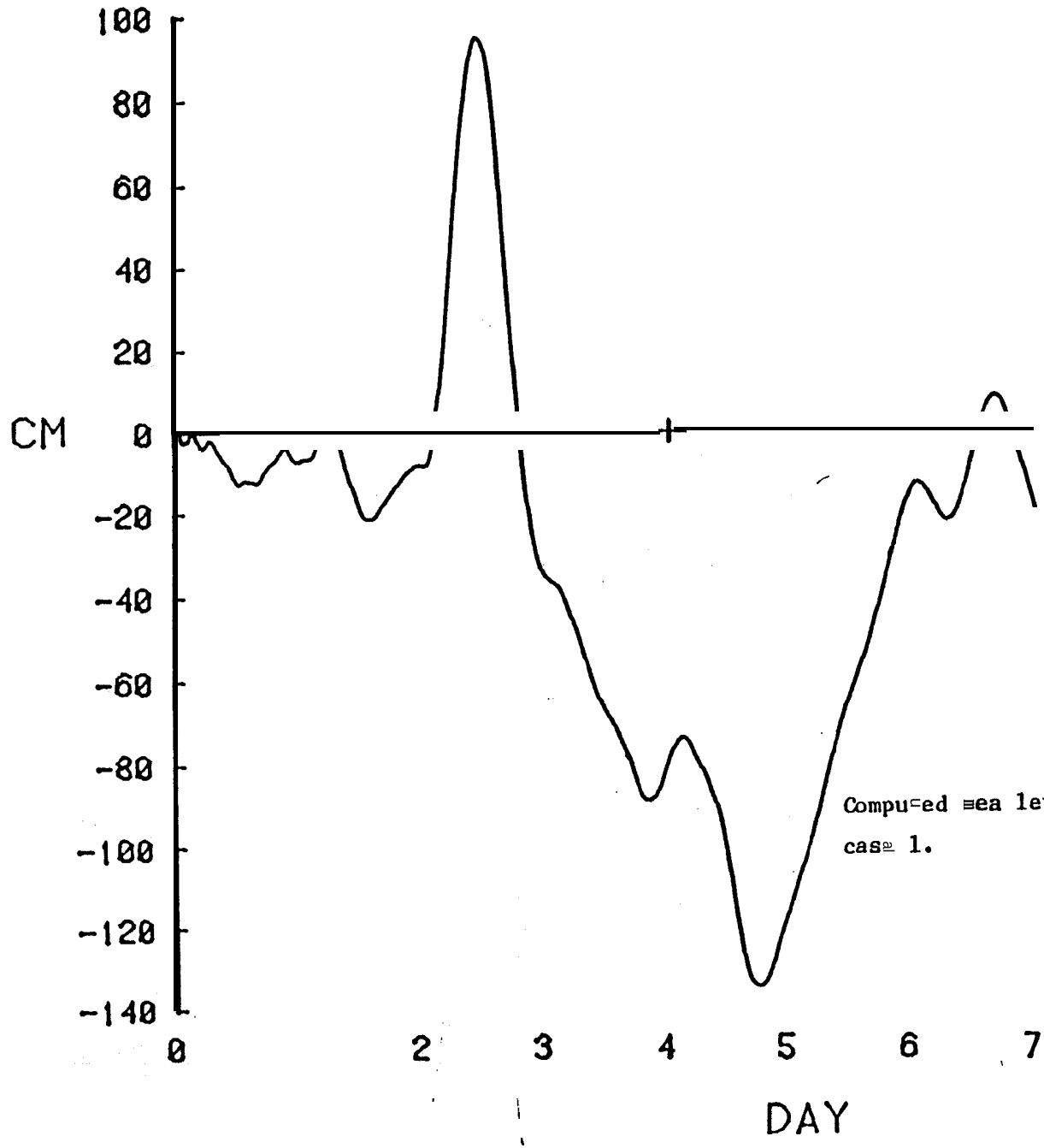

FIG.59

Computed sea level time series at Unalakleet, case 1.

SEA LEVEL, YUKON

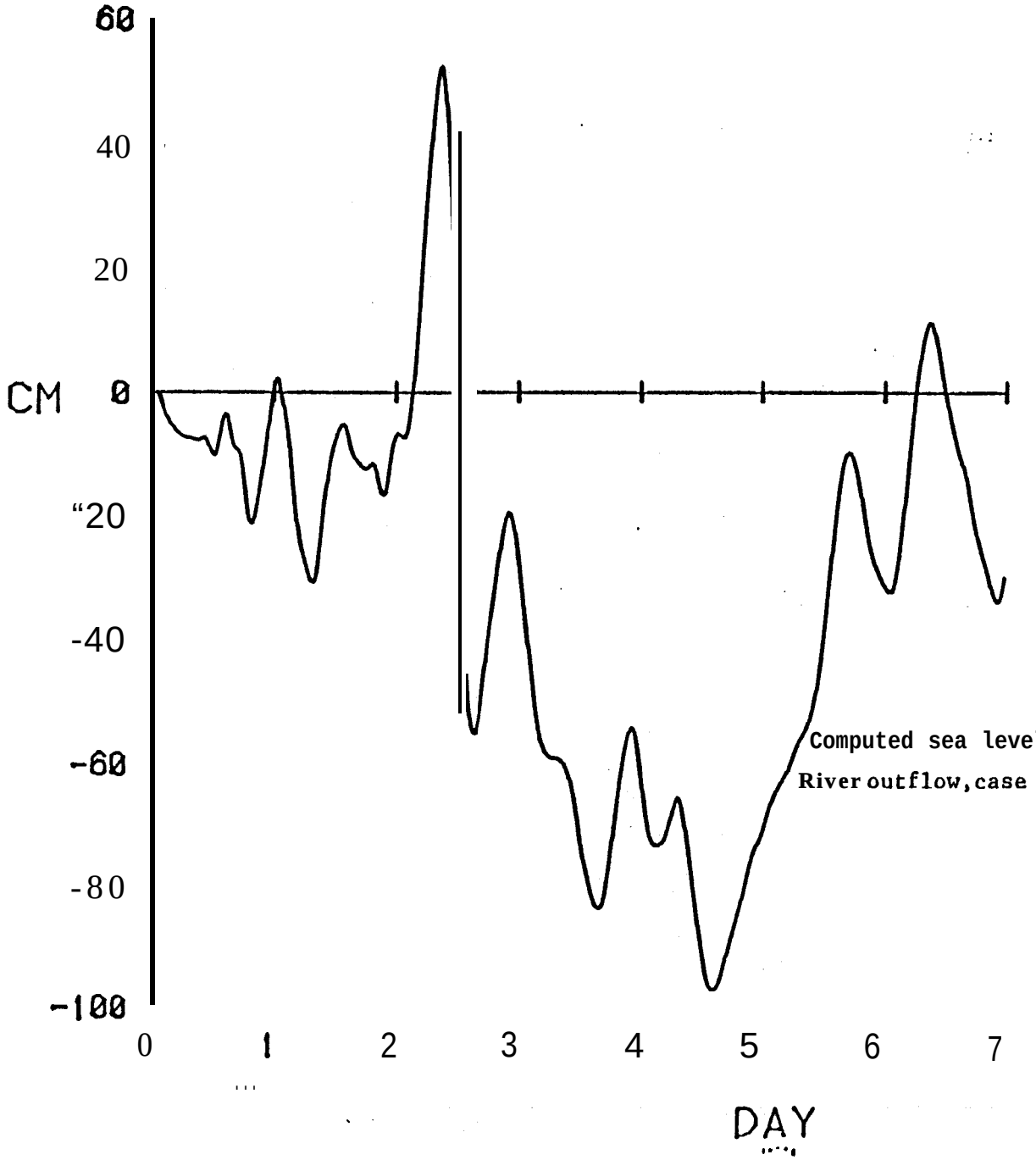

FIG.60
Computed sea level time series at the Yukon River outflow, case 1.

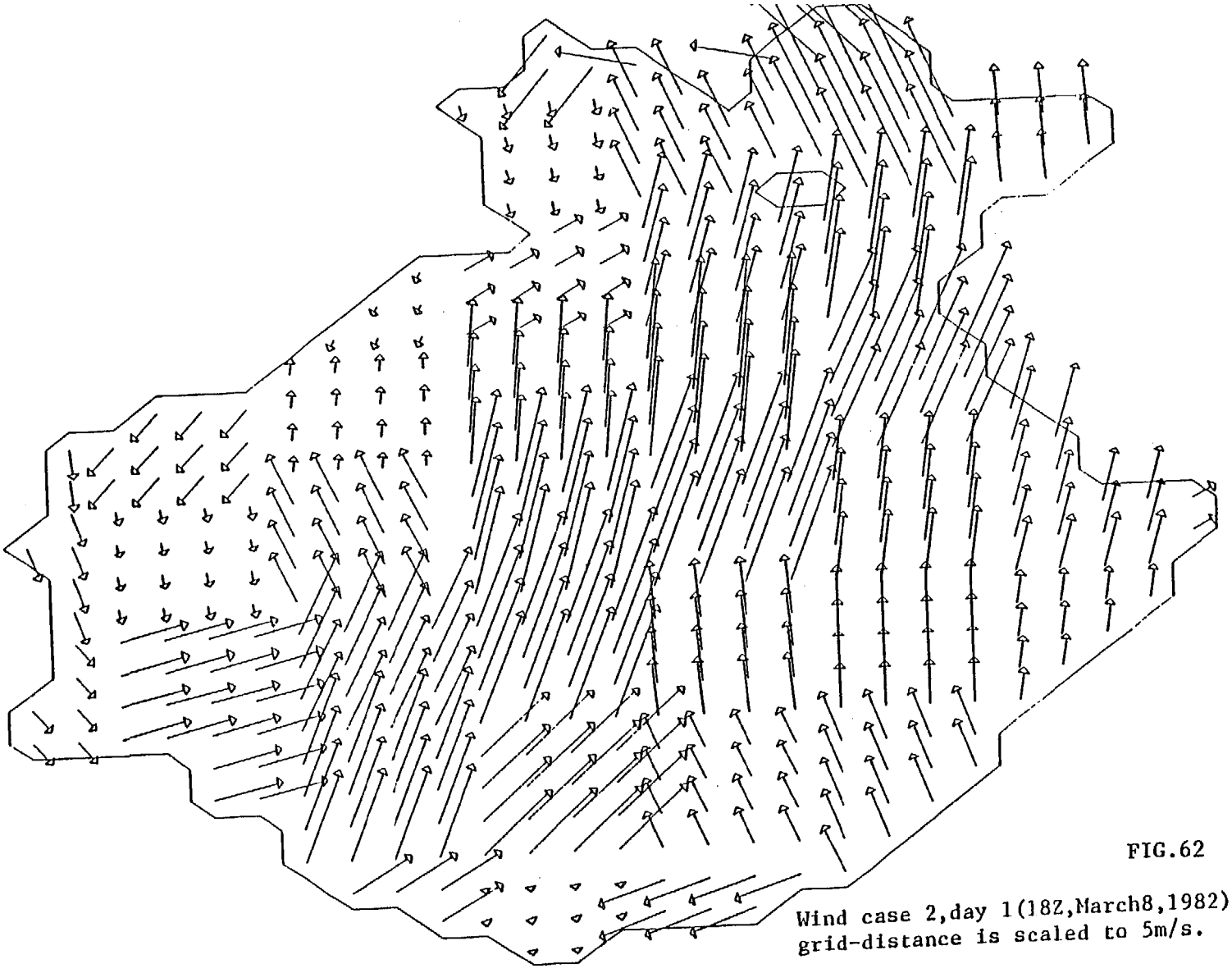

FIG.62

Wind case 2,day 1(18Z,March8,1982). One horizontal grid-distance is scaled to 5m/s.

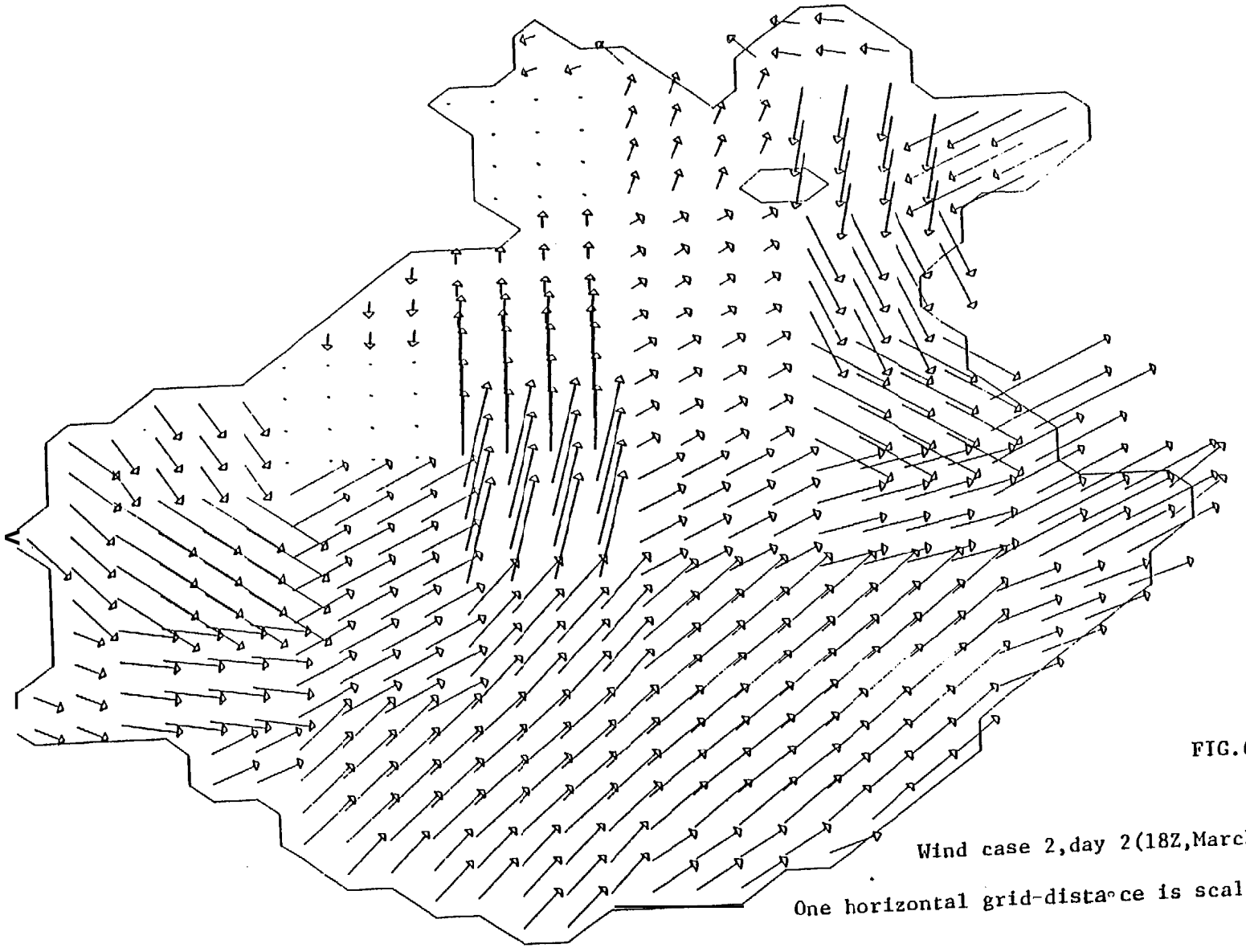

FIG.63

Wind case 2,day 2(18Z,March 9,1982).

One horizontal grid-distance is scaled to 5m/s.

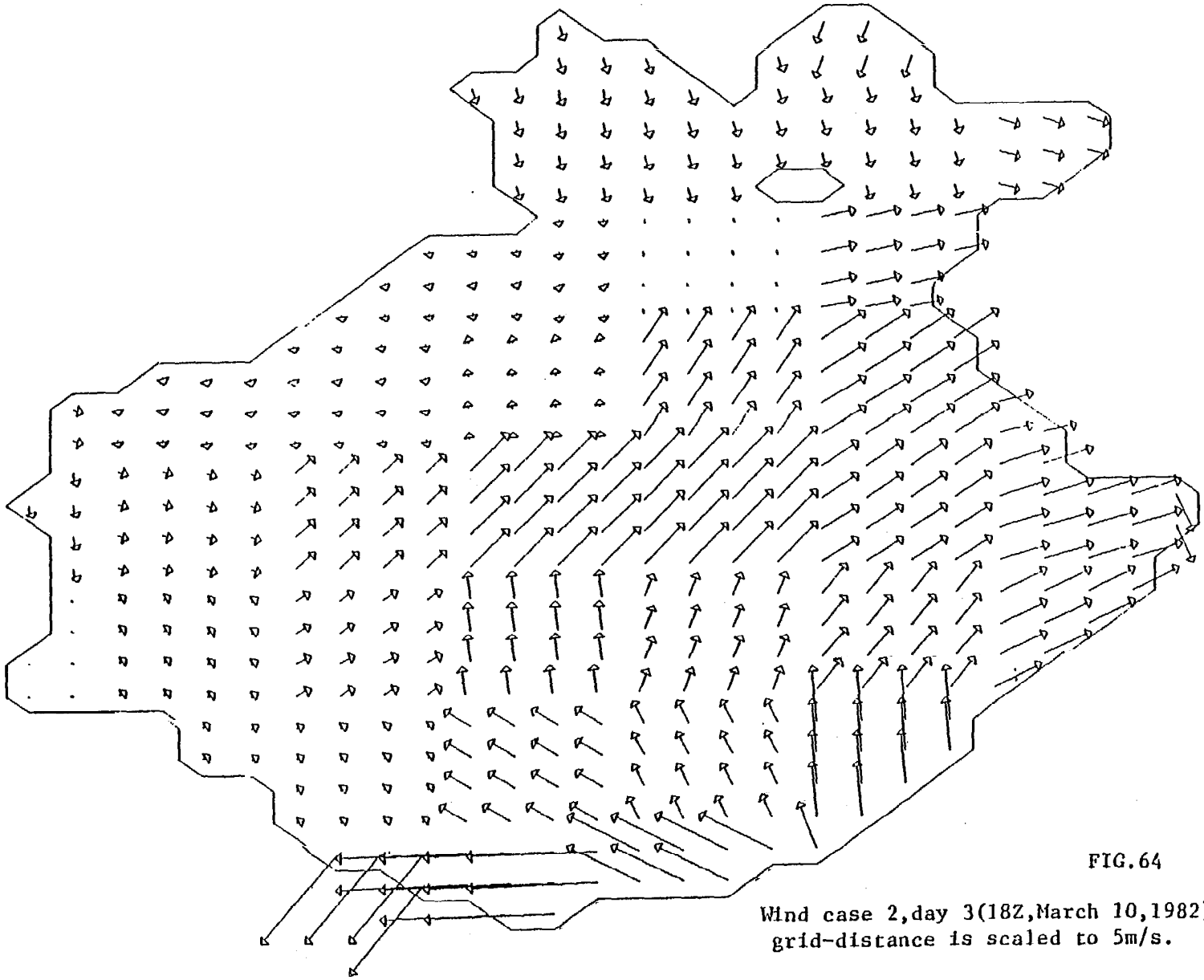

FIG.64

Wind case 2,day 3(18Z,March 10,1982). One horizontal grid-distance is scaled to 5m/s.

WIND 72 HOURS

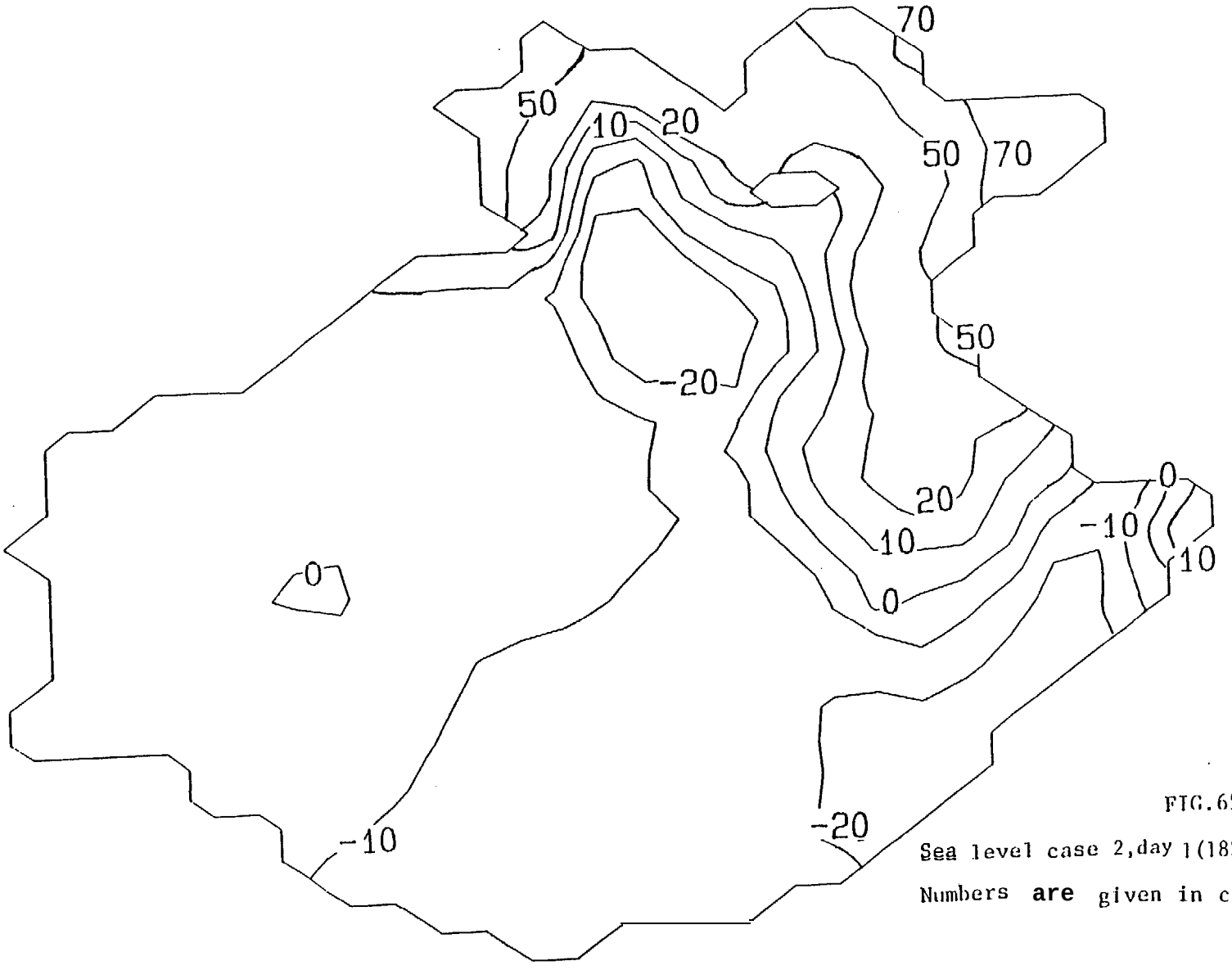

FIG.65

Sea level case 2,day 1(18Z,March 8,19[12).

Numbers are given in cm. .

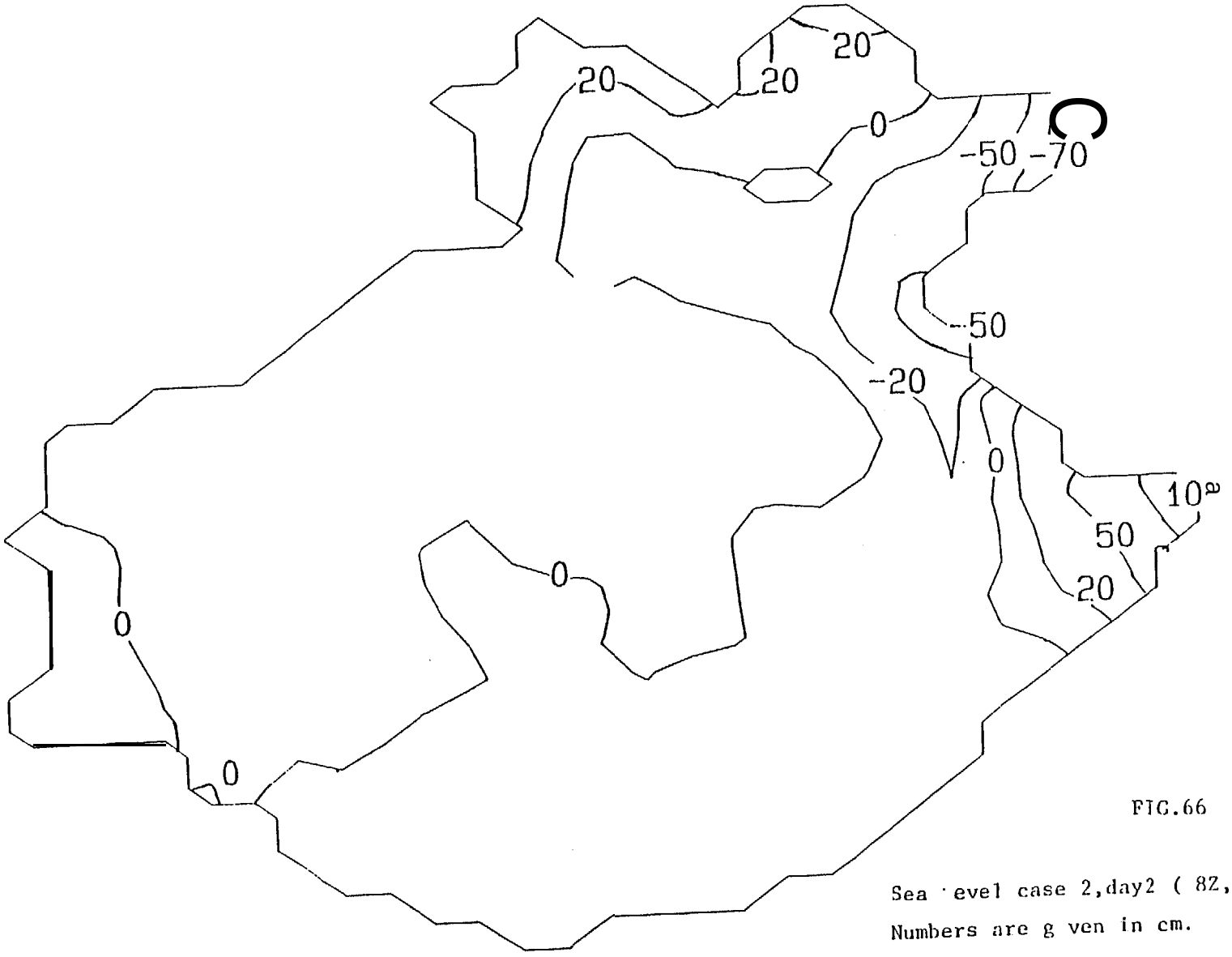

FIG.66

Sea level case 2,day2 (8Z,March 9,1982).
Numbers are given in cm.

SL DAY 2

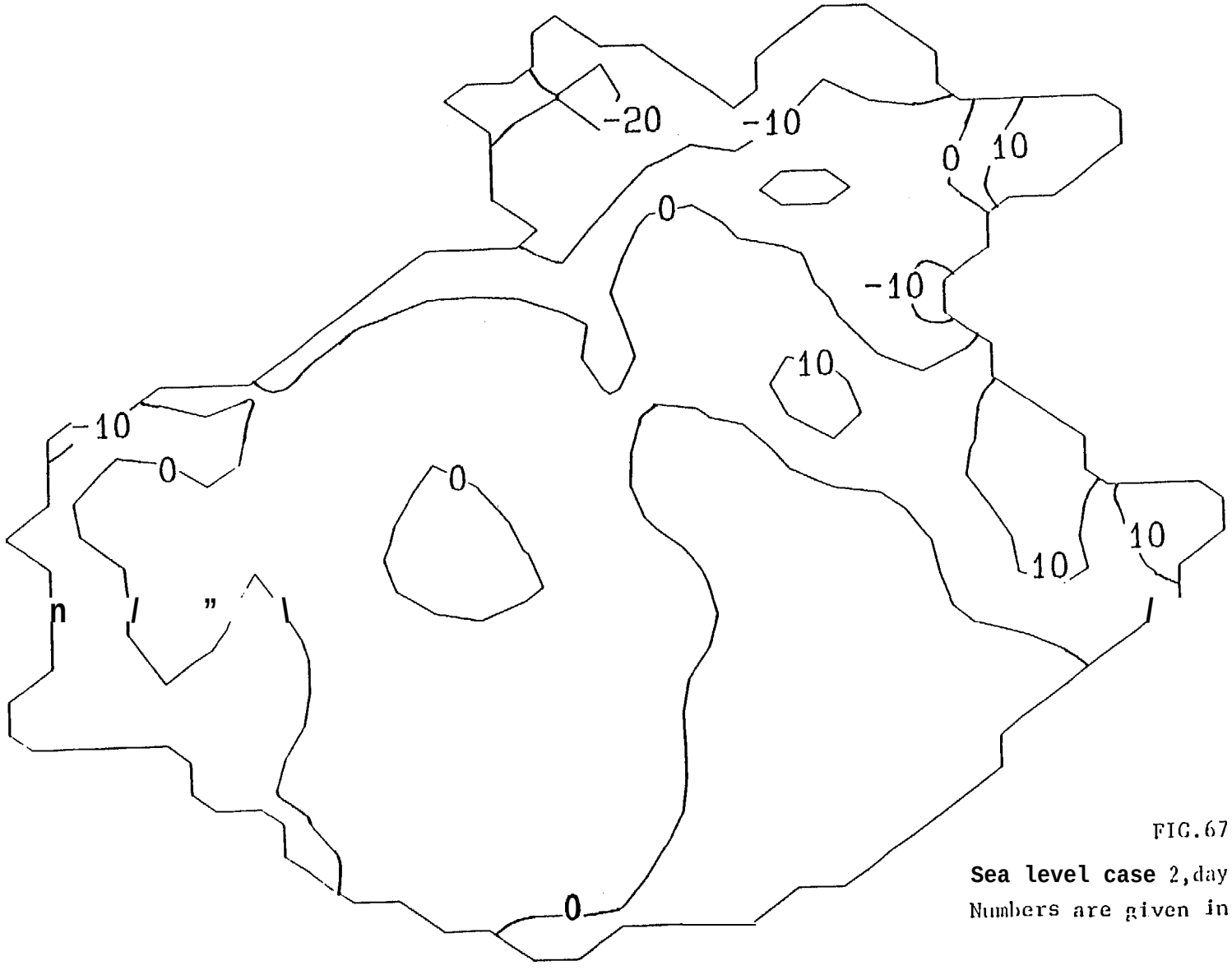

SL DAY 3

FIG.67

Sea level case 2, day 3(18Z, March10, 1982

Numbers are given in **cm.**

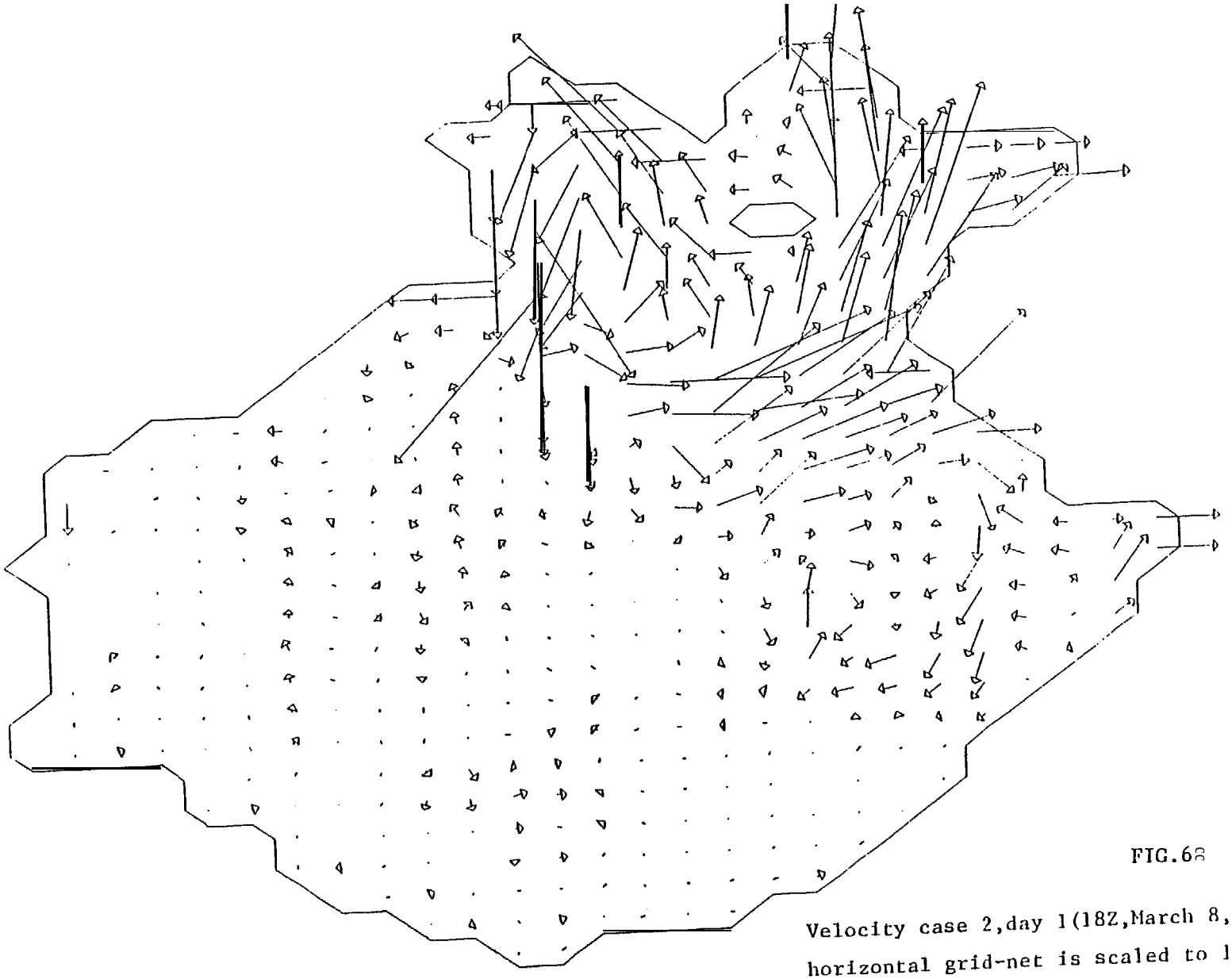

FIG.68

Velocity case 2,day 1(18Z,March 8,1982). One horizontal grid-net is scaled to 10 cm/s.

V DAY 1

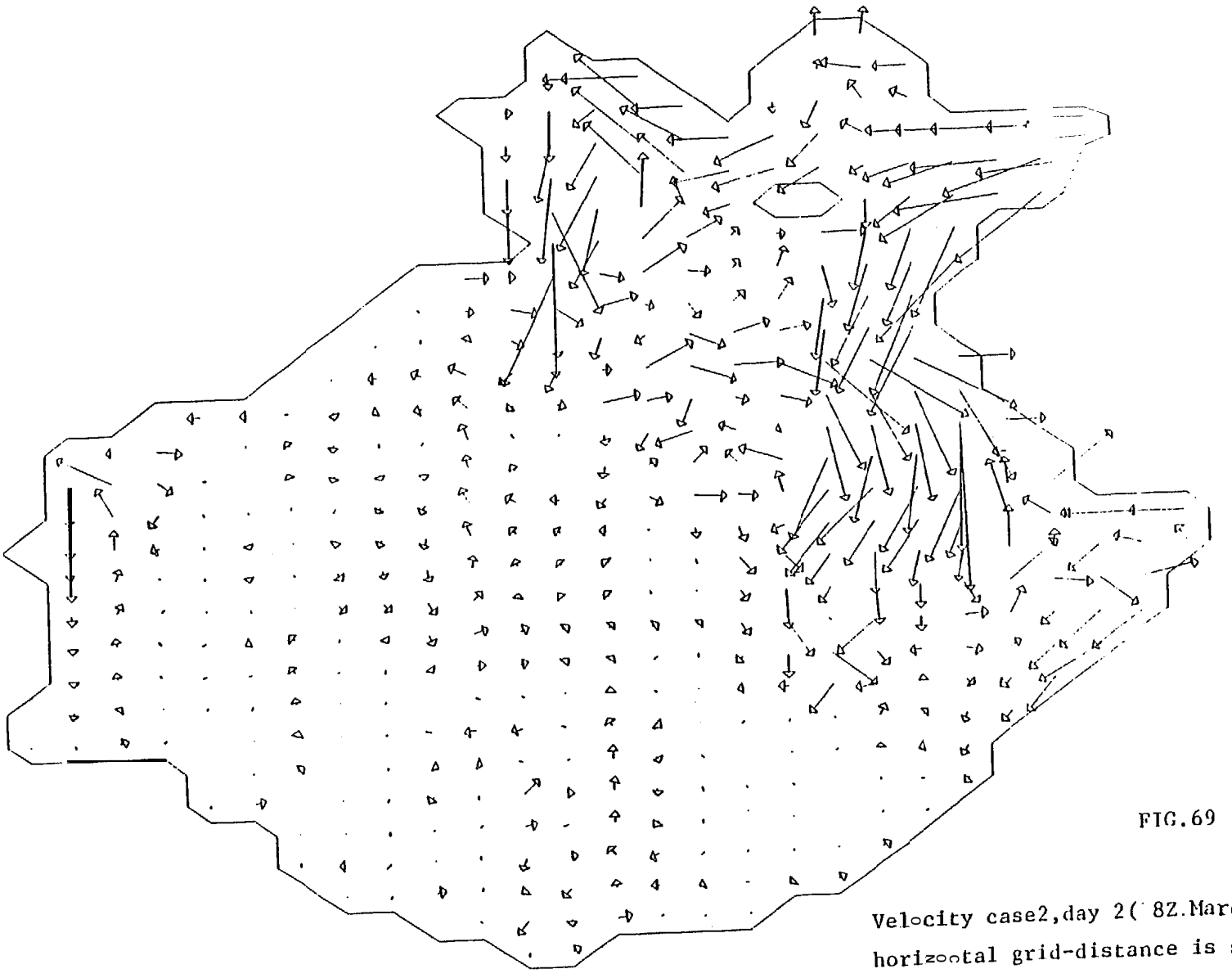

FIG.69

Velocity case2,day 2(8Z.Marcl 9,1982). One horizootal grid-distance is sca ed to 10cm/s.

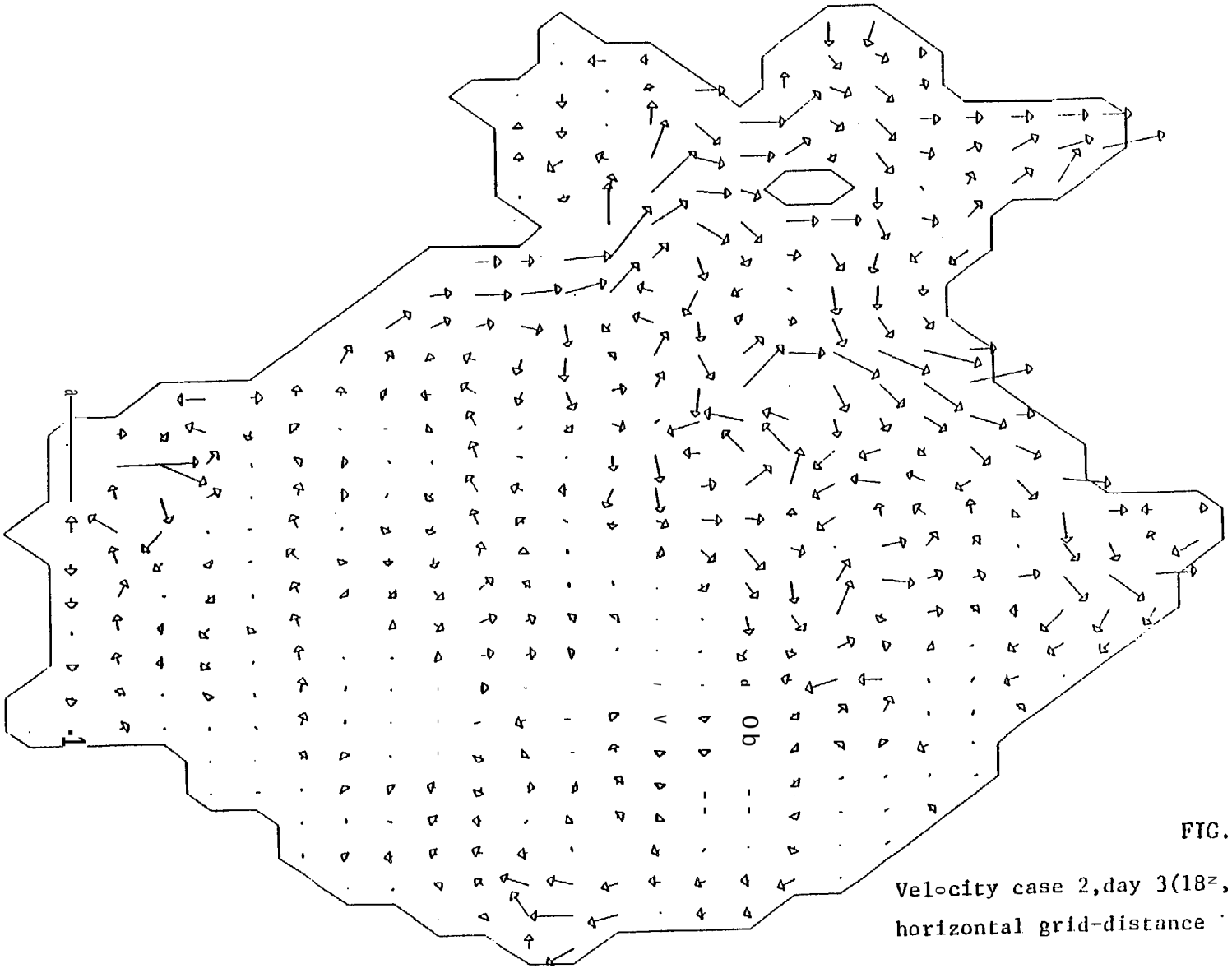

FIG.70

Velocity case 2,day 3(18^{z},March 0,1982). One horizontal grid-distance is scaled to 10cm/s.

V DAY 3

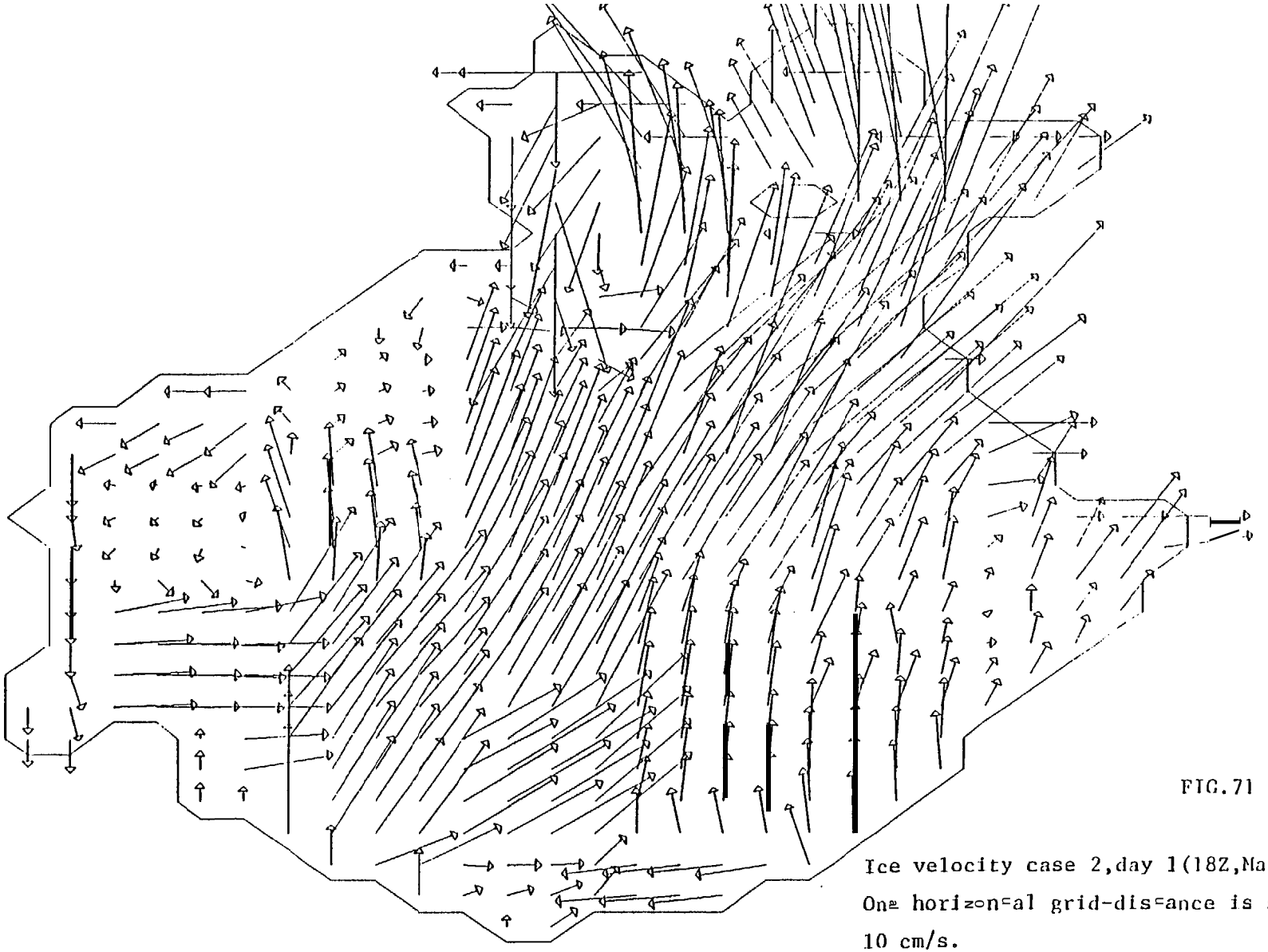

FIG.71

Ice velocity case 2,day 1(18Z,March 8,1982). One horizontal grid-distance is scaled to 10 cm/s.

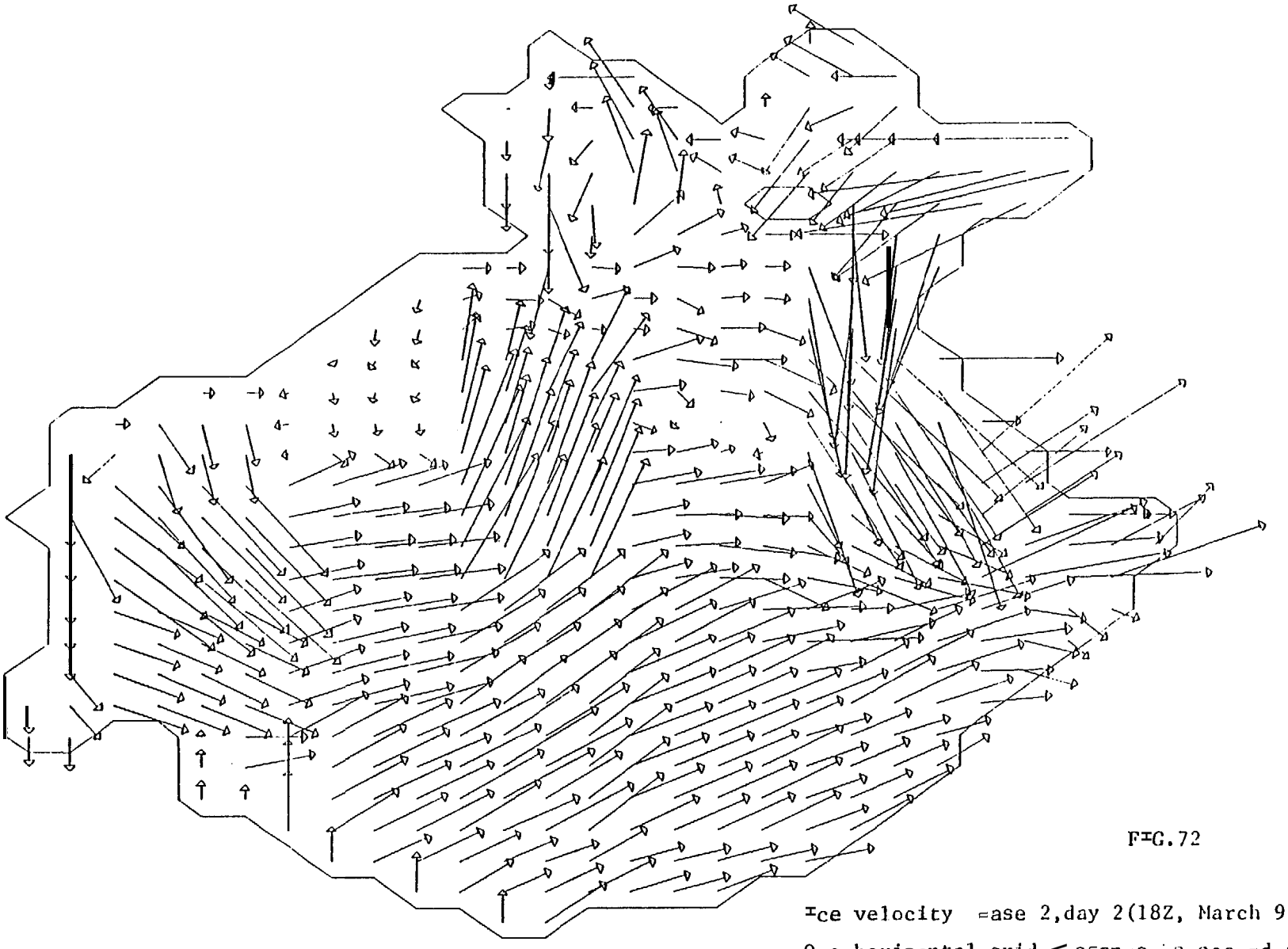

FIG. 72

Ice velocity case 2, day 2 (18Z, March 9, 1982).
One horizontal grid square is scaled to 10 cm/s.

ICE VELOCITY DAY 2

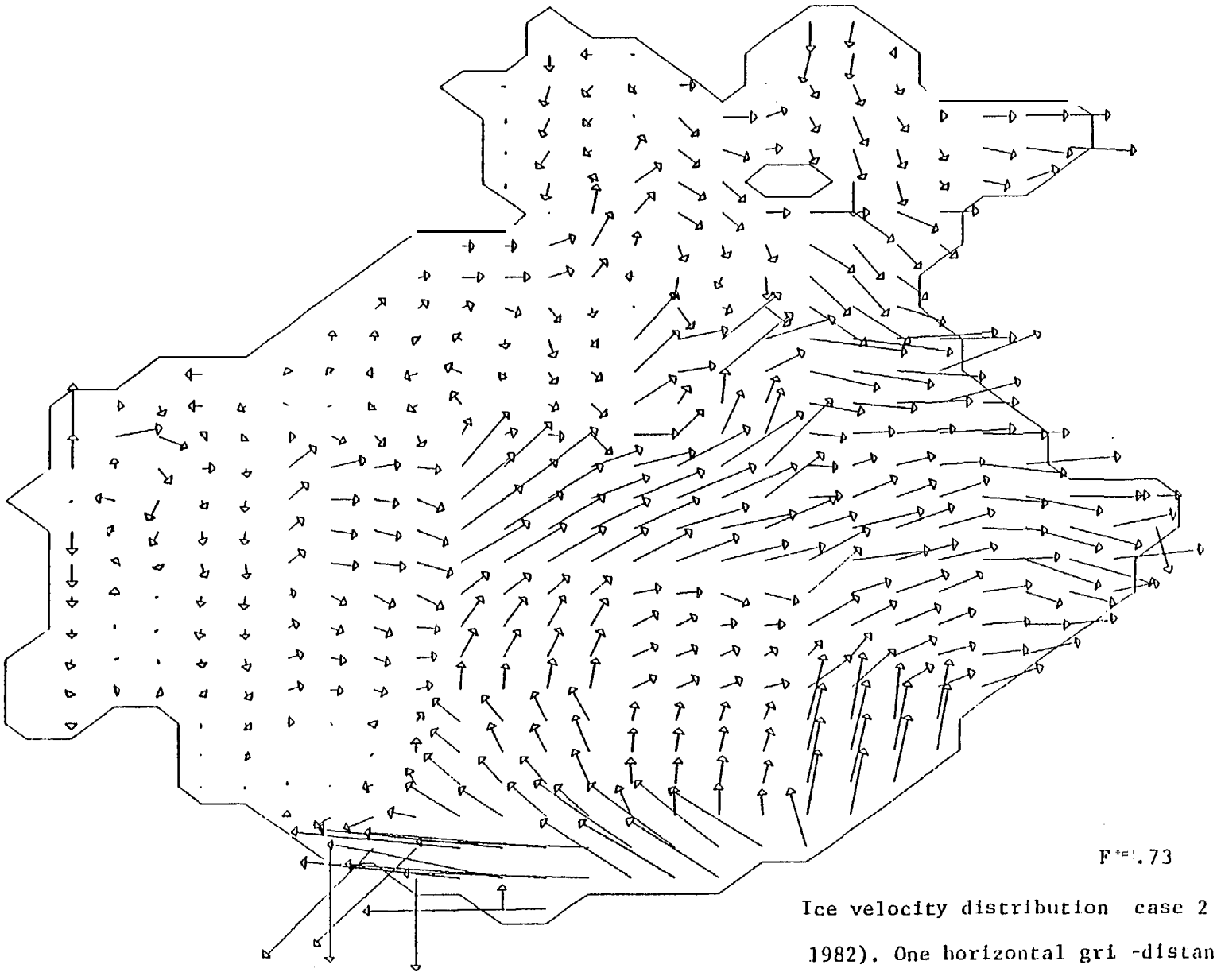

F*=.73

Ice velocity distribution case 2 day 3(18Z,March 0 1982). One horizontal gri -distance is scaled to 10 cm/s.

ICE VEI OC I TY DAY 3

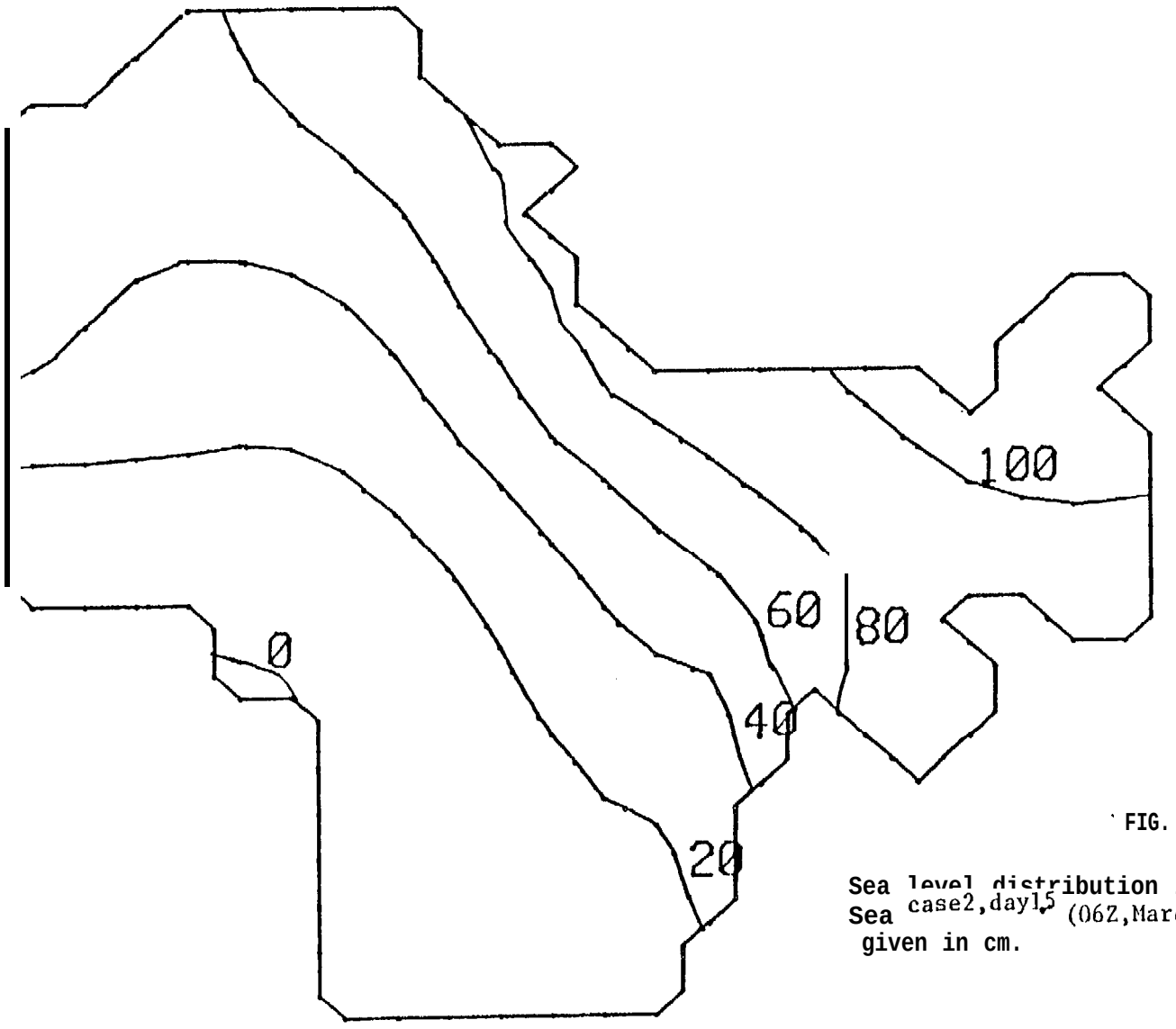

FIG. 74

Sea level distribution in the northeastern Bering Sea case2,day15 (06Z,March 9,1982). Numbers are given in cm.

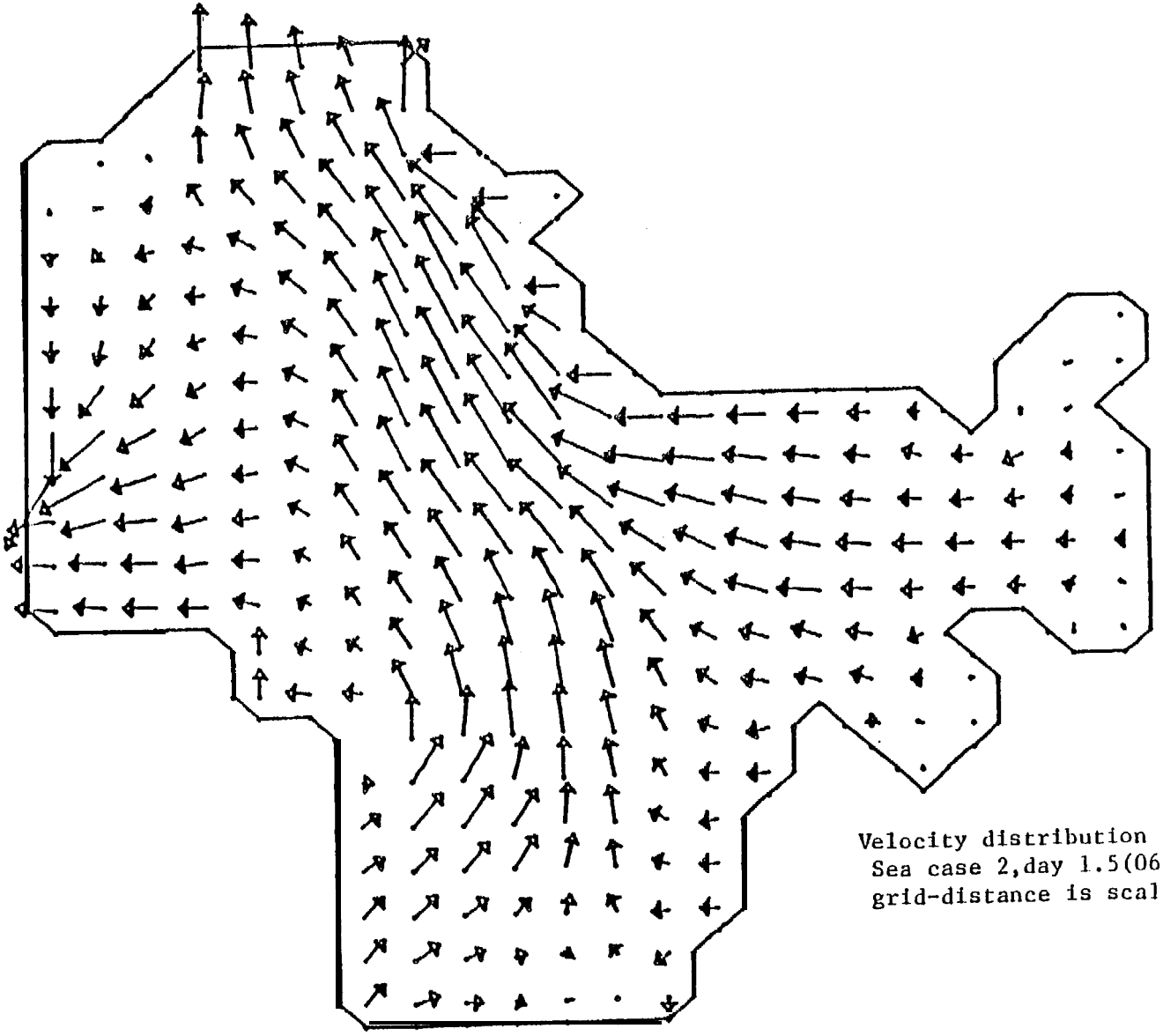

FIG. 75
Velocity distribution in the northeastern Bering Sea case 2, day 1.5 (06Z, March 9, 1982). One horizontal grid-distance is scaled to 20 cm/s.

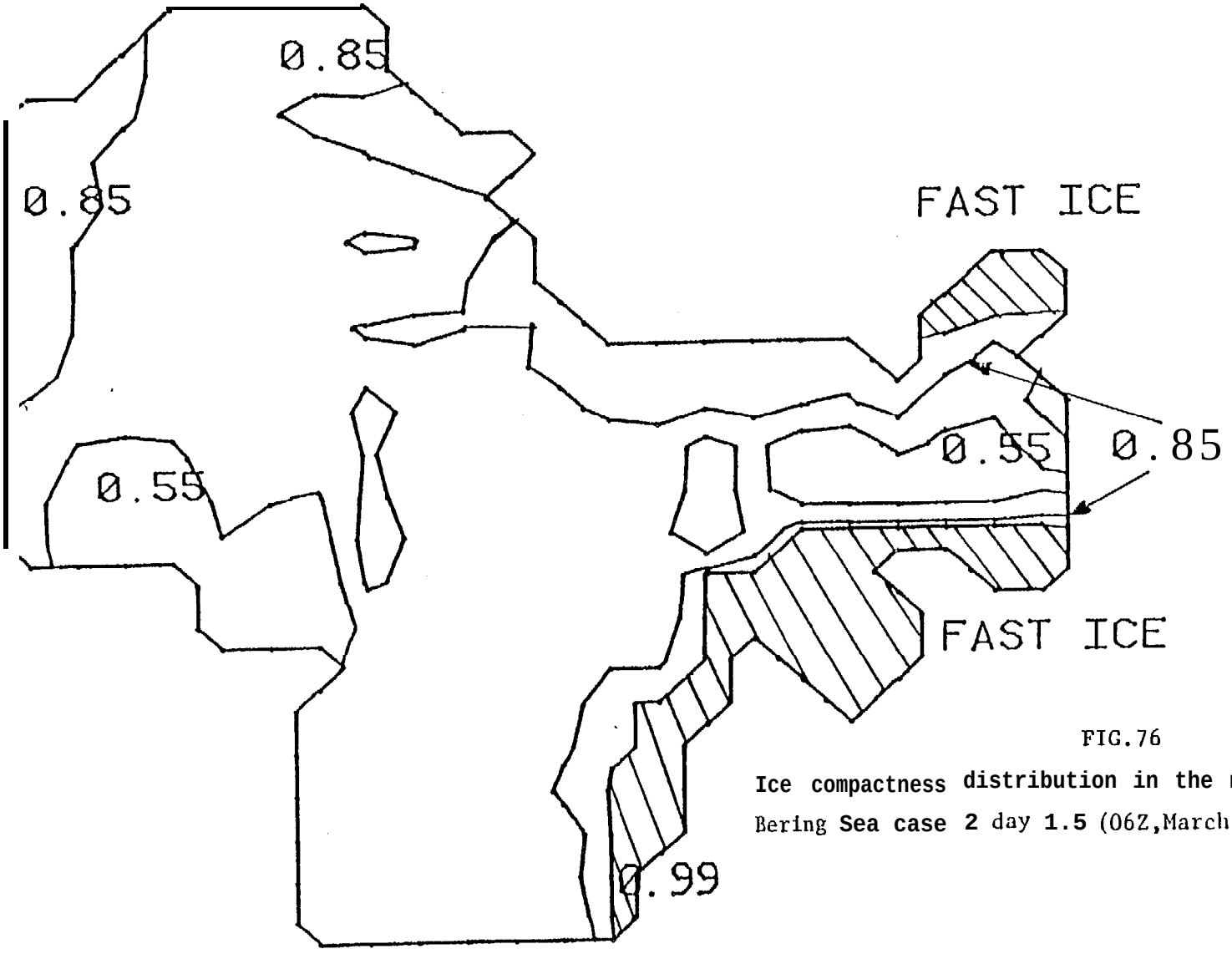

FIG.76

Ice compactness distribution in the northeastern Bering Sea case 2 day 1.5 (06Z,March 9,1982)

ICE COMPACTNESS) HOUR 36

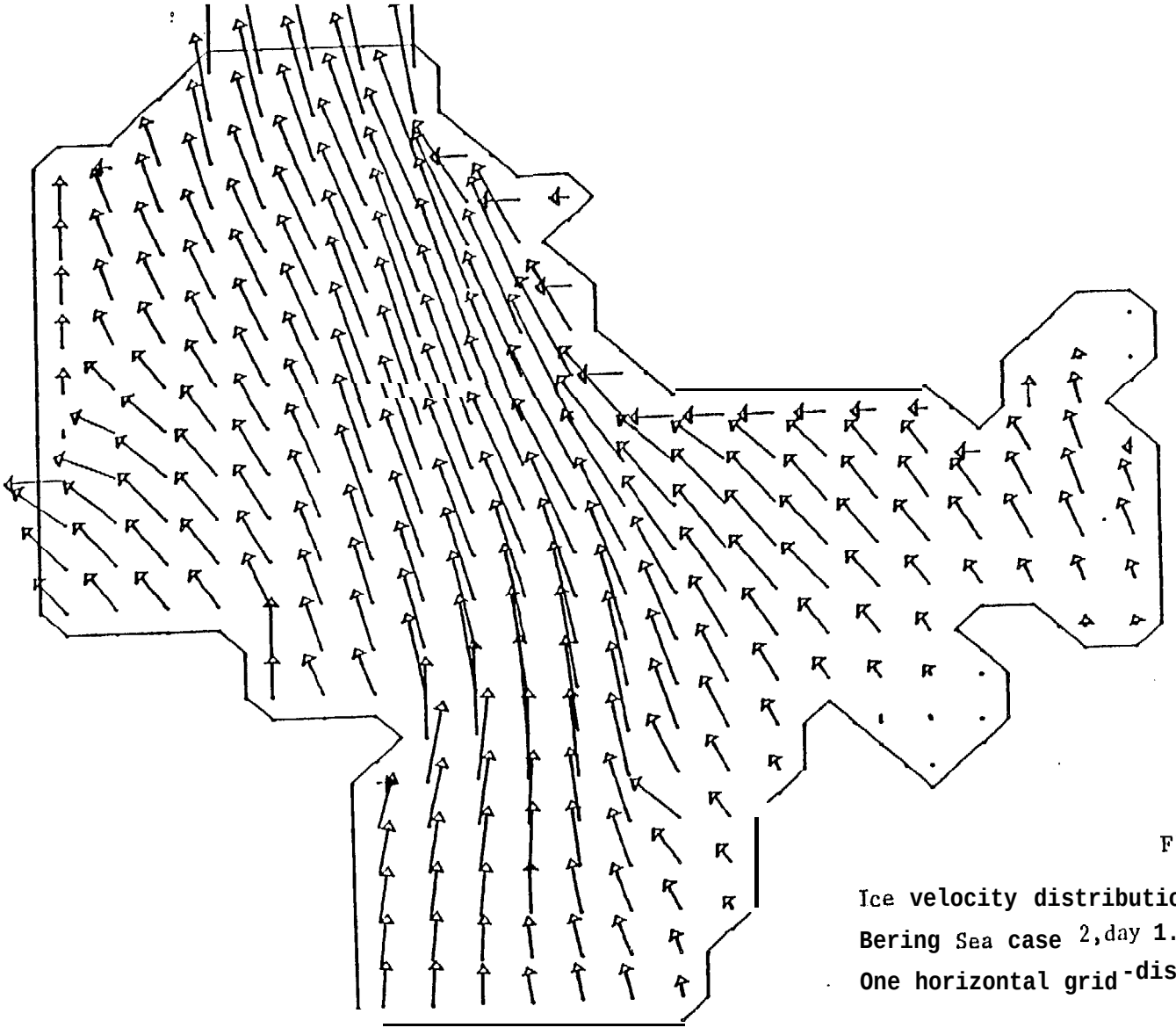

FIG.77

Ice velocity distribution in the northeastern Bering Sea case 2, day 1.5 (06 Z, March 9, 1982). One horizontal grid-distance is scaled to 20cm/s.

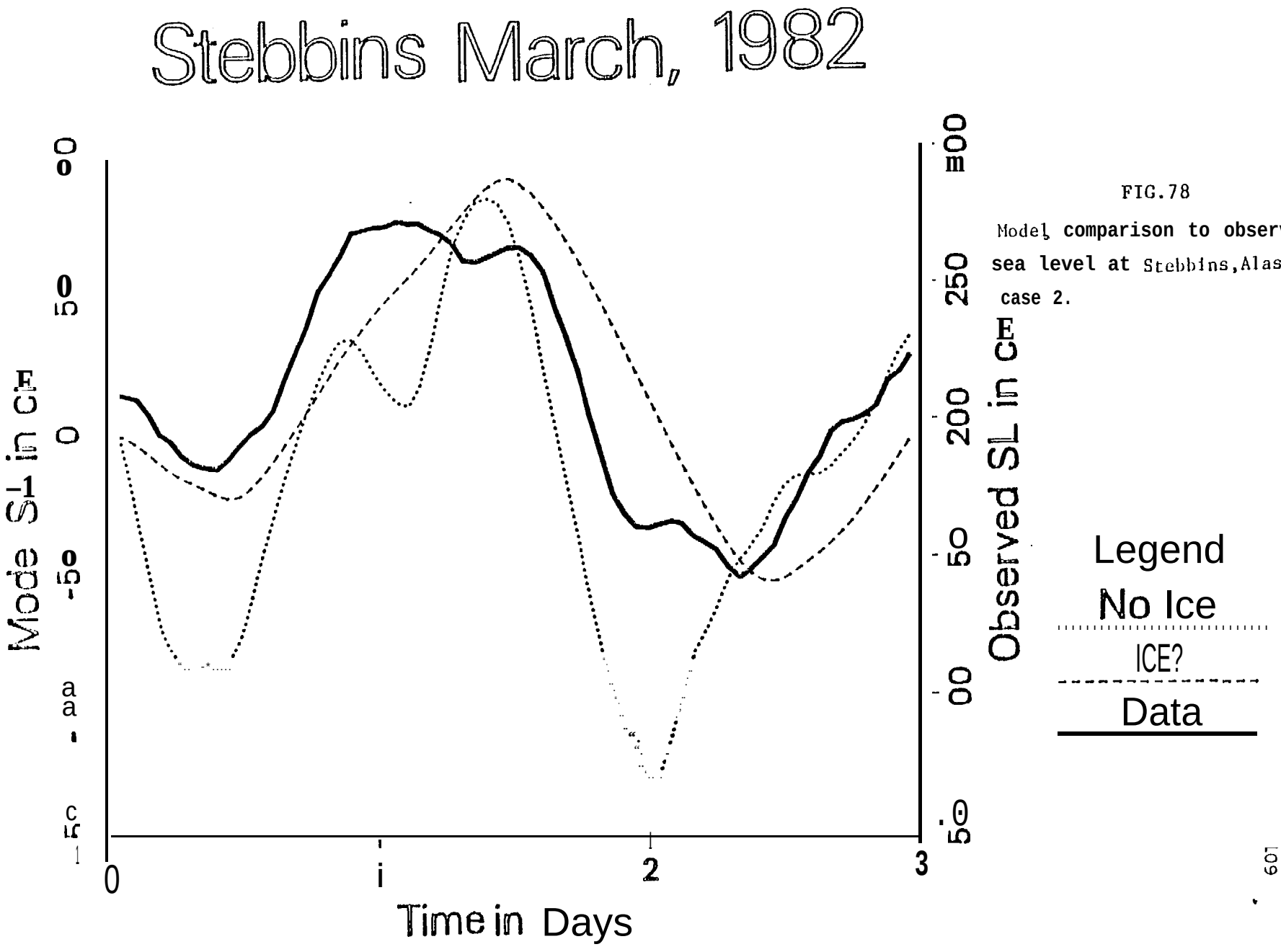

FIG.78

Model comparison to observed sea level at Stebbins, Alaska, case 2.

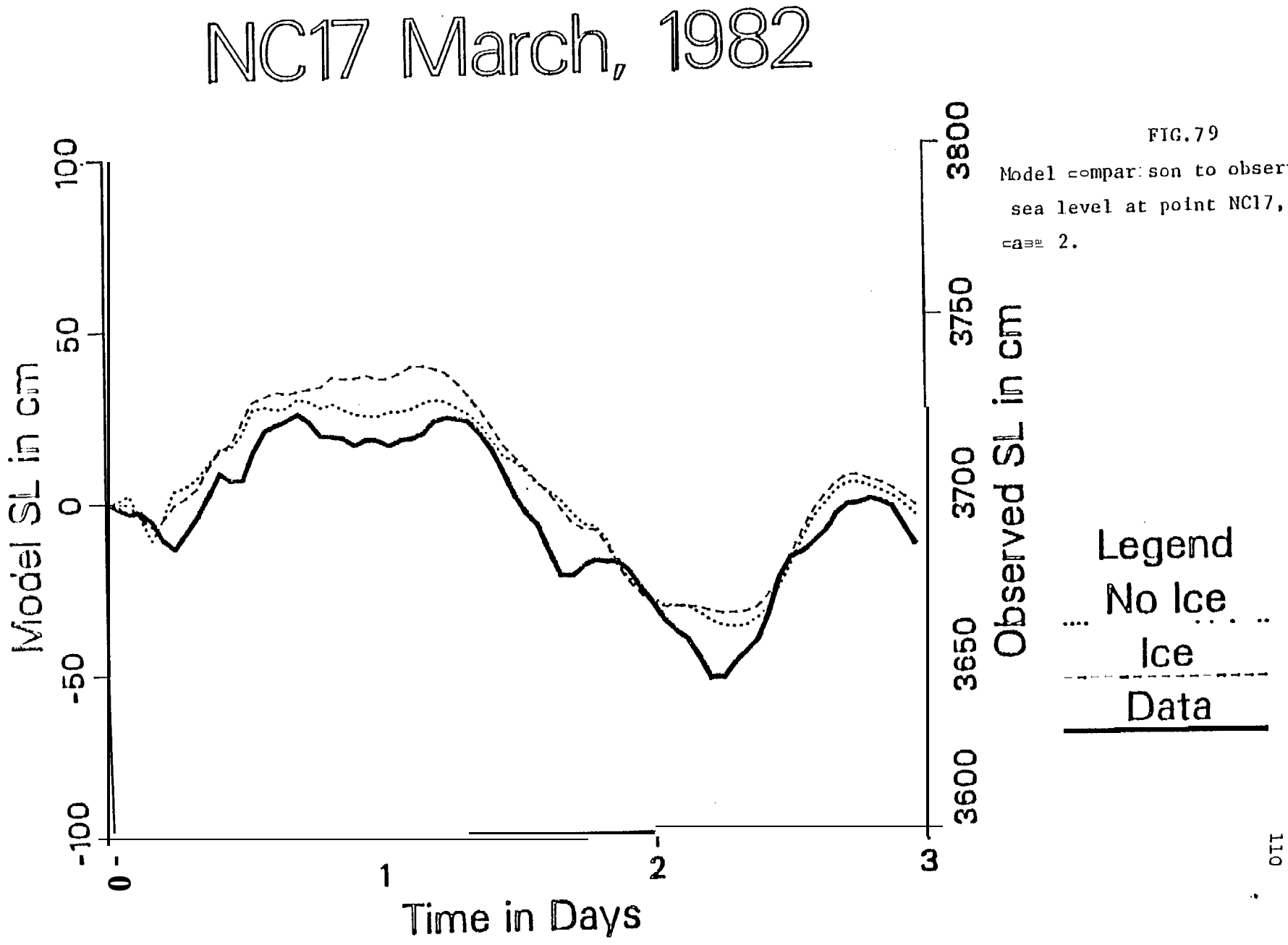

FIG.79

Model comparison to observed sea level at point NC17, case 2.

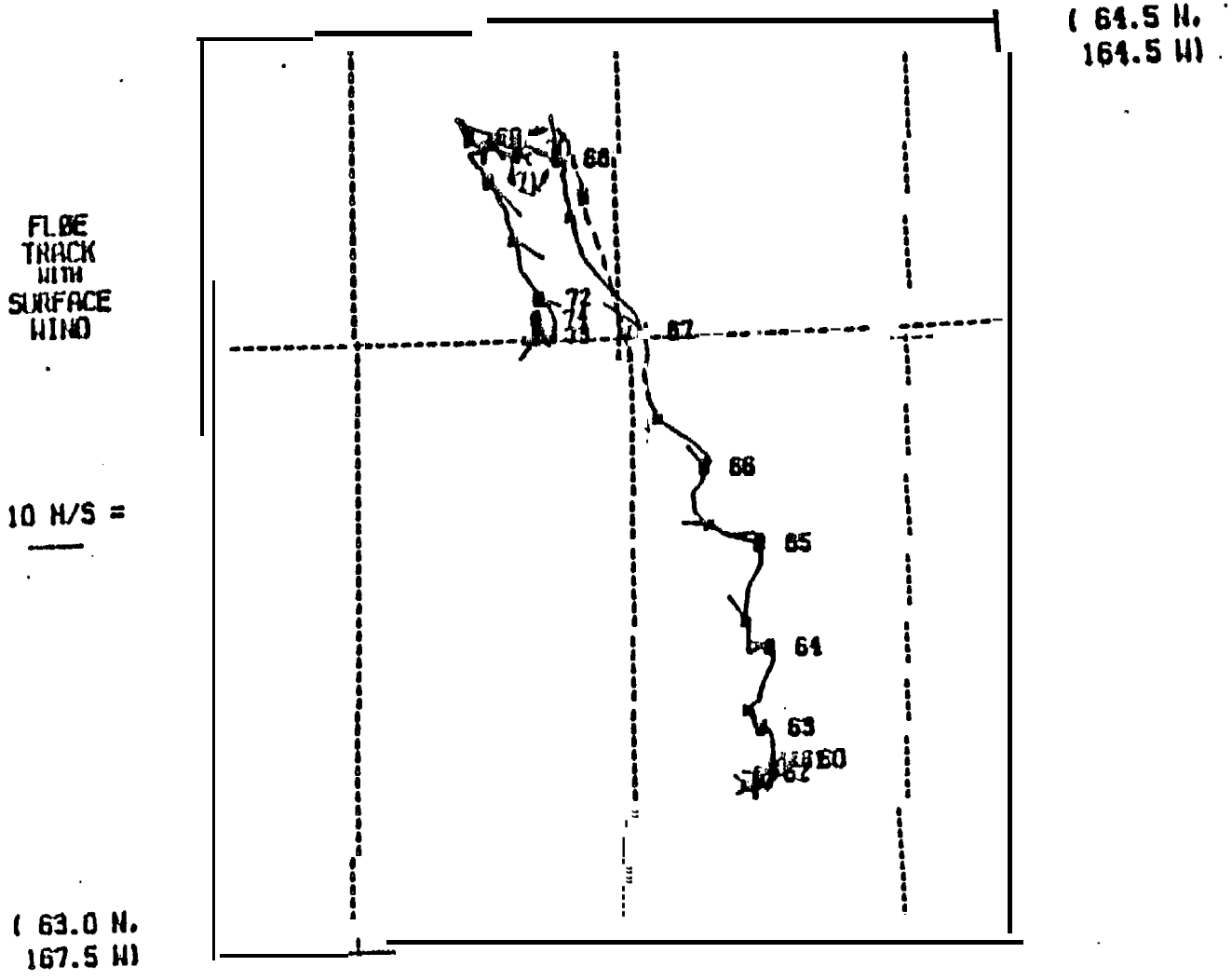

FIG.80

Ice drift floe track, March 1-15,1982 (JD 60-74). Measured by Reynolds and Pease(1984 (Floe stat °°
2322B)- continuous line, and calcu ated from model- broken line.

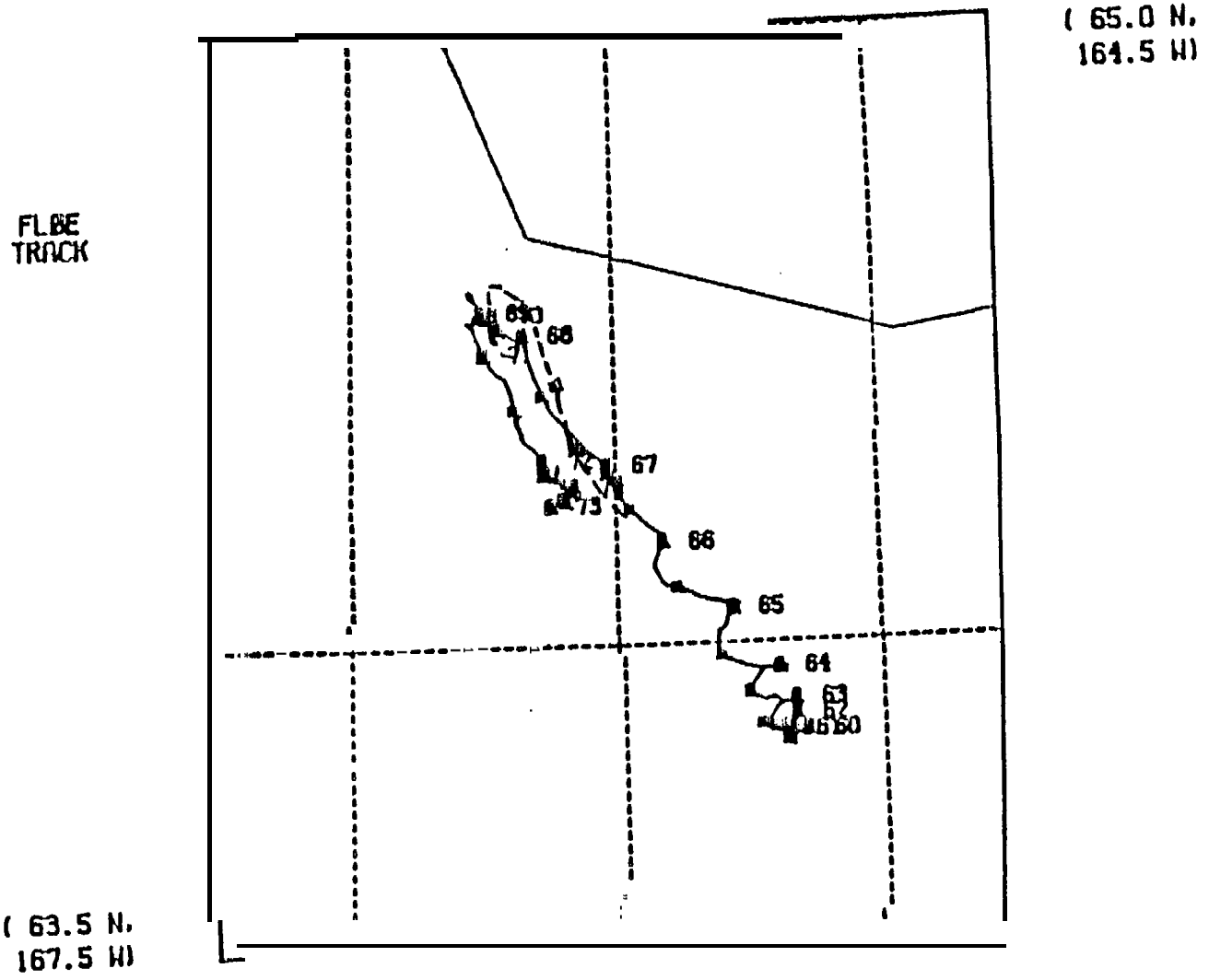

FIG.8E

Ice drift floe track, March 1-15,1982 (JD 60-74). Measured by Reynolds and Pease(1984) F oe station 2321B) - continuous line, and calculated from model - broken line.

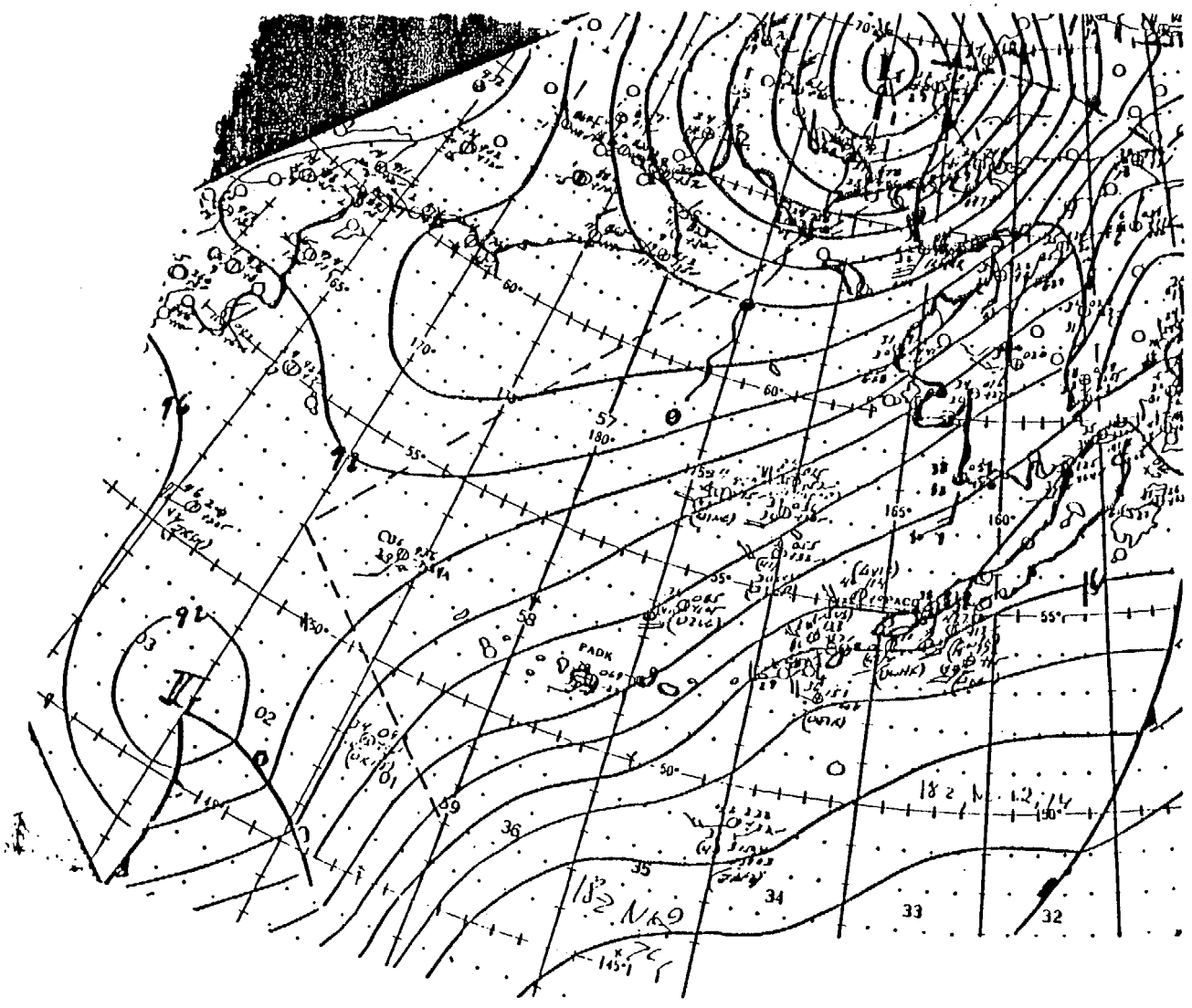

FIG.82

Sur a=e weather chart for 18^{z},November 12,1974. Pressure is give∘ i∘ millibars.

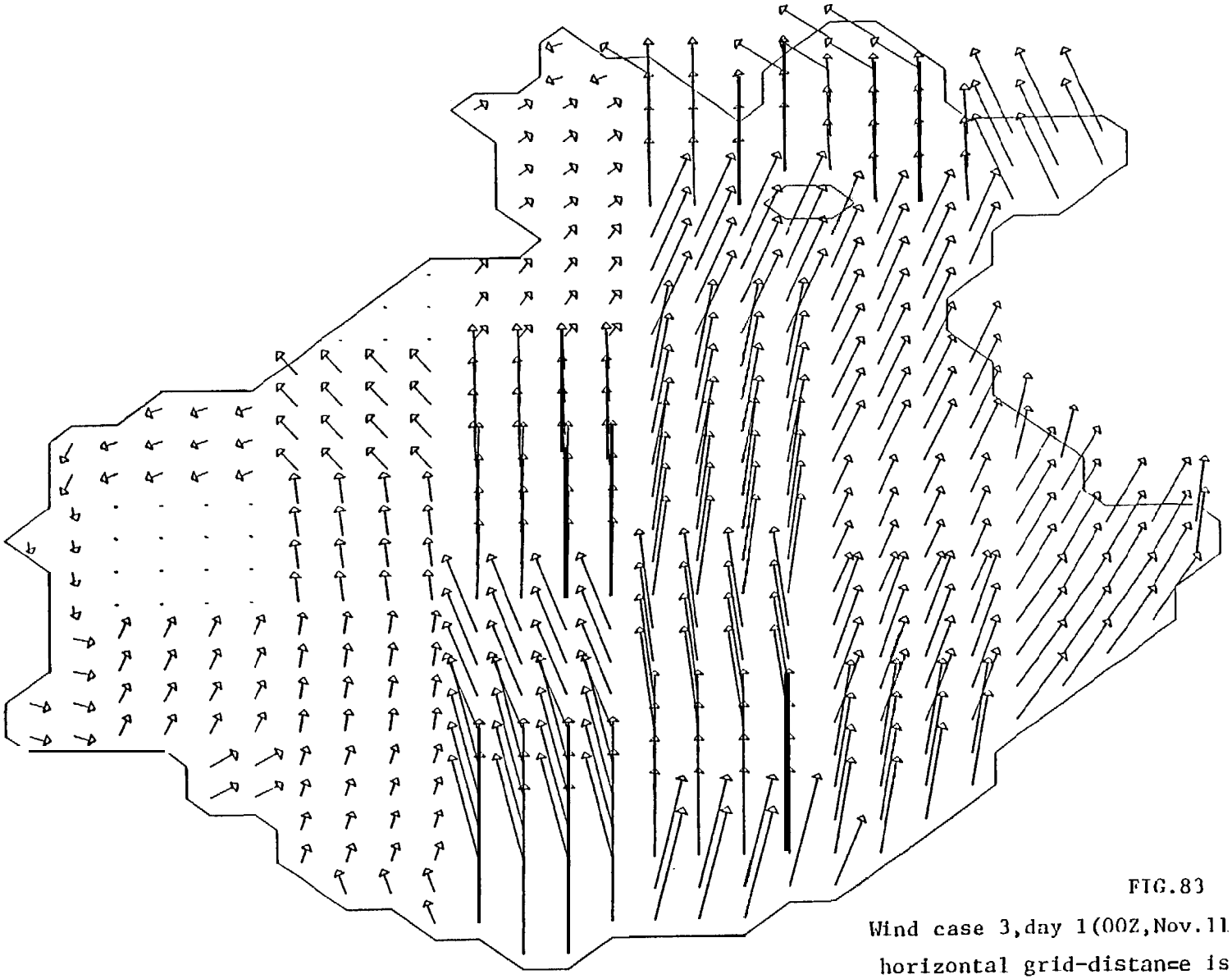

FIG.83

Wind case 3, day 1 (00Z, Nov. 11, 1974). One horizontal grid-distance is scaled to 10 m/s.

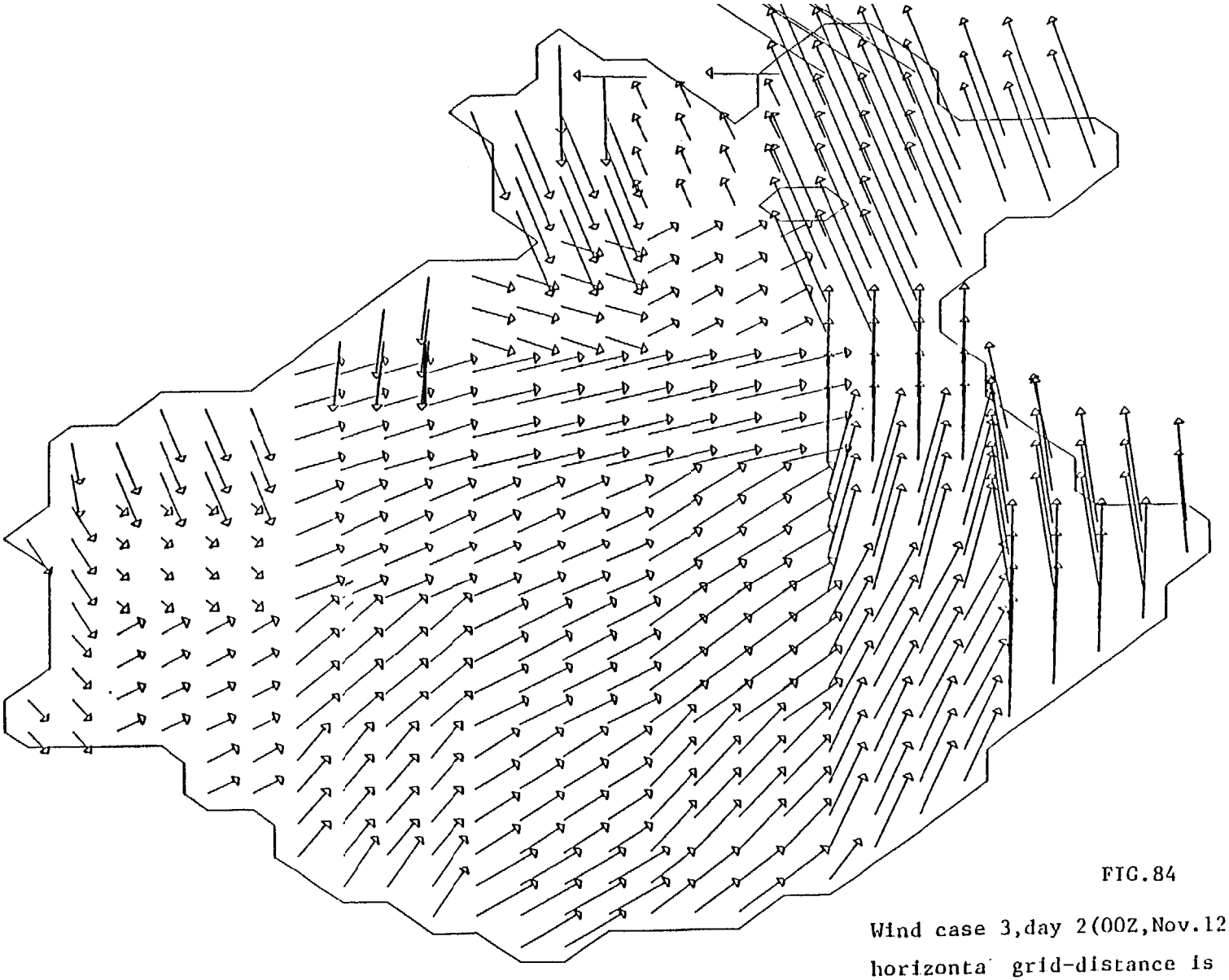

FIG.84

Wind case 3,day 2(00Z,Nov.12,1974). One horizonta grid-distance is scaled to 10m/s.

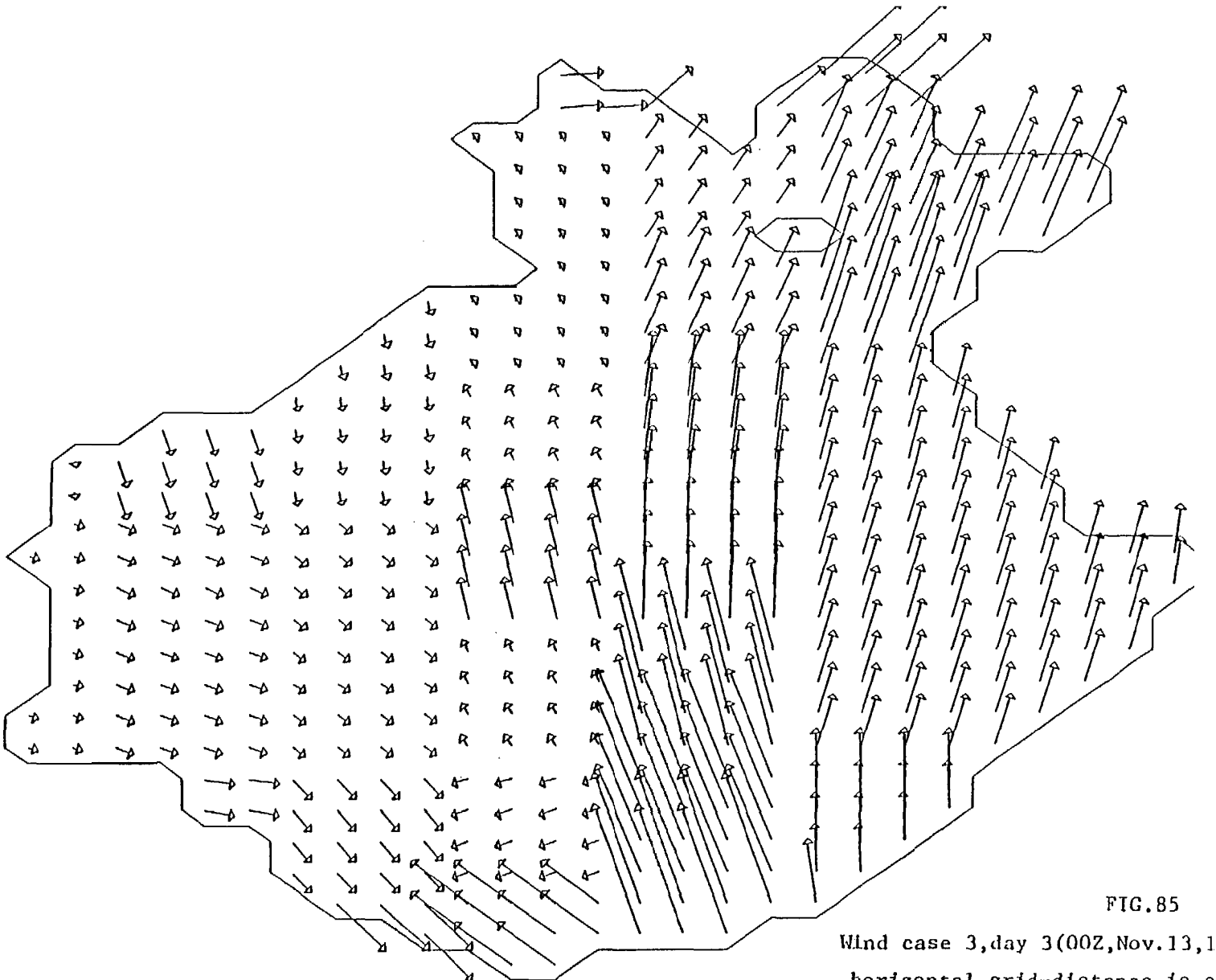

FIG.85

Wind case 3,day 3(00Z,Nov.13,1974). One horizontal grid-distance is scaled to 10m/s.

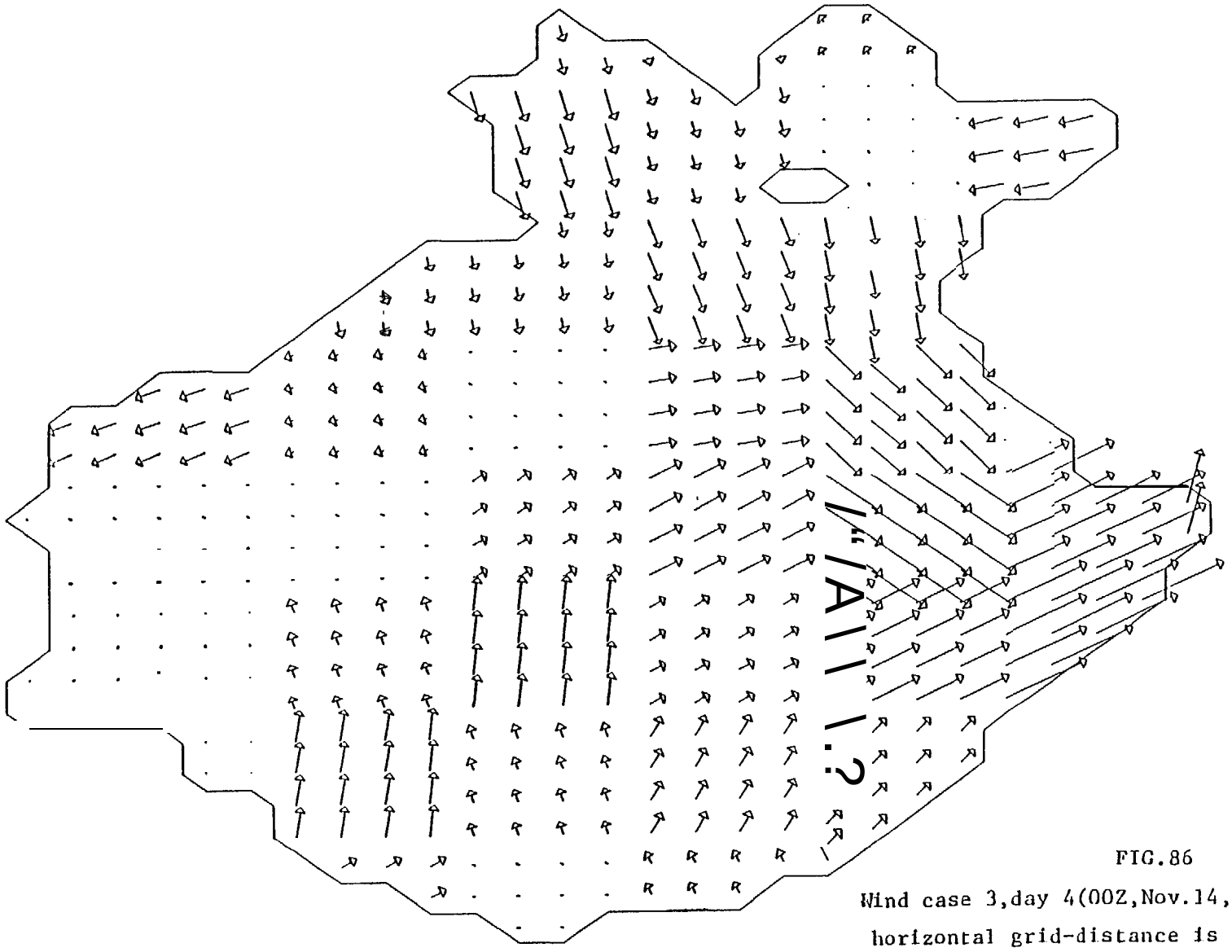

FIG.86

Wind case 3,day 4(00Z,Nov.14, 974). One horizontal grid-distance is scaled to 10m/s.

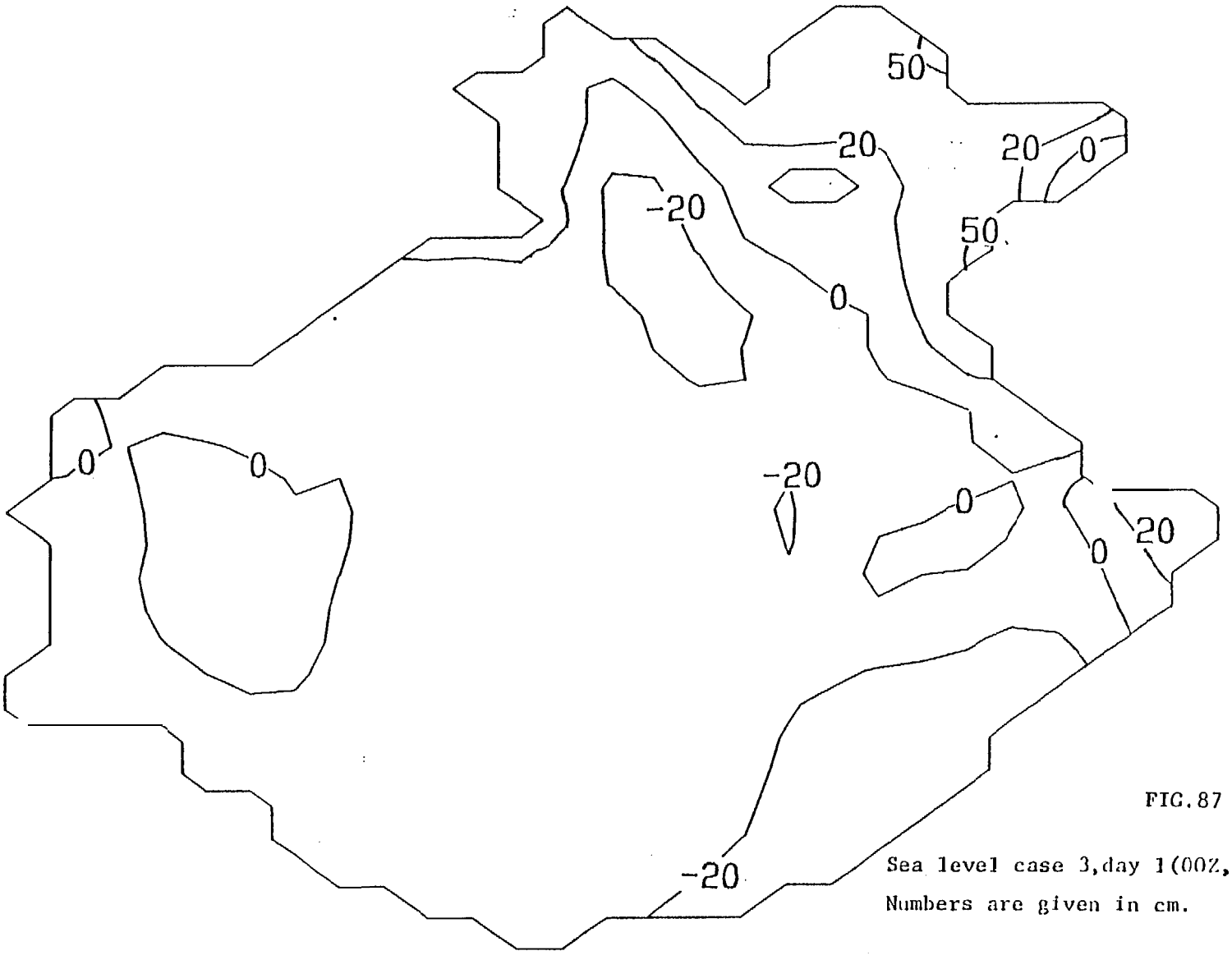

FIG. 87

Sea level case 3, day 1 (00Z, Nov. 11, 1974).
Numbers are given in cm.

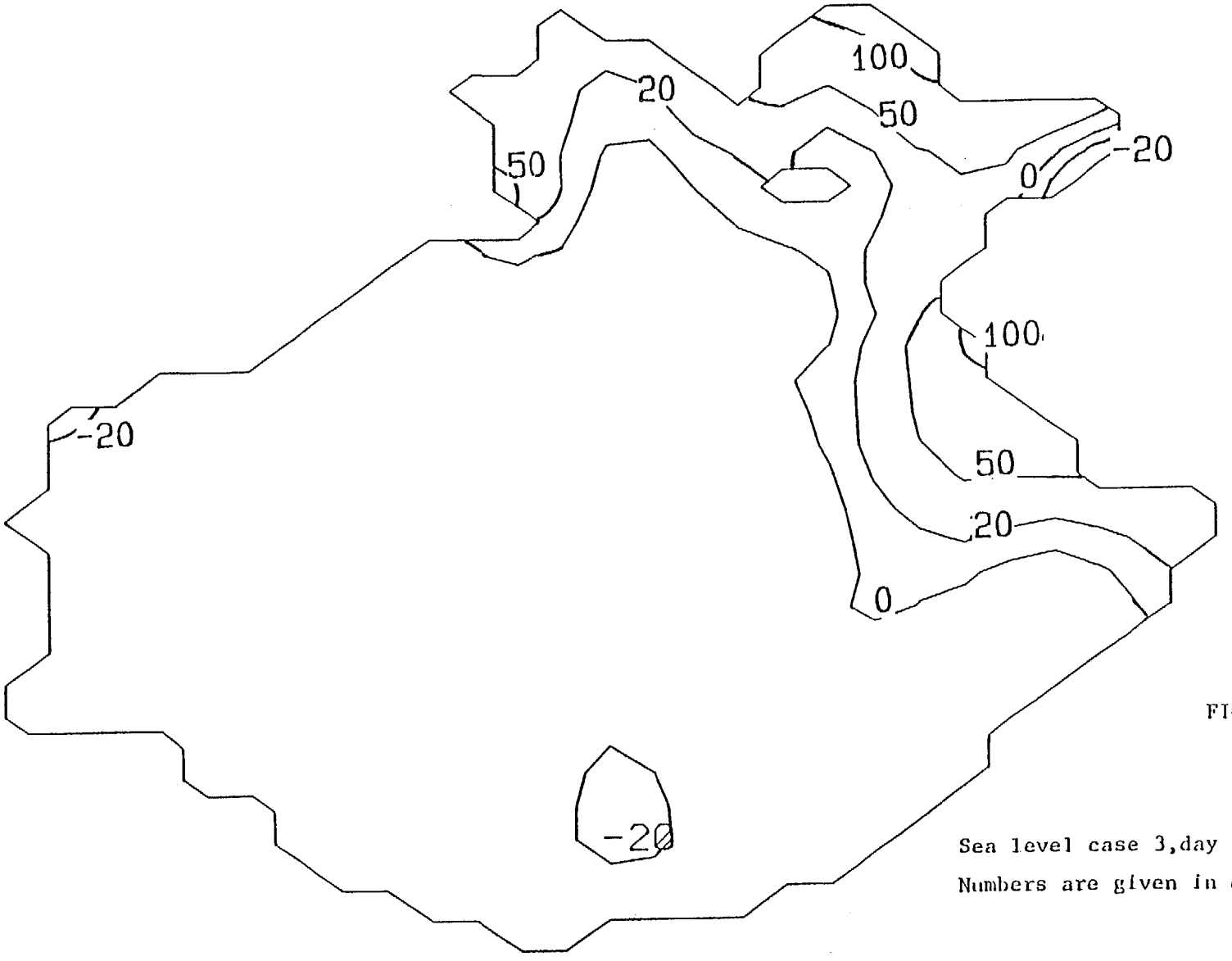

FIG.88

Sea level case 3,day 2(00Z,Nov.12,1974)
Numbers are given in cm.

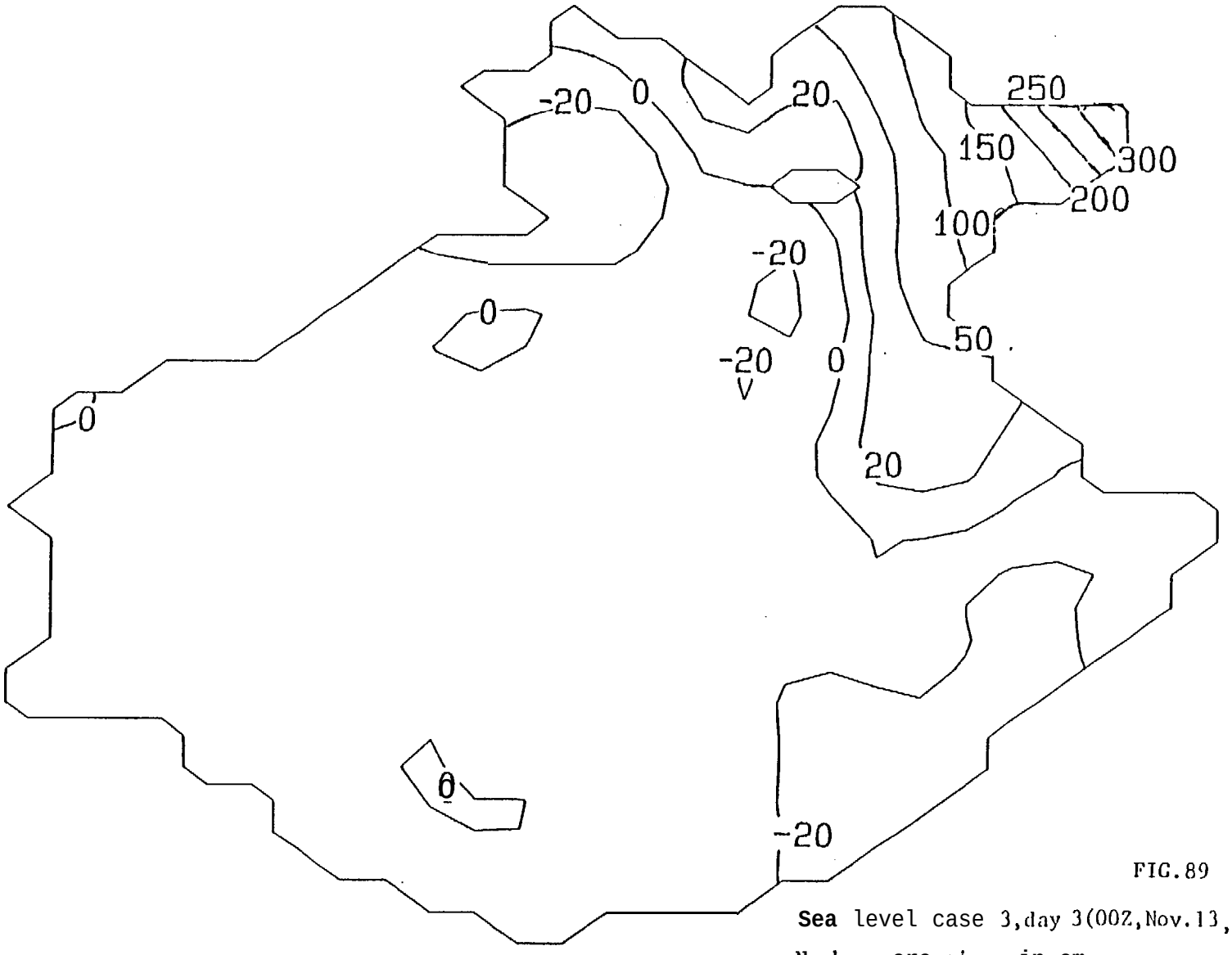

FIG.89

Sea level case 3,day 3(00Z,Nov.13,1974).
Numbers **are** given **in cm.**

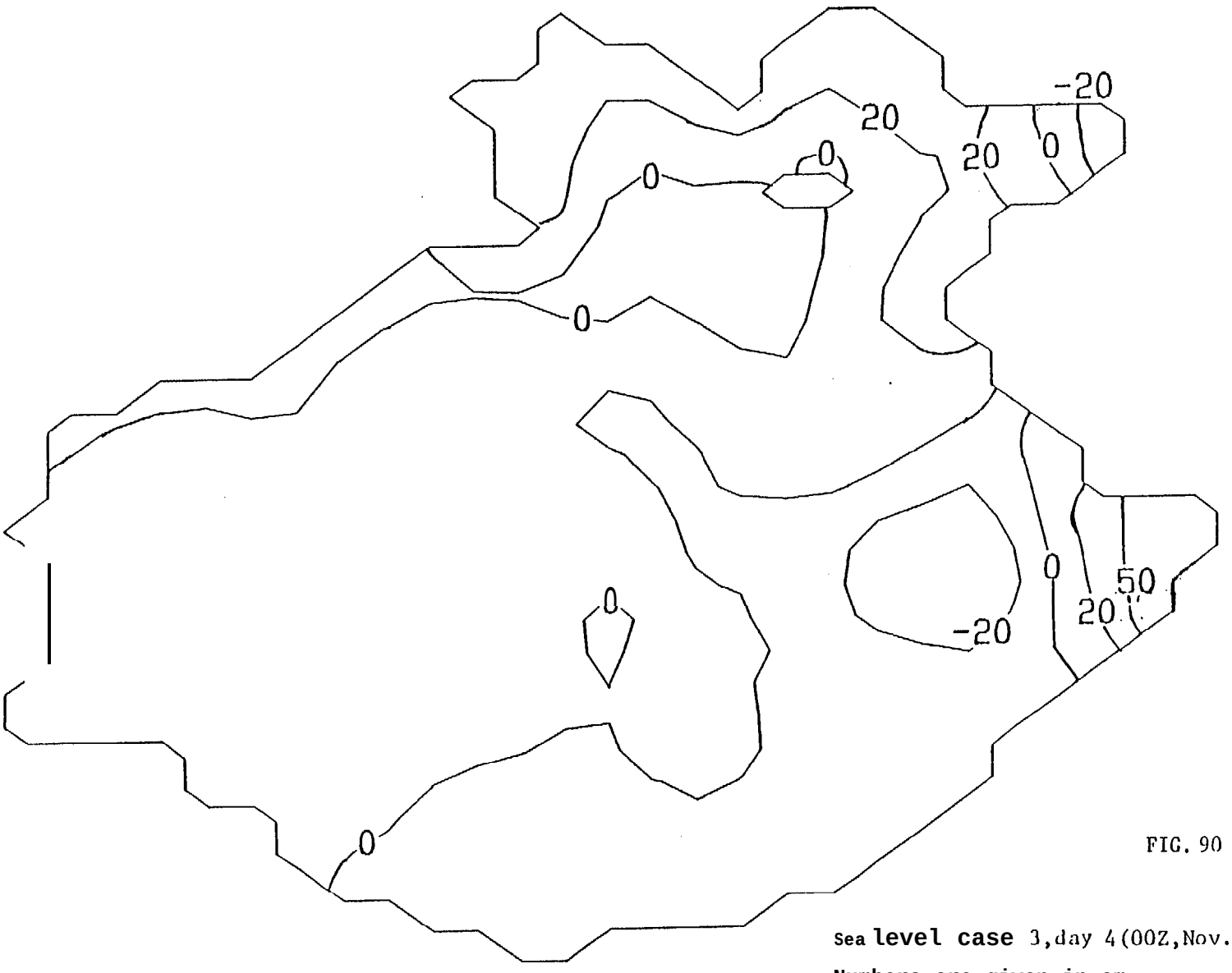

FIG. 90

Sea level case 3, day 4 (00Z, Nov. 14, 1974).
Numbers are given in cm.

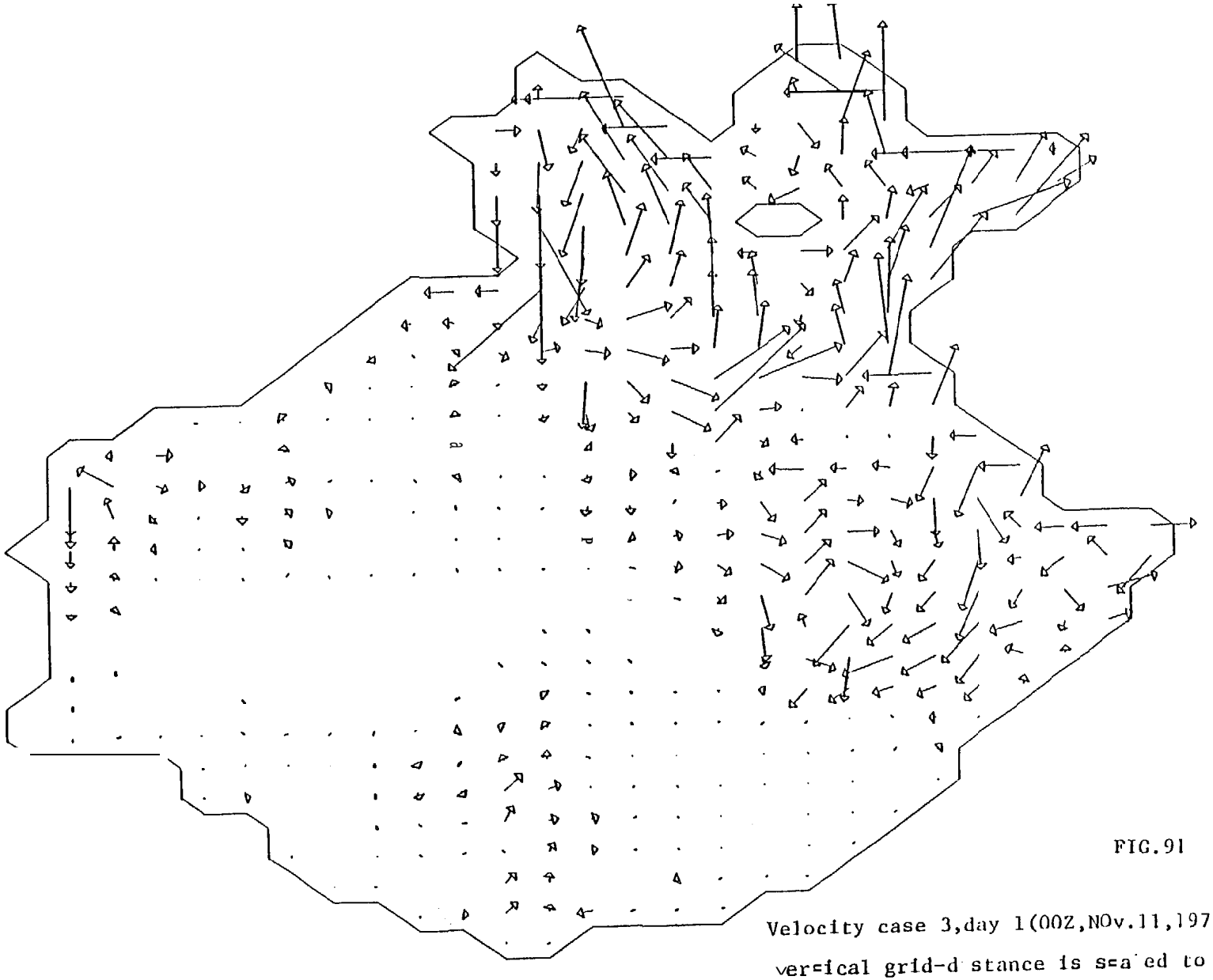

FIG.91

Velocity case 3,day 1(00Z,NOv.11,1974). One ver=ical grid-d stance is s=a ed to 10 cm/s.

V DaY

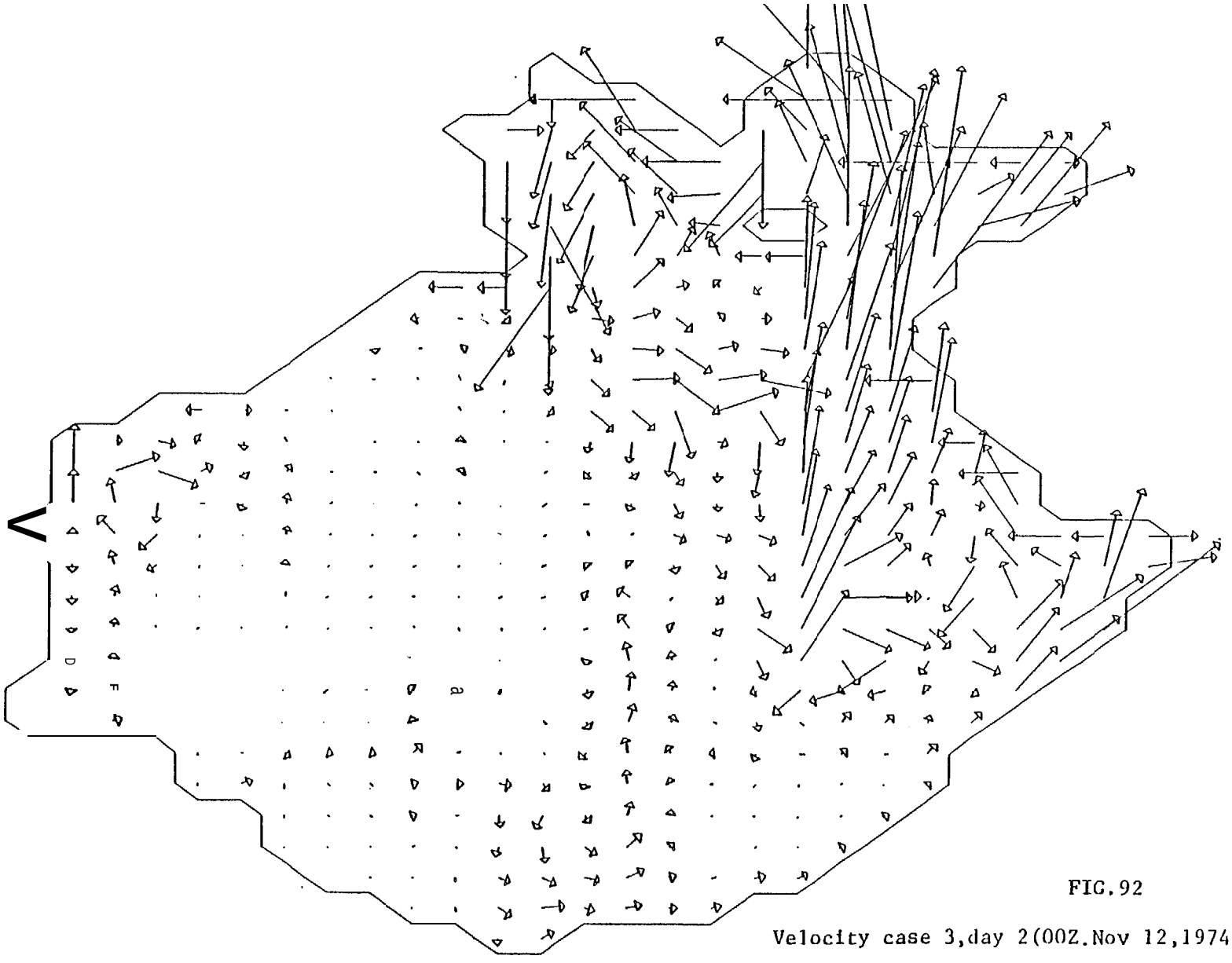

FIG. 92

Velocity case 3, day 2 (00Z. Nov 12, 1974). One vertical grid-distance is scaled to 10 cm/s.

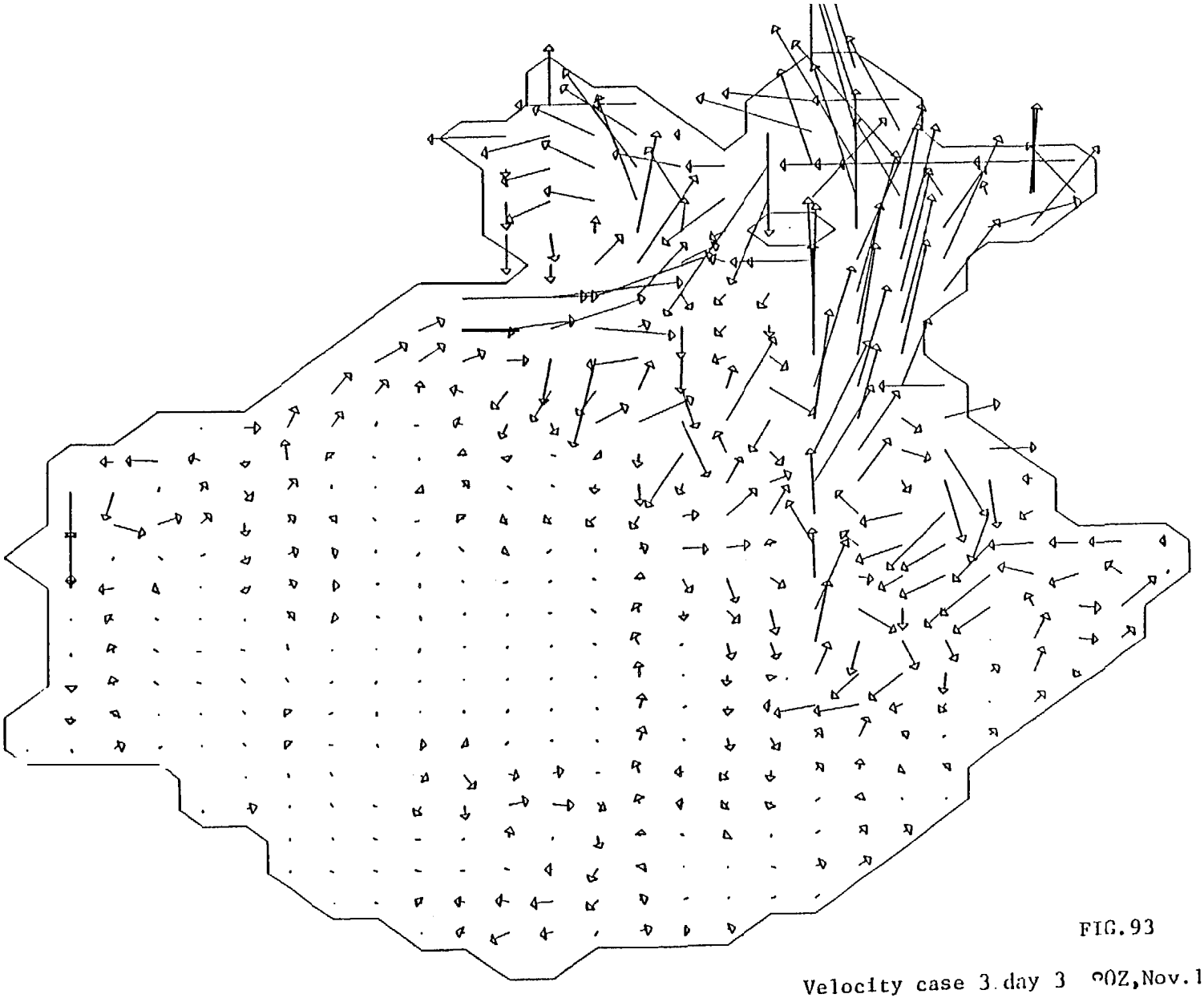

FIG.93

Velocity case 3 day 3 00Z,Nov.13,1974). One vertical grid-distance is scaled to 10 cm/s.

V DAY 3

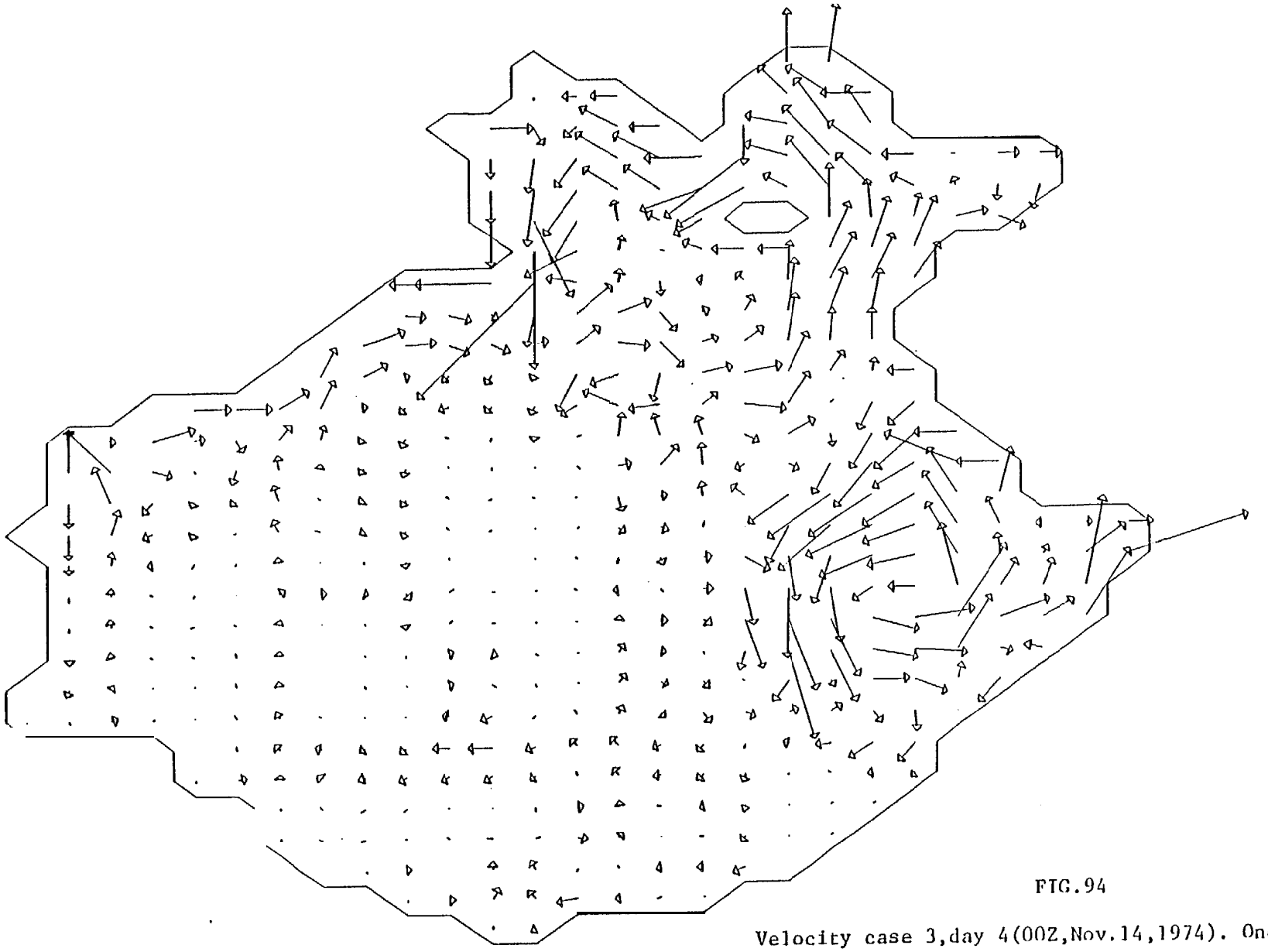

FIG.94

Velocity case 3,day 4(00Z,Nov.14,1974). One vertical grid-distance is scaled to 9 cm/s.

V DAY 4

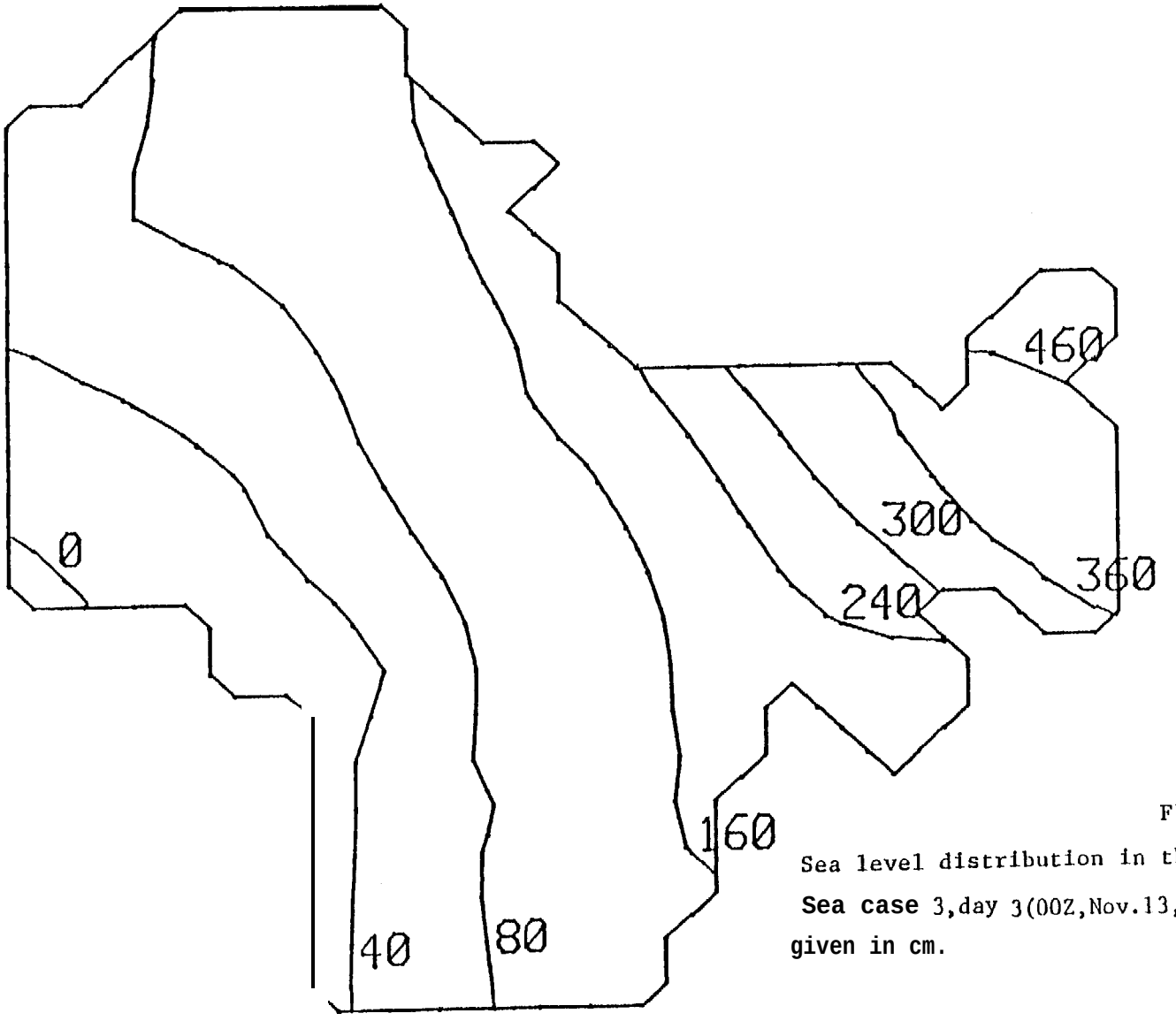

FIG.95

Sea level distribution in the northeastern Bering Sea case 3,day 3(00Z,Nov.13,1974). Numbers are given in cm.

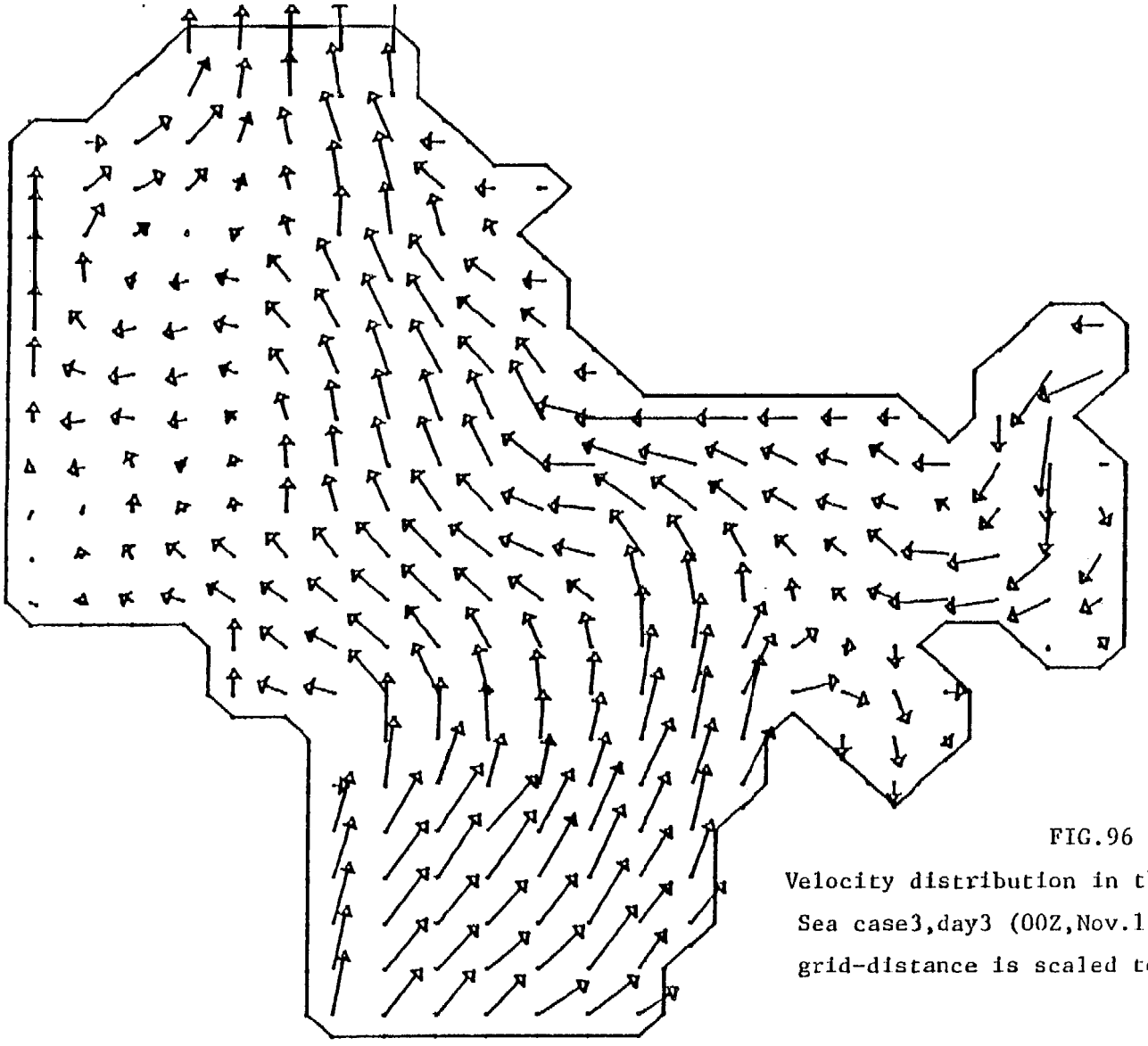

FIG.96

Velocity distribution in the northeastern Bering Sea case3,day3 (00Z,Nov.13,1974). One horizontal grid-distance is scaled to 40cm/s.

STEBBINS, NOV. 74

FIG. 97

Computed sea level time series at Stebbins, case 3.

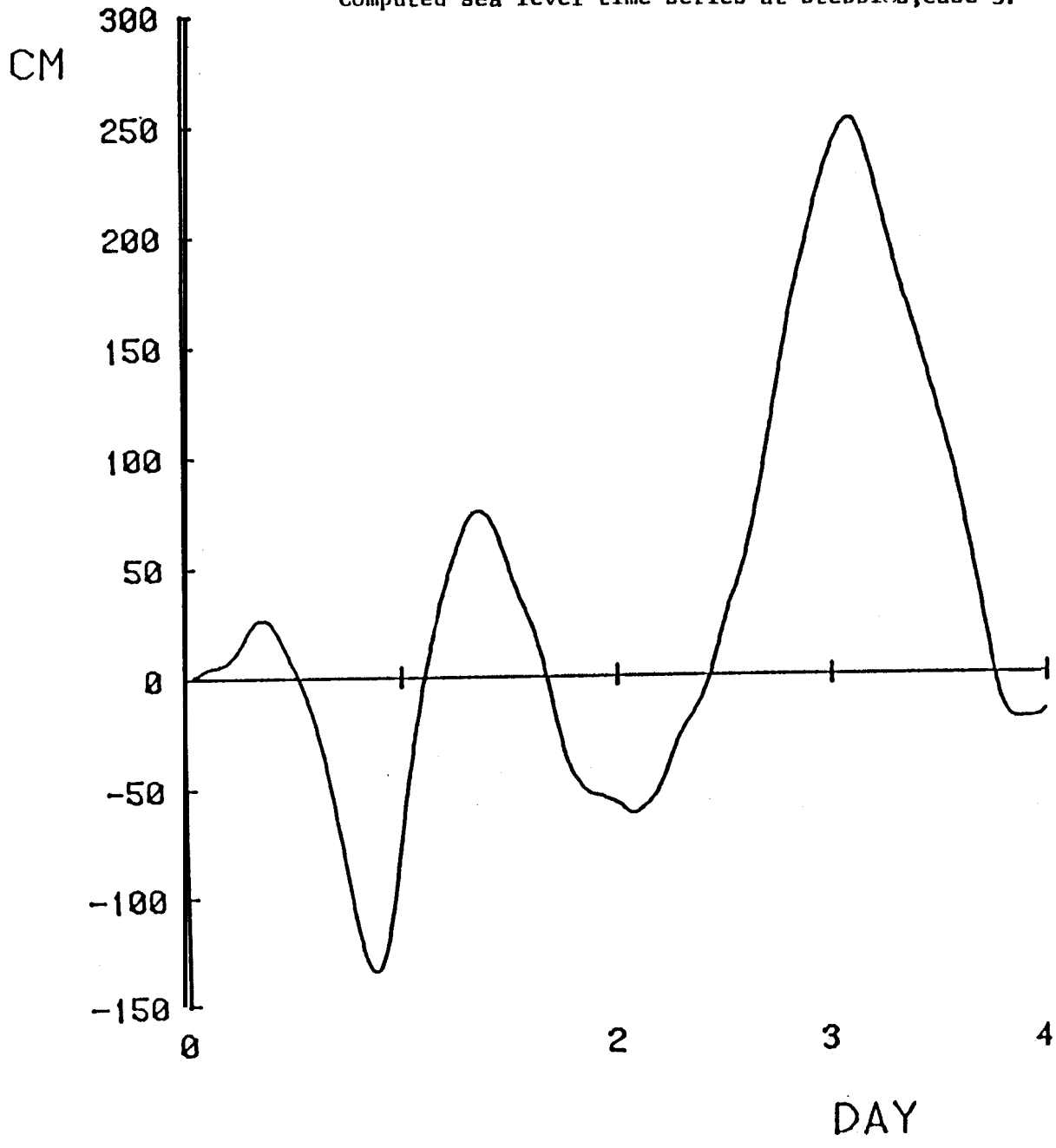

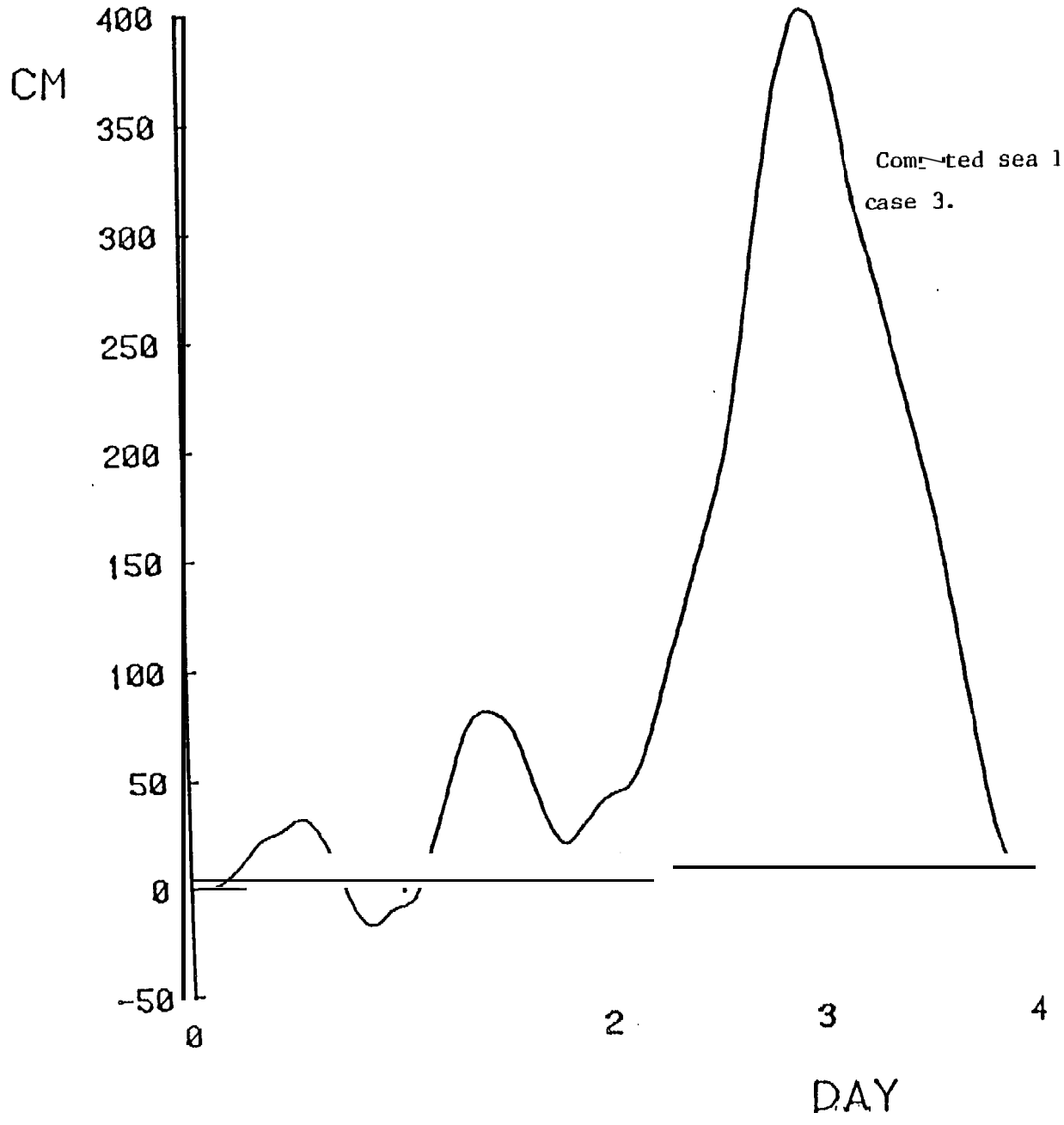

FIG.98

Computed sea level time series at Unalakleet, case 3.

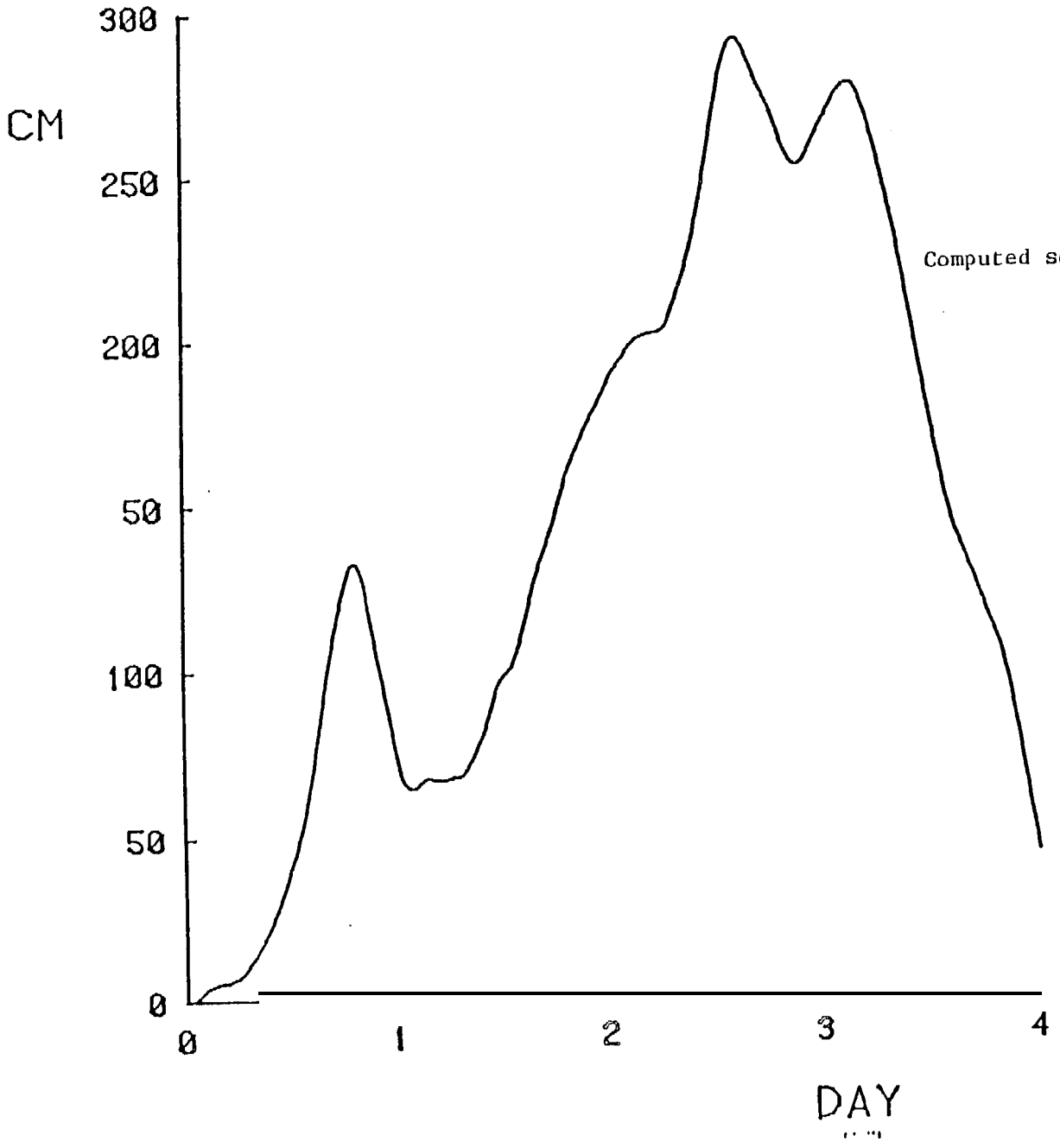

FIG.99

Computed sea level time series at Nome, case 3.

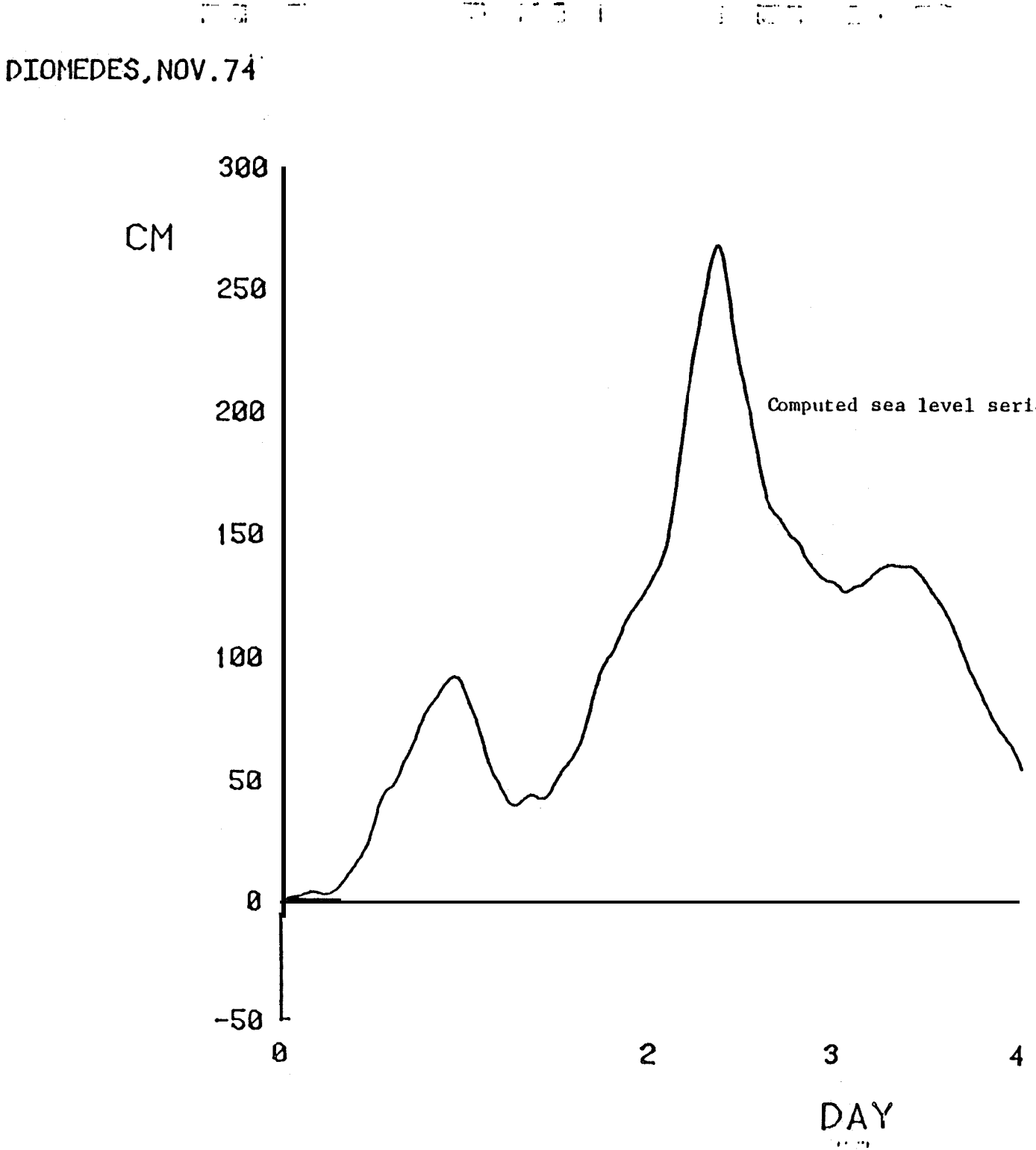

FIG.100

Computed sea level series at Diomedes, case 3.